

A SURGICAL CONFOCAL MICROLAPAROSCOPE FOR REAL-TIME
OPTICAL BIOPSIES

by

Anthony Amir Tanbakuchi

Copyright ©Anthony Amir Tanbakuchi 2009

A Dissertation Submitted to the Faculty of the
COLLEGE OF OPTICAL SCIENCES

In Partial Fulfillment of the Requirements For the Degree of

DOCTOR OF PHILOSOPHY

In the Graduate College

THE UNIVERSITY OF ARIZONA

2009

THE UNIVERSITY OF ARIZONA GRADUATE COLLEGE

As members of the Dissertation Committee, we certify that we have read the dissertation prepared by Anthony Amir Tanbakuchi entitled A surgical confocal microlaparoscope for real-time optical biopsies and recommend that it be accepted as fulfilling the dissertation requirement for the Degree of Doctor of Philosophy

____ Date: April 2, 2009
Arthur Gmitro

____ Date: April 2, 2009
Urs Utzinger

____ Date: April 2, 2009
Jim Schwiegerling

____ Date: April 2, 2009
Andrew Rouse

Final approval and acceptance of this dissertation is contingent upon the candidate's submission of the final copies of the dissertation to the Graduate College. I hereby certify that I have read this dissertation prepared under my direction and recommend that it be accepted as fulfilling the dissertation requirement.

____ Date: April 2, 2009
Dissertation Director: Arthur F. Gmitro

STATEMENT BY AUTHOR

This dissertation has been submitted in partial fulfillment of requirements for an advanced degree at the University of Arizona and is deposited in the University Library to be made available to borrowers under rules of the Library.

Brief quotations from this dissertation are allowable without special permission, provided that accurate acknowledgment of source is made. Requests for permission for extended quotation from or reproduction of this manuscript in whole or in part may be granted by the copyright holder.

SIGNED: _____
Anthony Amir Tanbakuchi

ACKNOWLEDGEMENTS

This work would not have been possible without the collaborative efforts of Dr. Arthur Gmitro, Dr. Andrew Rouse, Dr. Molly Brewer, Dr. Kenneth Hatch, and Dr. Richard Sampliner. All of these individuals contributed insight and expertise that made this project a success. Dr. Gmitro provided the initial vision and direction for *in vivo* confocal imaging systems and obtained the funding to support the work. Dr. Rouse had significant participation in the project and provided important guidance. Dr. Brewer helped motivate the development of the instrument and gave guidance on how such an instrument would be used in a clinical setting. Dr. Hatch served as the primary clinician to test the device *in vivo*. Dr. Sampliner provided human esophagus biopsies for the *ex vivo* imaging studies. I would also like to thank Kathy Schmidt and the surgical staff at UMC who provided critical assistance during the clinical trials and Dr. Katerina Dvorak and Angelique Kano for providing mice to image with the bare fiber probes.

Funding for this work was provided by the Arizona Disease Control Research Commission grant number 971, NIH grants CA 94287 and CA 115780, the BMIS Fellowship, and the Imaging Fellowship.

I would like to thank my dissertation committee, Dr. Arthur Gmitro, Dr. Andrew Rouse, Dr. Urs Utzinger, and Dr. Jim Schwiegerling, for providing guidance and constructive criticism.

Finally, I would never have accomplished this work without the inspiration I received from the handful of great teachers. I feel lucky to have been their student. I hope that I will be able to give back to society as much as they gave to their students. Thank you Dr. Russell Kraus, Priscilla Morton, Fred Marinello, and Robert Petitmermet.

DEDICATION

To Kristina.



TABLE OF CONTENTS

LIST OF ILLUSTRATIONS	9
LIST OF TABLES	13
ABSTRACT	14
NOMENCLATURE	15
1 Introduction	17
1.1 Motivation	17
1.2 Clinical testing for the early detection of ovarian cancer	21
1.3 Statement of authorship and publication intentions	24
A clinical confocal microlaparoscope for real-time <i>in vivo</i> optical biopsies	24
In vivo imaging of ovarian tissue using a novel confocal microlaparoscope	27
Monte Carlo characterization of parallelized fluorescence confocal systems imaging in turbid media	29
2 Design and development	31
2.1 Clinical confocal microlaparoscope system	31
Mobile cart	34
Optical scan unit	34
Software control system	37
Confocal Microlaparoscopes	39
First generation design	40
Second generation design	44
Third generation design	47
2.2 Results	50
Ovarian images	51
Esophagus images	55
3 Clinical application and testing	58
3.1 Materials and methods	58

Confocal microlaparoscope system	59
Fluorescent Contrast Agents	62
Confocal Imaging Procedure	64
3.2 Results	66
4 Monte Carlo analysis	73
4.1 Introduction	73
4.2 Monte Carlo model of a fluorescence confocal system	78
Model Principles	79
Implemented model	82
4.3 Results and Discussion	91
Characterizing aperture imaging performance	94
Optimizing pinhole spacing	106
Characterizing effects of tissue properties.	107
Characterizing the effect of fluorophore concentration.	109
5 New miniature objective lens	112
5.1 Existing miniature lens	112
5.2 New miniature lens	114
6 Bare fiber probes	124
6.1 Probe designs	125
6.2 Results	127
7 Conclusions	135
7.1 Summary of work	135
7.2 Future work	138
APPENDICES	140
A Microlaparoscope design details	141
A.1 First generation design	141
A.2 Second generation design	146
A.3 Third generation design	148
Mechanical drawings	150
Optical Scan Unit	173
Real-time multi-spectral	176
B New miniature lens details	177
B.1 Lens data	177
B.2 Lens quotation	190
B.3 Additional Designs	193

TABLE OF CONTENTS - CONTINUED

8

C Clinical software	195
C.1 Dependencies	196
C.2 Classes	196
Main program	196
Image processing, encoding, and display	197
Hardware interface	198
D Bare fibers	200
E Citation Index	202
F Colophon	206
REFERENCES	207

LIST OF ILLUSTRATIONS

1.1 An ovary is resected and sent to pathology for histological processing.	19
1.2 An ovary is imaged <i>in vivo</i> in real-time using a confocal micro-laparoscope.	20
1.3 Cross-section and en-face slices on an ovary.	21
1.4 “ <i>A clinical confocal microlaparoscope for real-time in vivo optical biopsies,</i> ” submitted for publication.	25
1.5 “ <i>In vivo imaging of ovarian tissue using a novel confocal microlaparoscope,</i> ” submitted for publication.	27
1.6 “ <i>Monte Carlo characterization of parallelized fluorescence confocal systems imaging in turbid media,</i> ” submitted for publication.	29
2.1 The microlaparoscope system imaging the epithelial surface of an ovary during surgery.	32
2.2 Mobile microlaparoscope system.	35
2.3 Diagram of the OSU.	36
2.4 Flow diagram of the clinical software.	38
2.5 Software control system interface.	39
2.6 First generation microlaparoscope.	41
2.7 First generation microlaparoscope focus sequence.	42
2.8 First generation microlaparoscope contrast agent delivery.	43
2.9 The second generation microlaparoscope.	45
2.10 Second generation microlaparoscope contrast agent delivery.	46
2.11 The third generation microlaparoscope.	48
2.12 Third generation microlaparoscope cross-sectional view.	49
2.13 Second generation microlaparoscope contacting the surface of the ovary.	52
2.14 Images of ovary epithelium obtained <i>in vivo</i> with fluorescein sodium.	53
2.15 Images of human ovary epithelium obtained <i>ex vivo</i> with AO.	54
2.16 Images of ovary epithelium obtained <i>in vivo</i> with AO.	55
2.17 Images of human esophagus epithelium obtained <i>ex vivo</i> using AO.	56

3.1	The confocal microlaparoscope.	60
3.2	Microlaparoscope probe tip.	61
3.3	The mobile cart.	62
3.4	Confocal microlaparoscope imaging an ovary <i>in vivo</i>	65
3.5	<i>In vivo</i> imaging of the ovary.	66
3.6	<i>In vivo</i> confocal microlaparoscope images of the human ovary using fluorescein sodium.	67
3.7	(VIDEO) <i>In vivo</i> confocal microlaparoscope video of the human ovary using topically applied fluorescein sodium as the contrast agent.	68
3.8	<i>Ex vivo</i> images of ovarian tissue stained with acridine orange.	69
3.9	(VIDEO) <i>Ex vivo</i> video of normal appearing ovary epithelium tissue stained with acridine orange.	70
3.10	(VIDEO) <i>Ex vivo</i> video of abnormal appearing ovary epithelium tissue stained with acridine orange.	71
3.11	<i>In vivo</i> images of ovarian tissue stained with acridine orange.	72
4.1	Four types of confocal apertures.	75
4.2	Simplified optical layout of a fluorescence confocal system.	76
4.3	Example photon path in turbid media.	82
4.4	Illustration showing the final collected position r_{ci} of a detected photon incident in an aperture at r_d	83
4.5	Flow diagram for the Monte Carlo simulation.	84
4.6	(VIDEO) Movies of the three-dimensional distribution of collected photon signal positions.	95
4.7	Lateral x - y signal distribution for r_s	96
4.8	(VIDEO) Data from Fig 4.6 shown in terms of error in collected position ε	98
4.9	Bivariate projections of the data shown in Fig 4.8.	99
4.10	Collected photon signal density broken down into ballistic and scattered components.	101
4.11	Comparison of the number of collected ballistic photons to the total number of collected photons as a function of imaging depth.	102
4.12	Axial density at three imaging depths for each of the aperture configurations.	103
4.13	Lateral and axial IQR performance as a function of imaging depth.	105
4.14	Linear array aperture pinhole spacing optimization.	107
4.15	Nipkow aperture pinhole spacing optimization.	108
4.16	Effect on the lateral and axial performance with changing μ_a	109
4.17	Effect on the lateral and axial performance with changing g	110
4.18	Effect on the lateral and axial performance with changing μ_f	111
5.1	Existing lens on the confocal microlaparoscope.	113

5.2	New lens design.	115
5.3	Lens OPD plots.	118
5.4	Field curvature and astigmatism for the extreme conjugates. . .	119
5.5	MTF of the new lens design at the three primary conjugates. .	120
5.6	Tolerance analysis of assembled design at the 15 μm conjugate. .	122
5.7	Lens tolerances and specifications.	122
6.1	Illustration showing how a flat tip bare fiber has problems making uniform contact with tissue.	125
6.2	Illustration showing how a contoured fiber tip can increase contact with tissue.	126
6.3	Three different bare fiber probes developed and tested.	127
6.4	Bare fiber lateral and axial performance with uniform and topical fluorophore.	129
6.5	Axial photon density for uniform fluorophore and topical fluorophore with HWHM 25 μm	130
6.6	<i>Ex vivo</i> human esophagus results using a thirty-thousand element fiber with a hemisphere tip.	131
6.7	<i>In vivo</i> mouse results using a thirty-thousand element fiber with a hemisphere tip.	132
6.8	(VIDEO): <i>In vivo</i> video of mouse esophagus using a thirty-thousand element fiber with a hemisphere tip.	133
6.9	<i>In vivo</i> mouse colon results using a one-hundred-thousand element fiber with a hemisphere tip.	134
A.1	First generation microlaparoscope sketch.	142
A.2	Optical scan unit connector sketch.	143
A.3	First generation microlaparoscope coverslip design.	144
A.4	First generation microlaparoscope multi-lumen housing.	145
A.5	Second generation microlaparoscope flexible design.	146
A.6	Second generation manual focus design.	147
A.7	Third generation microlaparoscope syringe.	149
A.8	Third generation microlaparoscope.	151
A.9	Third generation microlaparoscope. Side view and top view. .	152
A.10	Looking up into the focus coupling inside the motor housing. .	153
A.11	Microlaparoscope handle	154
A.12	Motor housing.	155
A.13	Motor housing cross-section.	156
A.14	Motor housing cover.	157
A.15	Focus connector.	158
A.16	Focus rod.	159
A.17	Syringe plunger.	160
A.18	Lens protector and dye outlet.	161

LIST OF ILLUSTRATIONS - CONTINUED

12

A.19	Wiring diagram. (Page 1)	162
A.20	Wiring diagram. (Page 2)	163
A.21	Wiring diagram. (Page 3)	164
A.22	Microlaparoscope housing quotation. (Page 1)	165
A.23	Microlaparoscope housing quotation. (Page 2)	166
A.24	Lens protector and dye outlet quotation.	167
A.25	Manufacturing details. (Page 1)	168
A.26	Manufacturing details. (Page 2)	169
A.27	Safety approval. (Page 1)	170
A.28	Safety approval. (Page 2)	171
A.29	Safety approval. (Page 3)	172
A.30	Optical scan unit housing (3D).	174
A.31	Optical scan unit housing.	175
A.32	Concept for real-time multi-spectral readout.	176
B.1	Lens layout.	178
B.2	System data. (Page 1)	179
B.3	System data. (Page 2)	180
B.4	Tolerance data. (Page 1)	181
B.5	Tolerance data. (Page 2)	182
B.6	Element 1 drawing.	183
B.7	Element 2 drawing.	184
B.8	Element 3 drawing.	185
B.9	Element 4 drawing.	186
B.10	Element 5 drawing.	187
B.11	Element 6 drawing.	188
B.12	Element 7 drawing.	189
B.13	Lens quotation. (Page 1)	191
B.14	Lens quotation. (Page 2)	192
B.15	Alternative objective space focus design	194
D.1	Method for manufacturing contoured fiber tips.	201

LIST OF TABLES

2.1	System specifications	33
2.2	Comparison of key properties for the three generations of micro-laparoscopes.	40
5.1	New and existing lens properties.	116
5.2	Lens prescription	121

ABSTRACT

The first real-time fluorescence confocal microlaparoscope has been developed that provides instant *in vivo* cellular images, comparable to those provided by histology, through a nondestructive procedure. The device includes an integrated contrast agent delivery mechanism and a computerized depth scan system. The instrument uses a fiber bundle to relay the image plane of a slit-scan confocal microlaparoscope into tissue. The confocal laparoscope was used to image the ovaries of twenty-one patients *in vivo* using fluorescein sodium and acridine orange as the fluorescent contrast agents. The results indicate that the device is safe and functions as designed.

A Monte Carlo model was developed to characterize the system performance in a scattering media representative of human tissues. The results indicate that a slit aperture has limited ability to image below the surface of tissue. In contrast, the results show that multi-pinhole apertures such as a Nipkow disk or a linear pinhole array can achieve nearly the same depth performance as a single pinhole aperture. The model was used to determine the optimal aperture spacing for the multi-pinhole apertures.

The confocal microlaparoscope represents a new type of *in vivo* imaging device. With its ability to image cellular details in real time, it has the potential to aid in the early diagnosis of cancer. Initially, the device may be used to locate unusual regions for guided biopsies. In the long term, the device may be able to supplant traditional biopsies and allow the surgeon to identify early stage cancer *in vivo*.

Nomenclature

ε	Error in collected photon position, page 82
r'_0	Initial photon position at tissue surface, page 81
r_0	Initial photon position in aperture image, page 81
r'_d	Position that fluorescent photon exits tissue surface, page 81
r_d	Position of fluorescent photon in aperture, page 81
r_s	Position of fluorescence emission, page 81
r_{ci}	Final position of collected photon as recorded by detector, page 81
Δs	Photon scatter path length, page 87
δ	Fiber or pinhole center to center spacing, page 106
\varnothing	Diameter, page 121
Γ	Fluorescence extinction coefficient [$\text{cm}^{-1} \cdot \text{L/mol}$], page 86
μ_a	Non-radiative absorption coefficient [cm^{-1}], page 86
μ_s	Scattering coefficient [cm^{-1}], page 86
ξ	Uniformly distributed (0 to 1) random variable, page 83
C	Fluorophore concentration [mol/L], page 86
d	Distance of focal plane below tissue surface, page 86
$F(x)$	Cumulative probability density function, page 83
$f(x)$	Probability density function, page 83
$F^{-1}(x)$	Inverse cumulative probability density function, page 84
f_N	Nyquist frequency, page 119

g	Anisotropy factor, page 86
L	Total photon path length, page 89
l_a	Path length to absorption, page 88
l_f	Path length to fluorescence, page 88
M	Magnification, page 119
n	Index of refraction, page 91
N_c	Number of collected photons, page 92
R	Reflection coefficient, page 88
X	Random variable, page 83
AO	Acridine orange, page 53
CA	Clear aperture, page 121
FDA	United States Food and Drug Administration, page 28
FWHM	Full width half max, page 103
IND	Investigational new drug, page 28
IQR	Interquartile range, page 103
IRB	Institutional review board, page 28
MTF	Modulation transfer function, page 118
NA	Numerical aperture. $NA = n \sin \theta$
OPD	Optical path difference, page 117
OSU	Optical scan unit, page 26
RMS	Root mean square, page 103
MgF_2	Magnesium fluoride (optical coating), page 123

Chapter 1

Introduction

THIS DISSERTATION DESCRIBES THE FIRST clinical confocal microlaparoscope system tested in humans. The instrument's design is described in Chapter 2. Chapter 3 presents *in vivo* and *ex vivo* human results. The results show that the device has the ability to nondestructively resolve cellular and sub-cellular detail and that it has the potential to diagnose cancer *in situ*. Chapter 4 characterizes the system's performance in turbid media using Monte Carlo modeling. Chapter 5 introduces a new miniature objective design for the confocal microlaparoscope and Chapter 6 presents bare fiber confocal probes for imaging locations too small to access with the confocal microlaparoscope.

1.1 Motivation

Cancer frequently goes undetected until it reaches a late, difficult-to-treat stage. Cancers that develop in epithelial cells (carcinomas) are the most common type of malignancy and they account for ninety percent of all hu-

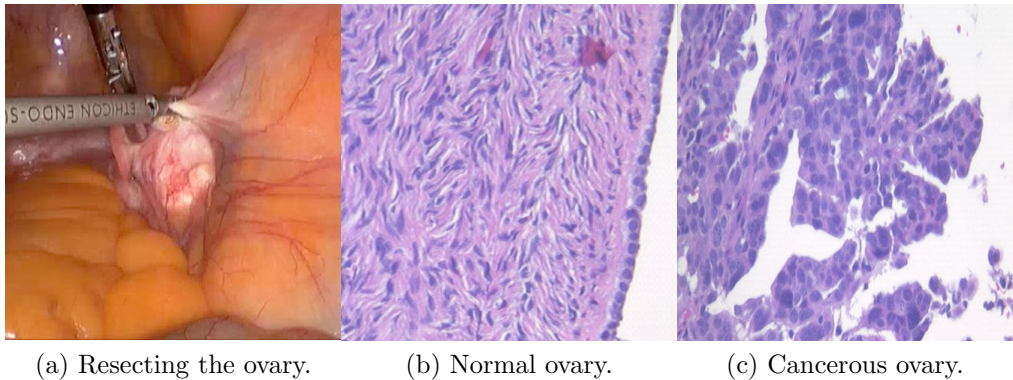
man cancers.[1] Development of imaging devices that can more thoroughly interrogate epithelial surfaces for abnormalities will enable earlier detection of cancer, resulting in significant improvement in patient survival.

The most effective treatments in terms of patient outcomes, quality of life, and cost are those that target cancer during its early development before it has metastasized. Early diagnosis, when the disease is still localized at its origin, results in high cure rates—even for cancers that typically have poor prognosis. Early detection provides the physician with more treatment options and the ability to use less invasive methods. Unfortunately, many cancers are not found until later stages due to inadequate detection methods or low sensitivity diagnostic techniques.

Initial detection and diagnosis of cancer is frequently based on biopsies. Small samples of tissue are removed and a pathologist makes a diagnosis using thin sections of stained and processed tissue. Since biopsies require removal of the tissue, only a limited number can be taken. This leads to significant sampling error, reducing the likelihood of early cancer detection. Development of devices that can non-destructively interrogate epithelial surfaces for abnormalities could reduce this sampling error.

Fig 1.1 illustrates how cancer is currently diagnosed in the ovaries. Fig 1.1(a) shows an ovary being removed to obtain tissue samples for cancer diagnosis. The surface of processed sections of normal ovary (Fig 1.1(b)) have a smooth homogeneous epithelial layer. Processed sections of a cancerous ovary (Fig 1.1(b)) have an irregular heterogeneous cellular distribution.

Conventional bright-field microscopy plays a central role in the diagnosis of disease from carefully prepared biopsy slides. However, when bright-field microscopy is used to image bulk tissue, the images appear blurry due to



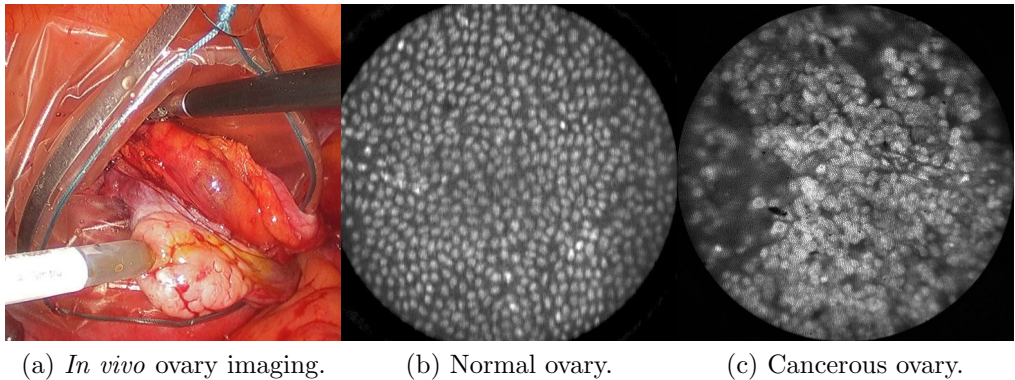
(a) Resecting the ovary. (b) Normal ovary. (c) Cancerous ovary.

Figure 1.1: An ovary is resected (a) and sent to pathology for histological processing. Using standard H&E staining, normal ovaries have the appearance of (b) and cancerous ovaries have the appearance of (c).

simultaneous collection of out of focus planes. Improved imaging of thick samples can be achieved with confocal microscopy. Confocal images of bulk tissue are sharp because light from out of focus planes is rejected via a confocal aperture.

Since the confocal microscope alleviates the need for cutting tissue into thin sections, it has significant potential for *in vivo* imaging of tissue *in situ*. However, a standard confocal microscope is a large device that is not well suited for *in vivo* assessment of epithelial surfaces inside the human body. We have previously reported on technology developed to enable *in vivo* confocal imaging using a coherent fiber optic bundle[2–6]. In Chapter 2, we describe the development of a confocal microlaparoscope.

A confocal microlaparoscope offers the potential for cellular imaging of a wide range of laparoscopically accessible organs. Many organs in the human body can be accessed using a laparoscope via a small incision.[7] Organs that can be accessed in this manner include the stomach, intestines, pancreas, liver, esophagus, spleen, kidneys, peritoneal wall, bladder, gall bladder,

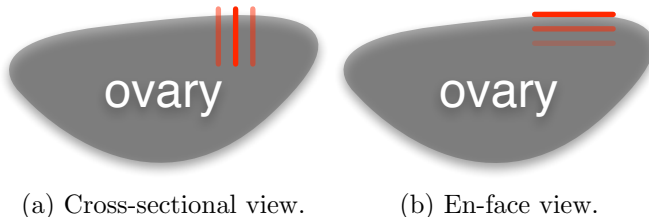


(a) *In vivo* ovary imaging. (b) Normal ovary. (c) Cancerous ovary.

Figure 1.2: An ovary is imaged *in vivo* in real-time using a confocal microlaparoscope in (a). Acridine orange is used as the fluorescent contrast agent; normal ovaries have the appearance of (b) and cancerous ovaries have the appearance of (c).

lymph nodes, reproductive organs in females, and prostate in men. In addition, laparoscopic surgery has significant advantages over open surgery. It minimizes the overall trauma to the skin and muscles, patient recovery time is shorter, and the infection rate is significantly reduced.

Fig 1.2 illustrates how ovarian cancer could be diagnosed *in vivo* using the confocal microlaparoscope. Fig 1.2(a) shows the confocal micro-laparoscope being brought into contact with the ovary *in vivo* for instant cellular imaging. Normal ovary epithelium has a homogenous appearance (Fig 1.2(b)) whereas adenocarcinoma has a distinct loss of the regular cellular structure (Fig 1.2(c)). Although the tissue is viewed en-face rather than in cross-section (see Fig 1.3), the images provide similar diagnostic information as compared to those from histology.



(a) Cross-sectional view. (b) En-face view.

Figure 1.3: Using standard histological processing, tissue samples are viewed in cross-section (a) normal to the tissue surface. The confocal laparoscope captures images en-face (b) parallel to the tissue surface.

1.2 Clinical testing for the early detection of ovarian cancer

In Chapter 3, we present the first known use of a confocal microlaparoscope in humans. We present results from a clinical feasibility study consisting of twenty-one patients. The device was used to image ovaries *in vivo* prior to laparoscopic oophorectomy.

The American Cancer Society estimates that over 230,000 new cases of ovarian cancer were diagnosed in 2007 while more than 141,000 women died from the disease worldwide.[8] For those diagnosed with the disease, only thirty to forty-five percent survive five years.[9] The survival rate for ovarian cancer is poor because there are usually no obvious signs of the disease until it has reached an advanced stage. Over eighty percent of all cases are diagnosed during the later stages (Stage III or IV) of the disease when treatment is expensive and generally unsuccessful.[9] If diagnosis occurs when the cancer is localized to the ovary (Stage I), the five-year survival rate increases to ninety-two percent.

The majority of women who develop ovarian cancer are post-menopausal, but there are also many women who are at an elevated risk for developing

ovarian cancer at a younger age. Risk factors for ovarian cancer include obesity, diet, infertility, a family history of breast, ovarian, or colorectal cancer, and a personal history of breast cancer.[10–14]

Overall, the lifetime prevalence of ovarian cancer is only 1.7 percent.[15] However, the lifetime risk for the disease increases two-fold if the individual has one first or second-degree relative with the ovarian cancer. With two first-degree relatives the risk increases by twenty-five times (a forty percent lifetime risk).[16]

For the subgroups of women at increased risk, few options exist to allow early detection of ovarian cancer. An NIH 1994 consensus stated that there is no single acceptable screening test for ovarian cancer and no evidence that combining the available screening tests—CA125, transvaginal ultrasound, and pelvic exam—leads to acceptable sensitivity and specificity.[17] Ovarian cancer is thought to metastasize early in the course of the disease, often before a lesion in the ovary becomes grossly visible.

Without a viable method for early detection of the disease, women at high risk are given the option of prophylactic oophorectomy. The decision to have a prophylactic oophorectomy is a difficult choice for many women. Removal of the ovaries causes hormonal changes and symptoms similar to those experienced during menopause, though often more severe. Women of reproductive age are no longer able to bear children. Given such severe consequences, women under the age of forty-five who are not at high risk for ovarian or breast cancer are encouraged to undergo hormone replacement therapy. However, this has its own associated risks due to the carcinogenic and coagulative properties of estrogen.[18] In addition, a woman's general quality of life may be affected by early-onset osteoporosis, hot flashes, and

reduced sexual desire.[19]

Several novel techniques are being developed that could provide clinicians with diagnostic tools to detect early changes in ovarian tissue. Techniques, such as confocal microscopy[2, 20–28], two photon microscopy[29, 30], optical spectroscopy[31–36], and optical coherence tomography[37–43] are able to assess tissue morphology and/or biochemical composition. *In vivo* use of these methods has the potential to provide real-time diagnostic information allowing clinicians to assess the subtle changes that occur early in the disease process. These techniques may increase the sensitivity and specificity of a diagnosis, especially when used as a means for targeting traditional biopsies to regions that can be identified as abnormal at the cellular level.

Confocal microendoscopy, an emerging *in vivo* fluorescence imaging technique, can resolve individual cells and has the potential to distinguish between normal and abnormal cellular structure in tissues. The confocal microendoscope is able to image thin sections of thick samples due to its ability to reject light from out of focus planes. This optical sectioning property enables high-resolution microscopic imaging of thick biological samples at moderate depths (typically up to one-hundred to two-hundred microns below the tissue surface).

In vivo confocal imaging has the potential to aid clinicians during screening and/or surgical procedures. Commercial confocal microendoscope systems have recently been developed for visualization of colon and esophagus.[21] Results have been encouraging in these areas and additional applications for this technology are under investigation.

1.3 Statement of authorship and publication intentions

A project of this magnitude is not accomplished alone. Many individuals contributed to the success of this project. The initial concepts for *in vivo* confocal imaging with fiber optic bundles were developed by Dr. Arthur F. Gmitro and Dr. David Aziz in 1993.[2] Dr. Yashvinder S. Sabharwal continued the development of the system and presented a miniature objective lens design in 1999.[4] In 2000 and 2004 Dr. Andrew Rouse presented a new multi-spectral mode for the system and a flexible bench-top microendoscope.[5, 6]

The work presented in this dissertation builds upon the previous work and presents a clinical confocal microlaparoscope. Some of the chapters have been concurrently submitted as manuscripts for potential publication. The following paragraphs describe the dissertation contents that have been submitted for publication and address the specific contributions of the dissertation author.

A clinical confocal microlaparoscope for real-time *in vivo* optical biopsies

The contents of Chapter 2 were submitted as a manuscript (Fig 1.4) to the Journal of Biomedical Optics on February 17, 2009. The manuscript[44], “*A clinical confocal microlaparoscope for real-time *in vivo* optical biopsies*,” is authored by Anthony A. Tanbakuchi, Andrew R. Rouse, Kenneth D. Hatch, Josh A. Udovich, and Arthur F. Gmitro. The introduction and conclusions of the manuscript were integrated into the dissertation introduction and conclusions. The main accomplishment of the paper is a real-time mobile

A clinical confocal microlaparoscope for real-time *in vivo* optical biopsies

Anthony A. Tanbakuchi,^{1,2,*} Andrew R. Rouse,¹ Joshua A. Udovich,^{1,2} Kenneth D. Hatch,³ and Arthur F. Gmitro^{1,2,†}

¹Department of Radiology, University of Arizona.

²College of Optical Sciences, University of Arizona.

³Department of Obstetrics and Gynecology, University of Arizona.

(Dated: February 17, 2009)

Successful treatment of cancer is highly dependent on the stage at which it is diagnosed. Early diagnosis, when the disease is still localized at its origin, results in very high cure rates—even for cancers that typically have poor prognosis. Biopsies are often used for diagnosis of disease. However, because biopsies are destructive, only a limited number can be taken. This leads to reduced sensitivity for detection due to sampling error. A real-time fluorescence confocal microlaparoscope has been developed that provides instant *in vivo* cellular images, comparable to those provided by histology, through a nondestructive procedure. The device includes an integrated contrast agent delivery mechanism and a computerized depth scan system. The instrument uses a fiber bundle to relay the image plane of a slit-scan confocal microlaparoscope into tissue. It has a 3 μm lateral resolution and a 25 μm axial resolution. Initial *in vivo* clinical testing using the device to image human ovaries has been done in twenty-one patients. Results indicate that the device can successfully image organs *in vivo* without complications. Results with excised tissue demonstrate that the instrument can resolve sufficient cellular detail to visualize the cellular changes associated with the onset of cancer.

I. INTRODUCTION

This paper describes the first clinical confocal microlaparoscope system. We describe the instrument and how it evolved during clinical testing. We present both *in vivo* and *ex vivo* results showing that the device has the ability to nondestructively resolve cellular detail and has the potential to diagnose cancer *in situ*.

and a pathologist makes a diagnosis using thin sections of stained and processed tissue. Since biopsies require removal of the tissue, only a limited number can be taken. Sampling error plays a significant role in achieving accurate early detection of cancer. Development of devices that can non-destructively interrogate epithelial surfaces for abnormalities would reduce sampling error.

Many groups are investigating new technologies to

Figure 1.4: “A clinical confocal microlaparoscope for real-time *in vivo* optical biopsies,” submitted for publication.

clinical confocal microlaparoscope system. The microlaparoscope is simple to use during surgery and integrates a contrast agent delivery system and depth scan mechanism inside of the ergonomic handle.

In addition to writing the manuscript, my contributions included:

1. Developing three generations of confocal microlaparoscopes. The process entailed:
 - a) Development of a focus hysteresis correction system. This included integrating a computer controlled motor and developing correction algorithms.
 - b) Development of a reliable focus mechanism.

- c) Development of a reliable contrast agent delivery mechanism.
 - d) Developing an ergonomic and compact handle that contained the focus and dye delivery systems with surgical controls on the outside.
 - e) Wiring and assembling the microlaparoscope.
2. Development of the real-time clinical software.
- a) The software went through three generations. The first generation was written in Python using the PyGame library for the user interface. The second generation used Python with WxWidgets for the user interface. The third generation was a complete rewrite using Objective-C and Cocoa for the user interface.
 - b) The current software consists of over 10,000 lines of Objective-C code (75 characters wide).
 - c) A special memory management class was developed to enable efficient real-time image processing and encoding while allowing the use of garbage collection.
 - d) Code was written to interface with various hardware components including the focus motor, dye delivery motor, scan mirrors, microlaparoscope buttons, and camera.
 - e) Parallelized code for real-time image processing was also developed.
3. I completely redesigned and built the second generation mobile cart.
4. I motivated the development of a more compact optical scan unit (OSU) and worked with Dr. Rouse to implement it. I designed the OSU housing with integrated scan mirror electronics and worked with Dr. Rouse to assemble the unit.

5. I obtained and imaged approximately one-hundred human esophagus biopsies.

Dr. Kenneth Hatch was the primary clinician testing the device *in vivo* for imaging the ovary. Josh Udovich assembled the first generation mobile cart and assembled the flexible bench top catheter used as part of the first generation microlaparoscope. Dr. Rouse and Dr. Gmitro provided input for improving the manuscript.

In vivo imaging of ovarian tissue using a novel confocal microlaparoscope

In vivo imaging of ovarian tissue using a novel confocal microlaparoscope

Anthony A. Tanbakuchi, MS^{a,b}, Joshua A. Udovich, PhD^{a,b}, Andrew R. Rouse, PhD^a, Kenneth D. Hatch, MD^c, Arthur F. Gmitro, PhD^{a,b}

^aDepartment of Radiology, University of Arizona, Tucson, Arizona 85724

^bCollege of Optical Sciences, University of Arizona, Tucson, Arizona 85721

^cDepartment of Obstetrics and Gynecology, University of Arizona, Tucson, Arizona 85724

Abstract

Objectives: Develop a clinical confocal microlaparoscope for imaging ovary epithelium *in vivo* with the long term objective of diagnosing cancer *in vivo*. **Study Design:** The first confocal microlaparoscope was developed and used to image the ovaries of twenty-one patients *in vivo* using fluorescein sodium and acridine orange as the fluorescent contrast agents. *Ex vivo* imaging studies were also carried out. **Results:** The device was tested *in vivo* and demonstrated to be safe and function as designed. Real-time cellular visualization of ovary epithelium was demonstrated. **Conclusions:** The confocal microlaparoscope represents a new type of *in vivo* imaging device. With its ability to image cellular details in real time, it has the potential to aid in the early diagnosis of cancer. Initially, the device may be used to locate unusual regions for guided biopsies. In the long term, the device may be able to supplant traditional biopsies and allow the surgeon to identify early stage ovarian cancer.

Key words: confocal microendoscopy, fluorescence confocal imaging, optical biopsy, ovarian cancer.

1. Introduction

In this paper, we present the first known use of a confocal microlaparoscope in humans. This new type of laparoscope allows surgeons to obtain nondestructive optical biopsies of tissue in real-time. We present results from a clinical feasibility study consisting of twenty-one patients. The device was used to image ovaries *in vivo* prior to laparoscopic oophorectomy.

For the subgroups of women at increased risk, few options exist to allow early detection of the disease. An NIH 1994 consensus stated that there is no single acceptable screening test for ovarian cancer and no evidence that combining the available screening tests—CA125, transvaginal ultrasound, and pelvic exam—has an acceptable sensitivity and specificity.[10] Ovarian cancer is thought to metastasize early in the course of the disease, often before a lesion in the ovary becomes grossly vis-

Figure 1.5: “*In vivo imaging of ovarian tissue using a novel confocal microlaparoscope*,” submitted for publication.

The contents of Chapter 3 were submitted as a manuscript (Fig 1.5) to the American Journal of Obstetrics and Gynecology on March 12, 2009. The manuscript[45], “*In vivo imaging of ovarian tissue using a novel confocal microlaparoscope,*” is authored by Anthony A. Tanbakuchi, Josh A. Udovich, Andrew R. Rouse, Kenneth D. Hatch, and Arthur F. Gmitro. The introduction and conclusions of the manuscript were integrated into the dissertation introduction and conclusions. The main accomplishment of this paper is the successful *in vivo* testing of the confocal microlaparoscope in humans. The results show that the device can resolve cellular morphology.

Beyond serving as the primary author for the manuscript, my contributions included:

1. Interfacing with the clinicians to test the device and determine what improvements were needed.
2. Foreseeing technical or safety issues and rectifying them before problems arose.
3. Preparing the confocal microlaparoscope for surgical procedures.
4. Setting up the equipment in the operating room.
5. Dr. Rouse and I served as the primary individuals who operated the device in the clinic.

Dr. Andrew Rouse worked tirelessly to acquire IRB and FDA IND approval for the clinical trials. Dr. Kenneth Hatch was the primary surgeon testing the confocal laparoscope. Josh Udovich investigated the contrast agent safety and helped with the initial writing of the paper. Dr. Rouse and Dr. Gmitro provided input for improving the manuscript.

Monte Carlo characterization of parallelized fluorescence confocal systems imaging in turbid media

Monte Carlo characterization of parallelized fluorescence confocal systems imaging in turbid media

Anthony A. Tanbakuchi,^{1,2,*} Andrew R. Rouse,¹ and Arthur F. Gmitro^{1,2,†}

¹Department of Radiology, University of Arizona.

²College of Optical Sciences, University of Arizona.

(Dated: March 25, 2009)

This paper characterizes and compares the axial and lateral performance of fluorescence confocal systems imaging in turbid media. The aperture configurations studied were a single pinhole, a slit, a Nipkow disk, and a linear array of pinholes. Systems with parallelized apertures are used clinically because they enable high-speed and real-time imaging. Understanding how they perform in highly scattering tissue is important. A Monte Carlo model was developed to characterize parallelized system performance in a scattering media representative of human tissues. The results indicate that a slit aperture has severely degraded performance, both laterally and axially. In contrast, the analysis reveals that multi-pinhole apertures such as a Nipkow disk or a linear pinhole array can achieve performance nearly equivalent to a single pinhole aperture. Using the model, the optimal aperture spacing for the multi-pinhole apertures was determined. In addition to comparing aperture configurations, the effects of tissue non-radiative absorption, scattering anisotropy, and fluorophore concentration on lateral and axial performance of confocal systems was studied.

I. INTRODUCTION

Parallelized confocal fluorescence systems are becoming more prevalent in the laboratory and in the clinic because they operate at very high speeds enabling video rate imaging and real-time visualization of biological processes.^[1, 2] Confocal microscopes use a small aperture to reject out of focus light, allowing imaging of thin sections within thick samples. Standard confocal microscopes employ a single pinhole aperture that must be

der the same conditions. In addition to characterizing the axial sensitivity of the confocal systems, we study the lateral blur induced by the scattering.

Existing real-time parallelized confocal systems use a variety of aperture configurations that can be broken down into three general types. Fig 1(a) illustrates a serial pinhole aperture and Fig 1(b)-(d) illustrates the general categories of parallelized apertures: slit, Nipkow, and a linear array of pinholes. To collect a two-dimensional image and cover an equivalent field of view (illustrated by

Figure 1.6: “*Monte Carlo characterization of parallelized fluorescence confocal systems imaging in turbid media*,” submitted for publication.

The contents of Chapter 4 was submitted as a manuscript (Fig 1.6) to the Journal of Biomedical Optics on April 13, 2009. The manuscript[46], “*Monte Carlo characterization of parallelized fluorescence confocal systems imaging in turbid media*,” is authored by Anthony A. Tanbakuchi, Andrew R. Rouse, and Arthur F. Gmitro. The introduction and conclusions of the manuscript were integrated into the dissertation introduction and conclusions. The main accomplishment of this paper is the characterization of the confocal microlaparoscope’s slit aperture in turbid media using

a Monte Carlo model. The results show that a slit aperture has degraded performance compared to pinhole based apertures.

I conceived and initiated the study, developed the model, implemented the code (approximately 2,000 lines of optimized C code), setup an XGrid cluster to run the simulations, analyzed the results, and wrote the manuscript. Dr. Rouse and Dr. Gmitro provided input for improving the manuscript.

Chapter 2

Design and development

THIS CHAPTER DESCRIBES THE EVOLUTION of a mobile confocal microlaparoscope imaging system. To demonstrate the device's potential, we present *in vivo* and *ex vivo* human imaging results.

2.1 Clinical confocal microlaparoscope system

We have developed a complete clinical confocal microlaparoscope system that can be wheeled into an operating room and set up to image within a few minutes. The system consists of a confocal microlaparoscope (hereafter referred to as a microlaparoscope) connected to a mobile cart housing an optical scan unit (osu) and control systems. Once the system is running, the surgeon can interrogate regions of interest with the microlaparoscope, view live cellular images on the screen, and selectively record videos, depth scans, multi-spectral images, and still frames. Fig. 2.1 shows the instrument in use in the surgical suite. The mobile cart is on the right and the surgeon using the microlaparoscope is in the middle looking towards the left where



Figure 2.1: The microlaparoscope system imaging the epithelial surface of an ovary during surgery. In this image, the surgeon has located the left ovary using a wide-field laparoscope (left most display) and is inspecting the epithelial cells using the microlaparoscope via the second display from the left. The mobile cart is on the far right.

the gross anatomy is visible on a standard wide-field laparoscope screen. Directly adjacent to this screen is another display showing the live cellular images from the microlaparoscope system.

The microlaparoscope provides live images of excited fluorescence at thirty frames per second with an optical resolution of $3 \mu\text{m}$ laterally and $25 \mu\text{m}$ axially. The system frame rate is fundamentally limited by the acquisition rate of the CCD camera used for detection. Fluorescent contrast agents are delivered locally to the field of view using an integrated contrast agent delivery system. Using controls on the microlaparoscope, the surgeon can adjust focus from the nominal epithelial position down to an optical limit of $200 \mu\text{m}$ below the surface. Table 2.1 provides a detailed listing of the system's specifications.

The evolution from a laboratory system[2, 4–6] to a successful surgical system entailed significant translational research.[47–50] The work can be broken into two major areas: (1) the development of a mobile cart with a

Table 2.1: System specifications.

lateral resolution	3 μm
axial resolution	25 μm
collection elements	30,000
frame rate	30 fps
excitation wavelength	488 nm
spectral collection (150 spectral images)	6 s
average spectral resolution	6 nm
spectral collection	500 – 750 nm
port compatibility	5 mm trocar
dye delivery precision	50 nL
numerical aperture in tissue	0.46
micro-objective magnification	1.5
chromatic correction	488 – 660 nm
maximum imaging depth	200 μm
field of view	450 μm

miniaturized confocal scan assembly (the OSU) and surgical control system and (2) the development of the clinical microlaparoscope. Both areas presented major challenges. The mobile cart required a redesign of the OSU and a change of the laser excitation system from a water-cooled gas laser to a small air-cooled solid-state laser. Making the microlaparoscope easy to use entailed significant developments to tightly integrate the focus and dye delivery systems to ensure quick and reliable response. In addition, the device had to be sterilizable, fit inside standard surgical trocars, and safe to use inside a patient.

In the following sections we describe the mobile cart, the associated systems that it houses, and the functions that it provides. Then we will discuss the evolution of the microlaparoscope beginning with the early prototypes and ending with the state of the art instrumentation currently being used in human clinical trials. Details concerning the integrated in-handle axial focus and contrast agent delivery systems are also presented.

Mobile cart

The mobile cart houses the OSU and the control systems. The instrumentation fits on a standard endoscopy cart that has a 61 cm by 41 cm footprint. Fig. 2.2 depicts the components on the mobile cart. The top shelf houses the sterile microlaparoscope and the surgical supplies that are used during the imaging procedure. The microlaparoscope cable connects to the OSU located on the second shelf. The third and fourth shelves house the laser, function generator, and computer. The bottom shelf houses a medical grade isolation transformer. The operator display and controls for collecting data during surgery are located on a platform at standing height. A second mobile display is placed next to the operative field for viewing by the surgeon.

The system has been designed to streamline all operations during surgery. Once the system is plugged in and the safety interlocks engaged, the system boots and all hardware is initialized. Hardware initialization includes the solid state laser, camera, dye delivery system, focus system, and function generator for scan mirror control. After the automatic initialization, the operator is presented with the software control interface for live imaging.

Optical scan unit

Miniaturization of the OSU required a redesign of the previous bench-top system. By simplifying the optical layout and integrating the multi-spectral imaging segment into a common collection path[51] we were able to fit the whole scan system into a 50 cm by 30.5 cm housing. The housing also integrates the scan mirror power supply and control electronics, which were external in the previous system.

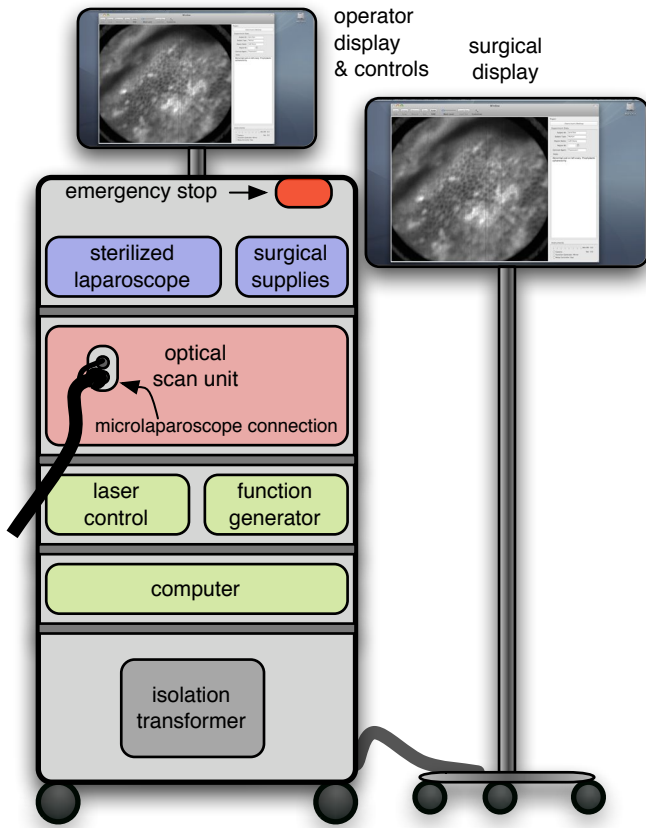


Figure 2.2: Mobile microlaparoscope system. The mobile cart (left) houses the optical scan unit (OSU), surgical supplies, laser source, control systems, computer, and operator controls. The microlaparoscope cable connects to the OSU. The secondary display (right) is placed next to the operative field for live *in vivo* imaging by the surgeon.

The components of the OSU are shown in Fig. 2.3. The top of the figure shows how the system operates in the standard grayscale imaging mode. In this mode, a 488 nm solid state laser beam is expanded and anamorphically shaped into a line via a cylindrical lens. The laser light is then reflected into the image path by a dichroic filter, imaged to a line by a microscope objective, and scanned by the object scan mirror across the coherent fiber bundle face in the microlaparoscope's proximal connector.

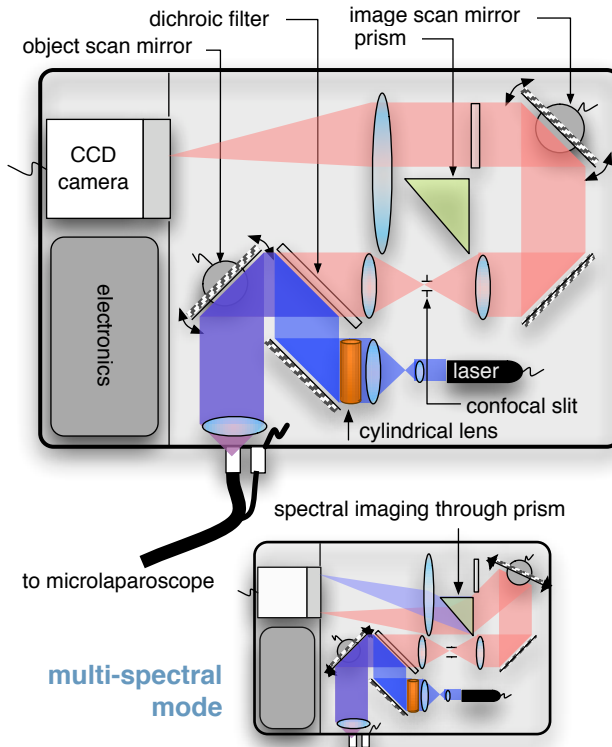


Figure 2.3: Diagram of the OSU. The top portion illustrates the standard grayscale mode of operation. A 488 nm laser is anamorphically shaped into a line and scanned onto the coherent fiber bundle in the microlaparoscope. The excited signal re-enters the system, is descanned and filtered through a confocal slit. The light is rescanned onto a two dimensional CCD camera. In the spectral imaging mode (bottom inset), the image scan mirror is turned to its extreme position redirecting the light through a dispersing prism.

Tissue fluorescence is collected back through the microlaparoscope and de-scanned by the object scan mirror. The dichroic filter passes the fluorescence signal, which is focused down onto a stationary confocal slit. The light exiting the slit is re-collimated and rescanned using the image scan mirror. An emission filter removes residual excitation light. The beam is refocused back into a line that sweeps across the camera to build up a two-dimensional image every thirtieth of a second.

In addition to two-dimensional grayscale imaging, the system can also

collect multi-spectral data.[3, 5, 51] This multi-spectral mode is activated in a fraction of a second via a software actuation button that deflects the image scan mirror to its extreme position (shown in the bottom of Fig. 2.3). During spectral collection the image scan mirror is held stationary. The light passes through a prism dispersing the signal across the CCD. The CCD camera records spectral information in the direction perpendicular to the slit and one dimension of spatial data in the dimension parallel to the slit. The second spatial dimension of the image is collected over time by recording multiple frames as the object scan mirror is slowly stepped. The complete spectral data collection procedure executes in a few seconds. Once spectral collection is complete the system reverts back to grayscale operating mode.

Software control system

A software package that interfaces with the data collection devices and the system controls was written using Objective C 2.0 and Cocoa with automatic garbage collection on Mac OS X. Fig. 2.4 provides a general overview of the software and hardware interface. The software links the surgical controls on the microlaparoscope to the control systems that manage contrast agent delivery, focus, and data acquisition. Parallel processing allows the software to run smoothly while live images are acquired, processed, and encoded at thirty frames per second. A custom image processing memory pool class enables efficient resource management under automatic garbage collection.

Fig. 2.5 shows the software interface. It provides a simple interface for viewing and collecting live images during the surgical procedure. The soft-

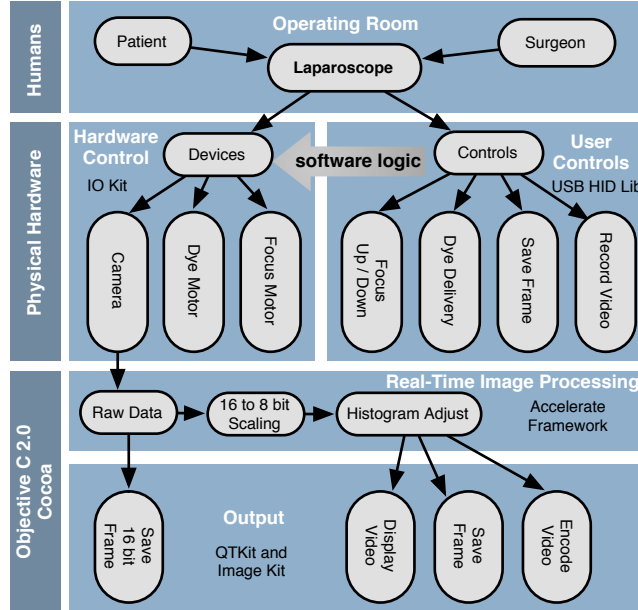


Figure 2.4: Flow diagram illustrating how the software integrates the hardware, live output, and data acquisition components of the microlaparoscope system.

ware has controls to: (1) start live acquisition, (2) save the current frame, (3) record video, (4) deliver dye, (5) load dye, and (6) adjust image display. In addition to the basic controls, the system also records procedure and patient information, which is archived with each image. System information, including image dynamic range and imaging depth, are also visible. During operation the surgeon can easily see real-time imagery on the surgical display (shown in Fig. 2.1) along with the instrument's current status. Contrast agent delivery, focus, and data acquisition can be initiated by the surgeon via integrated controls on the third generation microlaparoscope handle described in the next section.

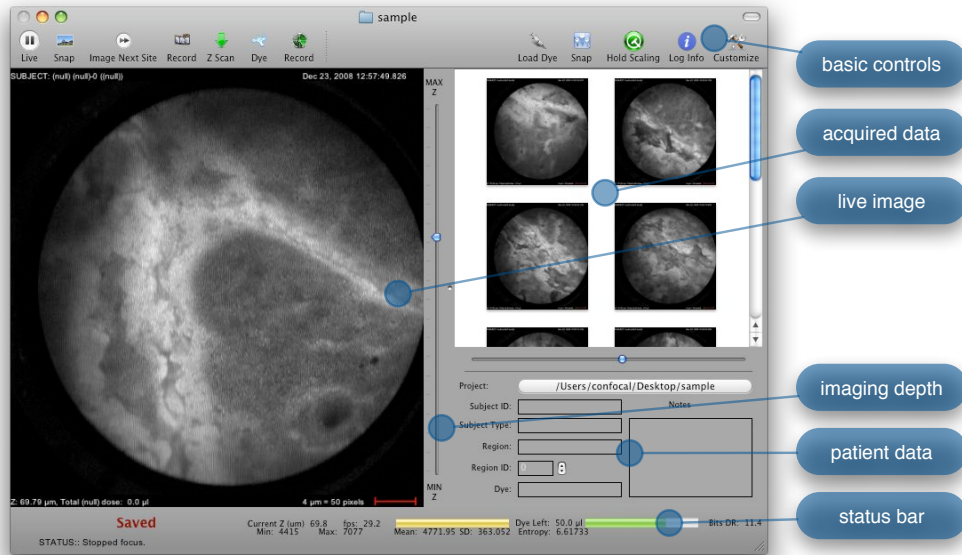


Figure 2.5: Software control system interface. The main window provides the live view and basic controls to run the system. The right side contains previews of data acquired during the procedure along with patient data.

Confocal Microlaparoscopes

Use of the surgical microlaparoscope entails placing the distal end in contact with the tissue, locally delivering fluorescent contrast agents to the field of view, adjusting focus, and collecting the resultant fluorescent confocal image.

To create the surgical microlaparoscope, we had to develop (1) a reliable focus mechanism, (2) a localized contrast agent delivery system, and (3) an ergonomic sterilizable housing with surgical controls compatible with a 5 mm diameter trocar instrument port. The development process encompassed three generations of instruments with the final version meeting all of the requirements. Table 2.2 summarizes the key properties of the three designs.

Table 2.2: Comparison of key properties for the three generations of microlaparoscopes.

	FIRST GEN	SECOND GEN	THIRD GEN
OSU connection	fixed	SMA	SMA
cable length	1.2 m	6 m	6 m
focus type	motorized	manual	motorized
focus control location	cart	handle	handle
focus precision	20 μm	5 μm	0.5 μm
dye control location	cart	handle	handle
dye precision	3 μL	1 μL	50 nL
axial position recording	no	no	yes
z -scan capability	yes	no	yes

In all three designs, the microlaparoscope contains a thirty-thousand element fiber bundle connected via an SMA connector to the OSU. The OSU generates a line of laser illumination that sweeps across the proximal face of the fiber. The fiber bundle spatially relays the illumination pattern to the distal end of the fiber bundle where a miniature 0.46 NA objective lens[6] images the illumination line to the desired tissue depth. Image depth is controlled by adjusting the axial spacing between the fiber bundle and the miniature objective lens. Contrast agent is locally delivered to the tissue through the microlaparoscope. The excited fluorescent signal is collected by the miniature lens and relayed back through the fiber bundle into the OSU.

First generation design

The first generation design—depicted in Fig. 2.6—utilized a sterilizable semi-rigid 5 mm diameter by 500 mm long dual-lumen polycarbonate sleeve through which a non-sterile imaging catheter was inserted[6]. This simple design allowed us to rapidly move to clinical testing by creating a sterile housing for our existing 3 mm flexible imaging catheter. The polycarbonate

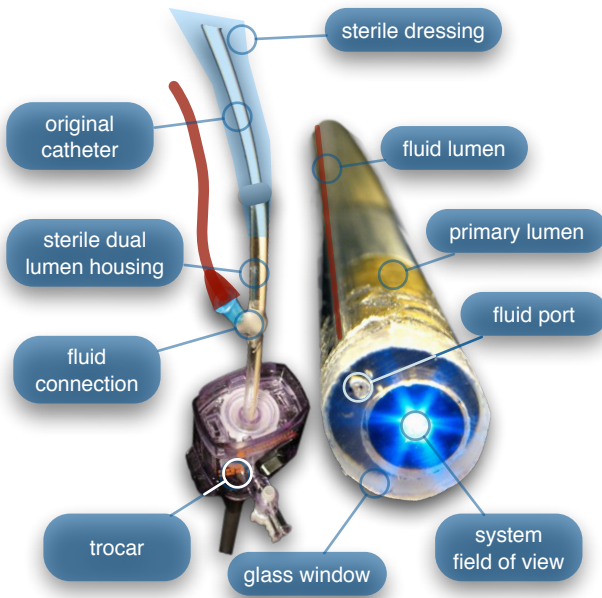


Figure 2.6: First generation microlaparoscope. The front end of the dual lumen polycarbonate housing is shown on the right. The existing imaging catheter is inside the primary lumen with the miniature objective flush against the glass window sealing the face. The secondary contrast agent fluid delivery lumen exits through a laser drilled port in the glass face. The left side of the figure depicts the rear end of the polycarbonate housing passing into a 5 mm trocar port. The dye line and imaging catheter are connected to the rear end of the housing.

also integrated a small secondary lumen to deliver dye locally to the field of view. The front end of the polycarbonate sleeve was sealed with a 160 μm thick glass window. A 500 μm diameter secondary lumen, used to deliver contrast agent, ran parallel to the primary lumen. A 200 μm diameter hole in the window was placed over the secondary lumen allowing contrast agent delivery to the tissue.

The rear end of the polycarbonate housing contained the couplings to mate the imaging catheter and the dye delivery line. In the operating room, the compression coupling of the sterilized polycarbonate housing was

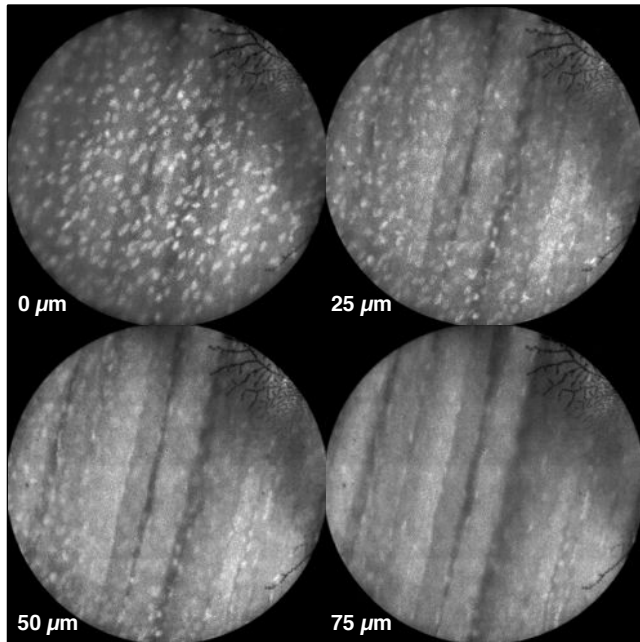


Figure 2.7: Image sequence demonstrating first generation focus control and the confocal properties of the osu. Sequence shows the process of incrementally focusing from the epithelial layer ($0\text{ }\mu\text{m}$) down to the muscle layer of mouse peritoneal wall in $25\text{ }\mu\text{m}$ increments. (Circular field of view is $450\text{ }\mu\text{m}$.)

loosened and the non-sterile imaging catheter was fed through the main 3.1 mm lumen until the miniature objective was in contact with the glass window. The fitting was tightened and then a sterile plastic cover was slid back over the portion of the imaging catheter that was in the operative field. A Luer Lock fitting coupled the fluid lumen to a 0.58 mm medical grade teflon tubing that ran back to the mobile cart.

The 3 mm flexible catheter consisted of a miniature objective lens connected to durable PEEK tubing. The thirty thousand element fiber optic bundle ran through the lumen of the PEEK tubing. Originally, focus was accomplished by a manual micrometer at the proximal end that moved the fiber bundle relative to the PEEK housing. However, focus control was un-

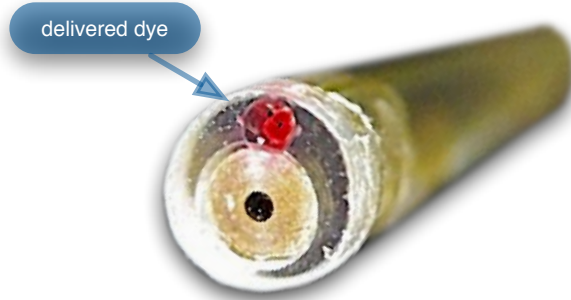


Figure 2.8: Demonstration of contrast agent delivery in the first generation system. Delivery time was approximately one second to deliver a 1 μL volume.

reliable due to an inexact fit of the fiber bundle inside the PEEK tubing. This resulted in hysteresis in the proximal movement of the fiber bundle relative to the fixed lens. Various methods were studied to improve the focus system[5, 6, 49]. Ultimately, the manual focus micrometer was replaced by a computerized stepper motor. A hysteresis correction algorithm was developed to position the distal fiber face with an accuracy better than the system's axial resolution. Fig. 2.7 illustrates the ability of the first generation focus system to image the epithelial surface of tissue (mouse peritoneal wall) and then the controllably focus to underlying cellular layers in 25 μm increments.

Dye delivery was accomplished by loading a syringe with fluorescent contrast agent. The syringe was then inserted into a syringe pump located on the mobile cart. The syringe was connected to the secondary lumen of the polycarbonate housing through 0.58 mm diameter medical grade teflon tubing. Software control of the syringe pump enabled delivery of 1 to 3 μL droplets of contrast agent onto the tissue surface near the field of view of the miniature objective. Figure 2.8 shows a photograph of the distal end of

the microlaparoscope with a droplet of dye coming out through the hole in the glass window.

The device worked well using the 1.2 m length imaging catheter. However, it was determined that a longer length imaging catheter was needed in the operating room. With the longer length catheter, the focus motor and the syringe pump were located far away from the distal microlaparoscope tip and focus would drift during use. Delivery of small droplets of contrast agent was unreliable. The surgeon also noted that positioning the proximal tip accurately was difficult because the polycarbonate housing was not rigid enough.

Second generation design

A second generation device was developed to address the issues concerning device rigidity, focus drift, and reliability of contrast agent delivery across a six meter length connection between the microlaparoscope and the OSU. The second design abandoned the use of the existing flexible imaging catheter. To address the reliability issues of focus and dye delivery in a six meter length device, the controls for focus and dye delivery were located close to the distal tip. To address the rigidity issue, a rigid instrument was made using a stainless steel tube with an inner diameter matching the fiber bundle's outer diameter. Fig. 2.9 shows a diagram of the second generation microlaparoscope.

The miniature objective attached to the distal end of the 3 mm diameter rigid stainless steel tube. The fiber bundle ran through the 1 mm inside diameter of the rigid tube. To focus, the fiber bundle moved axially relative to the fixed lens position. The tube and fiber bundle were held in place by a

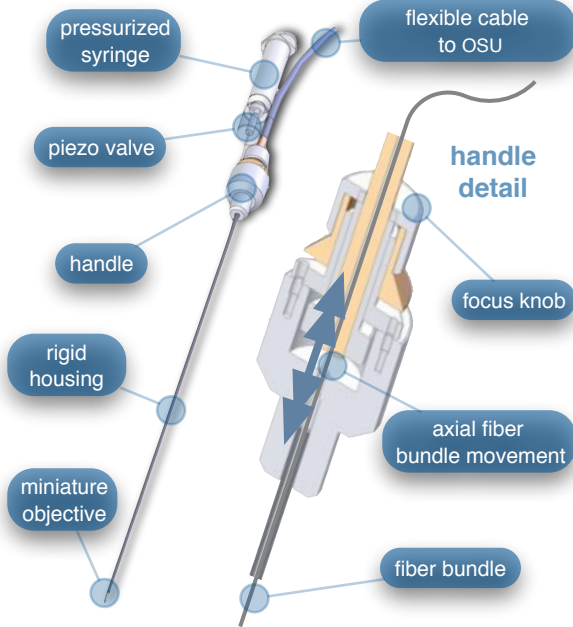


Figure 2.9: The second generation microlaparoscope. The overall device, shown on the left, incorporated a manual focus mechanism and an integrated dye delivery system that uses a piezo valve and a pressurized syringe. The right side shows a cross-section of the depth/focus knob built into the handle.

round handle containing a manual focus mechanism. Rotation of the handle knob resulted in precise movement of the proximal fiber face relative to the rigid tube. To deliver contrast agents, a twenty-one gauge hypodermic tube ran parallel to the 3 mm rigid tube. Both tubes were sealed inside medical-grade FEP heat shrink tubing resulting in a final 5 mm outer diameter. At the distal tip, the hypodermic tube made a ninety degree bend, dispensing contrast agents at the edge of the imaging field. At the back end of the handle, the hypodermic tubing passed into a computer controlled piezo valve immediately downstream from a pressurized syringe. A six meter long flexible cable ran from the handle to the OSU. The cable contained the fiber bundle and piezo valve electrical wires. The proximal end of the

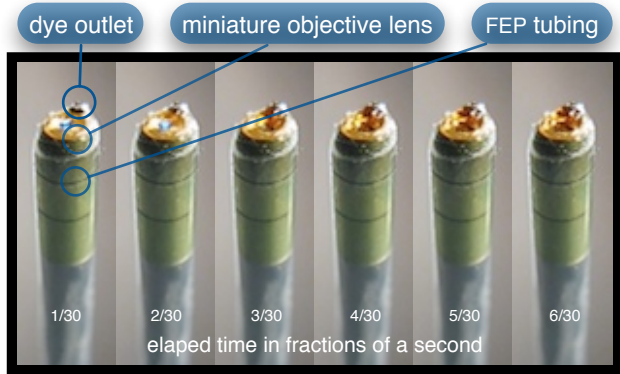


Figure 2.10: Demonstration of the ability of the second generation microlaparoscope to deliver small volumes of contrast agent to the field of view. In this sequence of images, the operator presses the dye delivery button and the dye is delivered to the distal tip via actuation of the piezo valve. The delivered volume in this example is approximately 1 μL .

protective housing broke out into a optical and electrical connectors. An standard SMA connector coupled the fiber bundle to the OSU.

Compared to the first generation system, the second generation system was much easier to use because the whole microlaparoscope could be sterilized and then quickly connected to the OSU in the operating room. In contrast, the first generation system required careful placement of the sterilized polycarbonate housing over the non-sterile imaging catheter permanently connected to the OSU. The rigid stainless steel tubing solved the rigidity issues enabling the surgeon to precisely position the device. A press of a button at the operator console enabled rapid delivery of a small droplet of contrast agent as shown in Fig. 2.10. Focus was extremely reliable and never drifted. In fact, during typical use, the surgeon would set the focus at the epithelial surface and image multiple sites without needing to refocus.

Although the second generation device addressed the primary issues

encountered with the first generation instrument, there were additional improvements that were important to make a successful clinical tool. Even though the manual focus system was reliable, a computerized system was desired to enable depth scans. Second, to allow the device to be controlled more efficiently by the surgeon, the microlaparoscope needed to integrate basic controls for focus, dye delivery, and data recording into the handle. The dye delivery system also needed some refinement. In the second generation device, to ensure repeatable delivery of small contrast agent droplets, the pressure in the syringe had to be well regulated at a relatively high 1.76 kg/cm^2 . This pressure would sometimes cause contrast agent to squirt out of the distal tip rather than pool up in a localized droplet.

Third generation design

To implement these improvements a third generation device was developed. The new microlaparoscope, shown in Fig. 2.11, has an ergonomic handle, control buttons, a computerized focus system, and a refined contrast agent delivery system. Control of focus and dye delivery are consistent and reliable since the control systems were miniaturized and located in the handle only 35 cm from the distal end of the device. A non-pressurized dye delivery system removed the problem encountered with dye ejection.

Mechanically, the third generation microlaparoscope followed the same design principles as the second generation device. Fig. 2.12 illustrates the mechanical aspects of the device. The fiber bundle couples to the focus motor inside the handle. A 1 cm^3 syringe with contrast agent is placed into a spring loaded receiver at the front end of the handle. A second miniature motor in the handle acts as a plunger for the syringe. A spring forces the

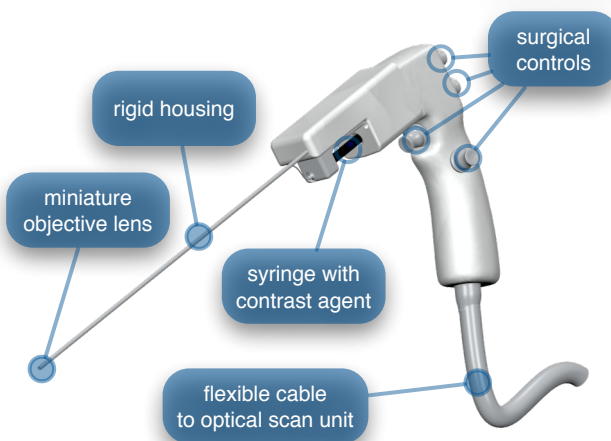


Figure 2.11: The third generation microlaparoscope. In this view, the rigid steel fiber bundle housing is visible entering into the main handle. A spring-loaded receptacle receives a 1 cm³ syringe loaded with contrast agents, which couples into the fluid line running to the distal tip. Four buttons allow the surgeon to control focus, contrast agent delivery, and data acquisition. A six meter length flexible line connects the microlaparoscope back to the OSU.

syringe to mate with a Luer Lock connection that guides the fluid down a twenty-one gauge hypodermic tube.

A customized tip helps to channel the dye and minimize tissue abrasion. The new tip is a 20 mm PEEK housing mated to the FEP outer tubing. A tiny 150 µm lumen inside the PEEK couples the hypodermic fluid line routing the dye to an exit port at the edge of the system's field of view. In the second generation design, the hypodermic tubing was bent around the tip of the miniature objective and had the potential to abrade the tissue surface. The new smooth tip helps to protect the tissue surface and allows the fluid exit port to be placed closer to the edge of the imaging field of view.

The handle contains four ergonomically positioned controls. Two upper thumb controls on the back allow the surgeon to adjust focus and acquire

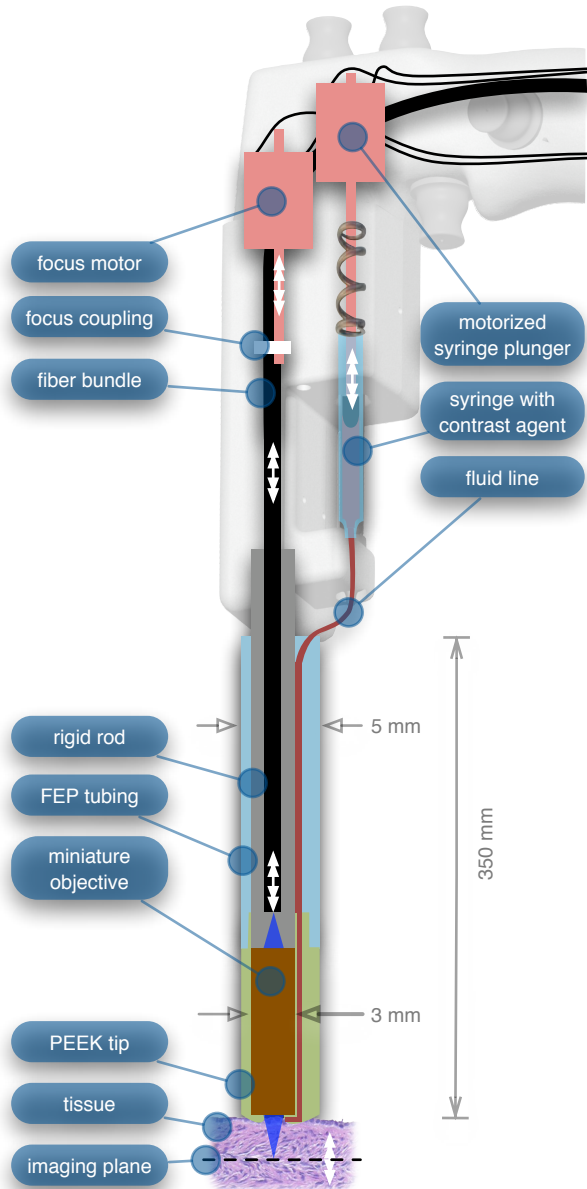


Figure 2.12: Detailed cross-sectional view illustrating the focus mechanism and contrast agent delivery system in the third generation microlaparoscope. The focus motor couples to the fiber bundle causing axial movement of the distal end of the fiber relative to the lens. The motorized syringe plunger forces fluid in the syringe to pass through the fluid line, into the tip, and out the tiny orifice at the edge of the system's field of view. (Diagram not to scale.)

a depth scan. The trigger button saves still frames with a short press and acquires video with a long press. The side button delivers a predefined amount of contrast agent to the field of view.

The electrical wires and the fiber bundle are routed through the handle into a flexible six meter protective cable. The rear end of the cable breaks out into an electrical connector and an SMA connector. Both connections couple to receptacles on the OSU. The electrical connection routes through the electronics of the OSU and exits as a single USB cable connecting to the computer linking the buttons and motors to the control software. The SMA connector couples the fiber bundle to the OSU.

The third generation microlaparoscope represents a viable surgical tool. Its rigid probe enables precise positioning control. The in-handle computerized focus system enables axial focus and depth scans with accurate $1 \mu\text{m}$ positioning. The contrast agent system delivers volumes with precision down to 50 nL . Finally, the whole device has an ergonomic design that is comfortable for the surgeon to use and provides controls for all the tasks that the surgeon may need.

2.2 Results

As previously mentioned, laparoscopic techniques can be used to access most organs in the body. To demonstrate the clinical viability of the confocal microlaparoscope system, we present results from two organs imaged using the device. The first set of results are *in vivo* and *ex vivo* images of the epithelial surface of ovarian tissue. Since there is no reliable way to detect ovarian cancer in its early stages,[17] the microlaparoscope could be

used to detect ovarian cancer in high risk women. The second set of results are *ex vivo* images of human esophagus. Although laparoscopic esophageal surgery is a recent innovation, it is now second only to biliary tract surgery in the frequency of minimally invasive procedures performed in every day surgical practice.[52] The microlaparoscope's ability to visualize the cellular boundaries of tumors could improve the success rates in laparoscopic staging of carcinoma of the esophagus and laparoscopic esophagectomy.

Ovarian images

Currently, the microlaparoscope is being evaluated in a clinical trial to image the epithelial surface of the ovary at the University of Arizona's Medical Center in Tucson, Arizona. The device was granted "*non significant risk*" status by the University of Arizona's Institutional Review Board and has been approved for use in humans using a protocol that includes topical application of contrast agents.[48] To date, twenty-one patients have been imaged *in vivo*.

The current protocol entails imaging human ovaries *in vivo* before oophorectomy or hysterectomy. The imaging protocol begins with the surgeon locating the ovary and isolating it in an endobag with the ovary still connected to the blood supply (see Fig. 2.13). Once the ovary is isolated, the surgeon brings the tip of the microlaparoscope into contact with the epithelial surface. Then the surgeon delivers the contrast agent and live imaging begins. The endobag protects the patient from inadvertent exposure to contrast agent. After the microscopic imaging is done, the surgical procedure is completed as normal and the ovaries are removed. The removed ovary is typically imaged again *ex vivo* using the microlaparoscope with additional

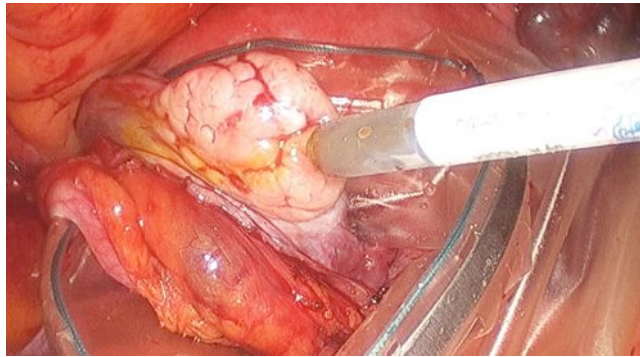


Figure 2.13: Wide-field laparoscope view showing the second generation microlaparoscope contacting the surface of the ovary. The organ, still attached to the blood supply, is laid inside an endobag to protect the patient from inadvertent exposure to contrast agents.

contrast agents. Biopsies are also taken for correlated pathology.

For the initial *in vivo* clinical studies,¹ fluorescein sodium was selected because of its existing track record of safe use in humans.[53, 54] Although fluorescein provides limited diagnostic contrast when applied to the surface of the ovary, it is a safe contrast agent and allowed us to test the safety and basic functionality of the microlaparoscope system *in vivo*.

Fig. 2.14 shows nine examples of *in vivo* images obtained with the microlaparoscope system. The images demonstrate that the device functions as designed. The microlaparoscope can deliver controlled volumes of dye to the image site and then display real-time cellular-level images to the surgeon. The focus mechanism works well. After an initial adjustment of the focus, the instrument can be moved to various sites on the ovary while still maintaining good focus on the epithelial surface.

After *in vivo* imaging with fluorescein, the surgeon removes the ovaries.

¹All patients participating in the clinical trials were consented and imaged in accordance with human subjects protocols approved by the Institutional Review Board of the University of Arizona.

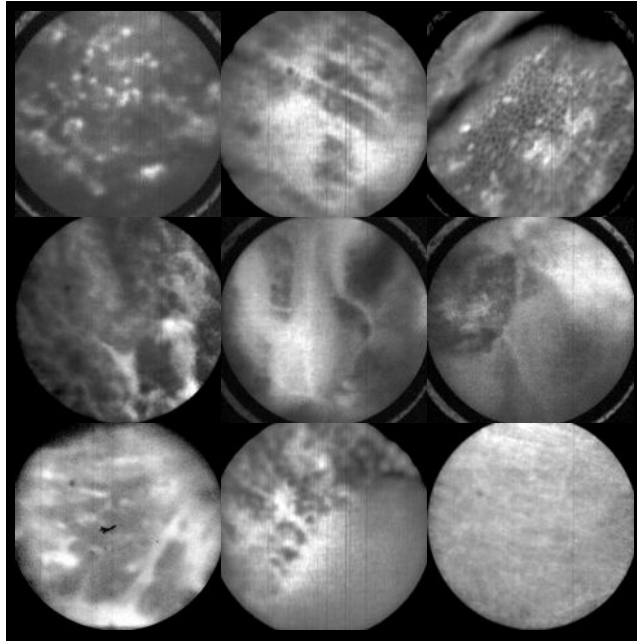


Figure 2.14: Images of ovary epithelium obtained *in vivo* during clinical trials using fluorescein sodium. The low contrast is a result of the minimal preferential binding exhibited by fluorescein. (Circular field of view is 450 μm .)

The ovaries are re-imaged *ex vivo* using acridine orange (AO). Compared to fluorescein, AO provides superior diagnostic contrast. Example images with AO, shown in Fig. 2.15, demonstrate the excellent cellular level contrast achievable with the instrument. The epithelial surface of a healthy ovary is characterized by a homogeneous distribution of bright nuclei as seen in Fig. 2.15(a). The epithelial surface cells of the ovary are delicate and partial denuding can occur, exposing the underlying stroma (Fig. 2.15(b)). Below the epithelial surface, healthy stroma also exhibits a characteristically homogenous structure albeit with a different nuclear size distribution and shape (Fig. 2.15(c)). In the case of ovarian cancer, the tissue structure is visibly different (Fig. 2.15(d)). The epithelial surface is irregular and the high degree of heterogeneity in the size and spatial distribution of nuclei is

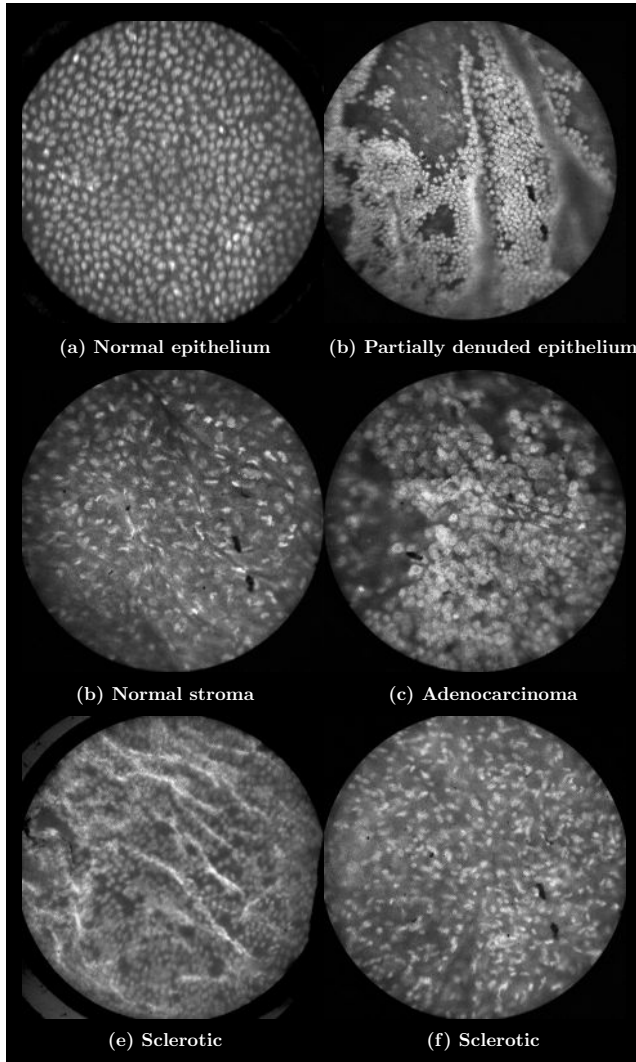


Figure 2.15: Images of human ovary epithelium obtained *ex vivo* using AO. Sub-captions contain pathology diagnosis. (Circular field of view is 450 μm .)

indicative of ovarian cancer.

We have previously shown[55] that the microlaparoscope system can easily differentiate between normal epithelium and ovarian cancer using automated algorithms. It also appears that the microlaparoscope system may be able to visualize cellular changes that happen prior to the onset of cancer. Less distinct tissue changes such as tissue sclerosis may also be

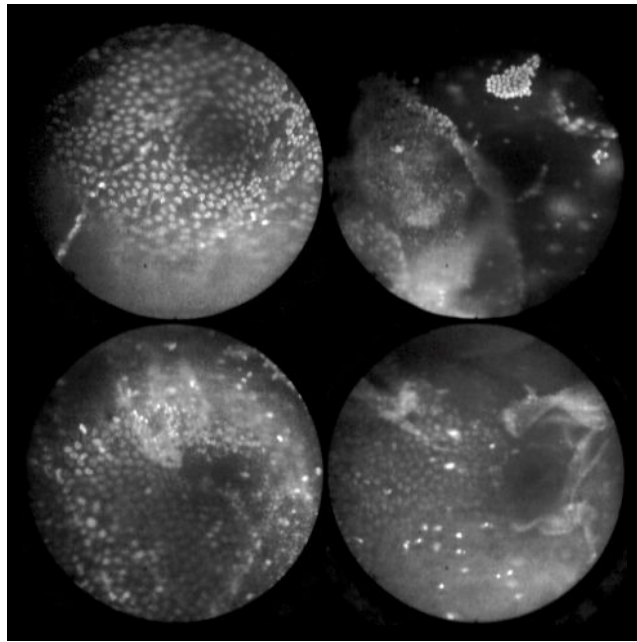


Figure 2.16: Images of ovary epithelium obtained *in vivo* during clinical trials using AO at 330 $\mu\text{mol}/\text{L}$. (Circular field of view is 450 μm .)

detectable (Figures 2.15(e) and 2.15(f)).

With the success of our initial testing with fluorescein, we have now begun imaging *in vivo* with AO.² Fig. 2.16 shows our preliminary results. These images depict the same homogeneous structure of nuclei as seen in Fig. 2.15(a) and (b). Denuding of the delicate epithelium is also visible in some of the images. By optimizing the concentration of AO and giving surgeons more time to practice using the device, we believe we will achieve results comparable to the images obtained *ex vivo*.

Esophagus images

We have conducted *ex vivo* imaging of esophagus tissue biopsies from more than 30 patients. Fig. 2.17(a) shows an example of normal squamous epithe-

²Approval from the FDA to use AO in this context has been granted under IND 102603.

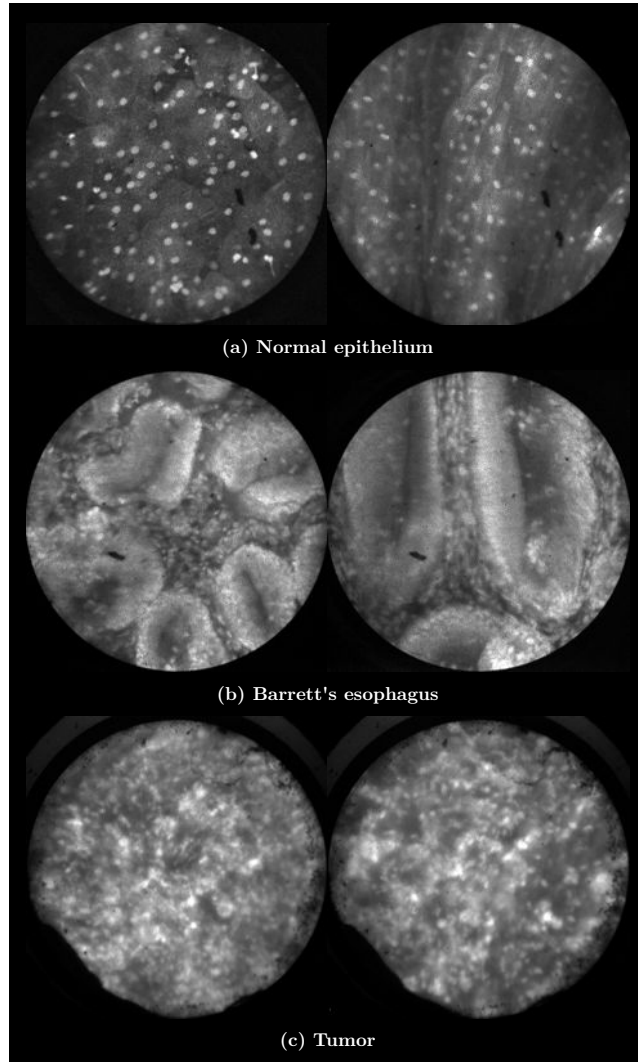


Figure 2.17: Images of human esophagus epithelium obtained *ex vivo* using AO. Sub-captions contain pathology diagnosis. (Circular field of view is 450 μm .)

lium. Fig. 2.17(b) shows epithelial tissue that closely resembles the intestine with columnar appearing mucosa and intestinal metaplasia, a condition known as Barrett's Esophagus. Finally, Fig. 2.17(c) illustrates tumorous esophagus tissue.

These images illustrate the device's ability to resolve the cellular details of tissue in the esophagus. Nuclear distributions are easily characterized

and morphological tissue changes can be readily discerned. In the case of laparoscopic esophagectomy, the microlaparoscope would allow the surgeon to optically biopsy suspect tissues to potentially find locations containing cancer.

Chapter 3

Clinical application and testing

CHAPTER 2 INTRODUCED the confocal microlaparoscope and presented some preliminary results showing the potential for *in vivo* optical biopsy. In this chapter, we discuss the clinical testing of the device in detail.

3.1 Materials and methods

We have previously reported on the development of a multi-spectral fluorescence confocal microendoscope[2, 4–6, 44]. To evaluate whether such a device could be used to image the ovaries *in vivo*, a clinical confocal microlaparoscope system was developed.[47–51] To create a viable clinical system, several criteria had to be met. First, the microlaparoscope system had to be compact and mobile so that it could be quickly moved into the surgical suite. The microlaparoscope also had to be compatible with standard trocars, be sterilizable, have the ability to deliver small localized volumes of contrast agents, and have the ability to focus at selected depths. Finally,

the device had to be comfortable and easy to use during surgery. A confocal microlaparoscope system was constructed meeting these criteria.

To view a real-time cellular image using the confocal microlaparoscope, the surgeon places the rigid probe through a five millimeter trocar port and contacts the epithelial surface of the organ. Pressing a button on the microlaparoscope handle delivers a controlled volume of fluorescent contrast agent to the field of view. Instantly, a live video of the cells appears on screen. As the probe tip is moved across the surface of the organ, the epithelium can be interrogated in real-time. Pressing another button on the handle saves videos and still frames. By default, the system is configured to image the epithelial layer of cells. However, controls located on the handle allow the surgeon to view deeper cell layers. After use, the microlaparoscope can be disconnected from the system, cleaned, and ETO sterilized for reuse.

In the following paragraphs we describe the confocal microlaparoscope system, discuss the fluorescent contrast agents that were used during imaging, and describe the imaging protocol used to test the device.

Confocal microlaparoscope system

The confocal microlaparoscope system consists of a microlaparoscope connected to a mobile cart containing a confocal optical scan unit. The microlaparoscope (shown in Figure 3.1) has a 35 cm rigid probe extending from its handle. The handle contains controls that allow the surgeon to adjust the focus, deliver contrast agents, save still images, and record videos. A flexible cable connects the microlaparoscope to the mobile cart.

The tip of the microlaparoscope's probe contains a miniature 3 mm diameter objective lens that provides a 450 μm field-of-view and a 3 μm lat-

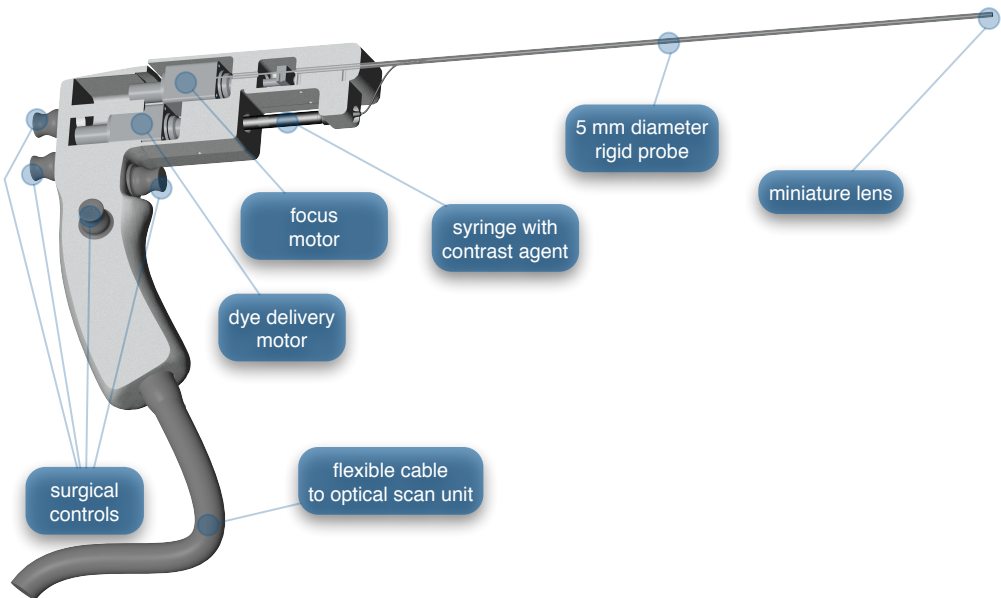


Figure 3.1: The confocal microlaparoscope. Four push button controls located on the handle allow the surgeon to adjust the focus, deliver contrast agents, save still images, and record videos. Inside the handle, two tiny motors control focus and dye delivery.

eral resolution. The miniature objective lens images the tissue plane onto a flexible coherent fiber-optic imaging bundle (Sumitomo Electric Industries, White Plains, NY). The fiber bundle runs through a six meters long cable that connects to the optical scan unit, located on the mobile cart. To adjust the imaging depth in the tissue, the focus motor inside the microlaparoscope's handle changes the spacing between the fiber bundle and the objective lens.

To deliver contrast agent to the imaging site, a syringe with fluorescent dye is placed into a spring-loaded port in the handle of the device. The second motor in the microlaparoscope handle acts as a syringe pump that forces the contrast agent through a tiny fluid delivery line in the rigid probe and onto the tissue. The system is able to deliver dye volumes with a 50 nL

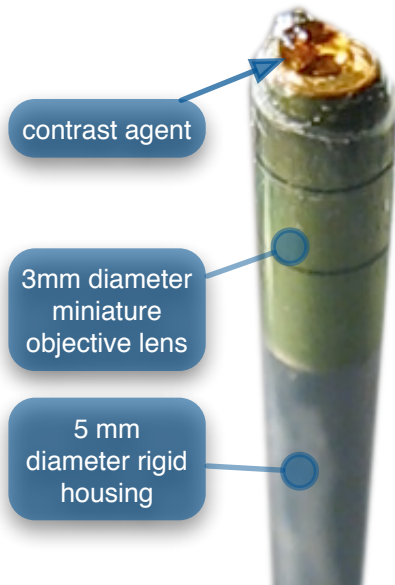


Figure 3.2: Microlaparoscope probe tip. A small volume of contrast agent has been delivered to the device field of view.

precision. Figure 3.2 shows a droplet of dye delivered to the tip of the probe.

The mobile cart, shown in Figure 3.3, contains the optical scan unit, laser, computer, and primary operator console. Live images are visible from the surgical field on a secondary display. The entire mobile unit can be moved into a surgical suite and set up to image within a few minutes.

To collect images, the microlaparoscope illuminates the tissue with laser light. The laser illumination excites the locally delivered contrast agent. Fluorescent signal emitted in the tissue is then collected by the miniature objective lens. The lens images the fluorescent signal onto the distal face of the coherent fiber optic bundle. This signal is then relayed back to the optical scan unit.

The optical scan unit is a high-speed confocal microscope. It contains the laser, scan mirrors, optics, confocal aperture, and detector. The details

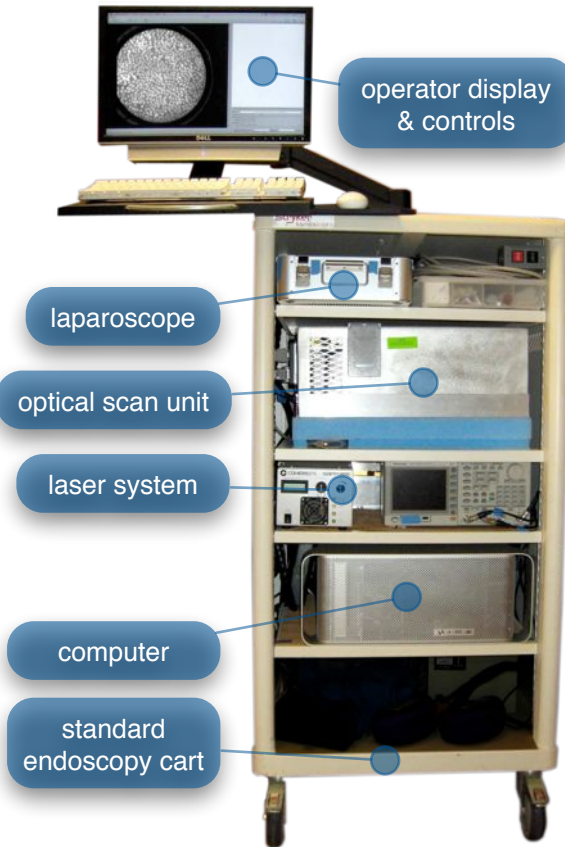


Figure 3.3: The mobile cart. Shelves on the cart, from top to bottom, contain the sterilized microlaparoscope, optical scan unit, laser power supply and system electronics, and computer. The top of the cart holds the operator controls and the primary display.

of the optical scan unit are discussed in [44].

Fluorescent Contrast Agents

Imaging with the microlaparoscope requires the application of an exogenous fluorescent contrast agent. Fluorescein sodium is a dye approved for use in humans for retinal angiography and was selected as the contrast agent for initial testing of the confocal microlaparoscope. The initial clinical study was conducted using approximately 1 to 3 μL of one percent fluorescein

sodium per imaging site. This volume is sufficient for staining a 5 mm diameter area on the tissue surface. The localized application of fluorescein sodium also marks the imaging site for correlated biopsies.

Topically applied fluorescein sodium binds rather non-specifically to proteins in tissue. This results in low contrast images that have limited diagnostic value for detecting ovarian cancer. The ovaries were also imaged using acridine orange (AO) following extraction from the patient. AO is a nuclear stain and an excellent fluorophore for visualizing cellular distributions. Its diagnostic potential has been demonstrated previously in the context of detecting ovarian cancer.[55]

Sites on the ovary that were imaged with fluorescein sodium during the *in vivo* procedure were identified using a UV flashlight to identify locations where the fluorophore had been applied. At nearby locations, approximately 1 to 3 μL of 330 $\mu\text{mol/L}$ AO was applied to the surface of the excised ovary and imaged with the microlaparoscope. These sites were biopsied and processed with standard histopathologic procedures using H&E staining.

Towards the end of the feasibility study AO was used *in vivo* to validate that the same contrast observed *ex vivo* could be obtained *in vivo*. For *in vivo* testing, 1 μL of 330 $\mu\text{mol/L}$ AO was used to image the ovaries using a protocol that prevented any other organ from coming into contact with the dye. This was accomplished by imaging the ovary inside an endobag. FDA approval to use AO in this context was granted under IND 102603.

In the context of this study, AO was used solely to validate that *in vivo* and *ex vivo* contrast was comparable. Although AO has been used clinically on humans in a therapeutic context for the treatment of synovial sarcomas[56], its long term safety when used for diagnostic imaging has

not yet been established. The dye has not been used extensively in clinical application due to concerns about cytotoxicity and mutagenicity; however acriflavine, a related compound, is currently being used for diagnostic imaging of the colon in Germany.[57]. In terms of optical biopsy, cytotoxicity is not a major concern since tissue extraction biopsy, the current approach, is completely destructive to the interrogated tissue. Mutagenicity, on the other hand, is a concern. We have recently completed a pilot study in our laboratory evaluating the safety of AO and SYTO 16 in a mouse model.[58] The results showed no increase in death rate or cancer incidence in animals treated with high doses of dye injected into the peritoneal cavity. However, the power of the study was not sufficient to establish safety. Further study is needed before such a dye could be used clinically in a situation where removal of the ovary is not a predetermined outcome.

Confocal Imaging Procedure

The clinical feasibility study involved twenty-one patients imaged over a one year time period. All procedures in the study were approved by the Institutional Review Board at the University of Arizona. Participants in the study were recruited at the University Medical Center, Tucson, Arizona. Subjects were eligible to participate in the study if they were at least eighteen years of age and not pregnant. All subjects were from the cohort of patients undergoing laparoscopic oophorectomy or open surgery. No financial compensation was offered and there was no diagnostic benefit to the patient for participation in the study.

Standard surgical procedures for clinical oophorectomy were followed with the addition of microlaparoscope imaging prior to ovary removal. Fig-



Figure 3.4: Confocal microlaparoscope imaging the epithelial surface of an ovary *in vivo*. The patient's left ovary has been located using a wide field laparoscope (second display from the left). The surgeon on the right (holding the device in his left hand) has inserted the microlaparoscope through a five millimeter trocar port and placed the tip in contact with the ovary. Live cellular images are viewed on the left most display.

Figure 3.4 shows the microlaparoscope in use during a clinical procedure. All patients were placed under general endotracheal anesthesia and abdominal cavities were insufflated with carbon-dioxide to raise the abdominal wall. The ovary was partially resected and placed inside an endobag to prevent the patient from being exposed to the contrast agent (Figure 3.5). The microlaparoscope was inserted through a 5 mm trocar. Conventional laparoscopic image guidance was used to position the microlaparoscope tip into contact with the ovary. Several locations on the surface of the ovary were interrogated using the confocal microlaparoscope. In all patients, the extra imaging with the microlaparoscope was completed in under ten minutes.

Once the microlaparoscope imaging was complete, the ovaries were re-

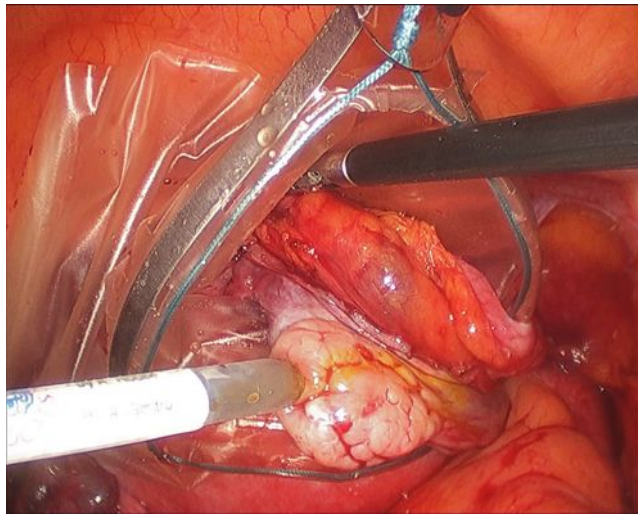


Figure 3.5: *In vivo* imaging of the ovary. Under standard wide field laparoscope visualization, the ovary is located and placed an endobag to prevent other organs from receiving the fluorescent contrast agent. The microlaparoscope (coming in from the lower left) is brought into contact with the ovary, contrast agent is locally applied, and real-time cellular imaging commences.

sected, sealed inside the endobag, and removed as part of the standard surgical procedure. Immediately following removal, the ovary was imaged *ex vivo* with the microlaparoscope using AO as the contrast agent. The ovaries were sent to histopathology for clinical diagnosis.

3.2 Results

Twenty patients were imaged *in vivo* using fluorescein sodium followed by *ex vivo* imaging with AO. One patient was imaged with AO *in vivo*. For the group of patients imaged with fluorescein sodium, seventeen had normal ovaries when evaluated by histopathology and three of the patients were found to have ovarian cancer. No surgical complications occurred in any of the patients imaged with the microlaparoscope.

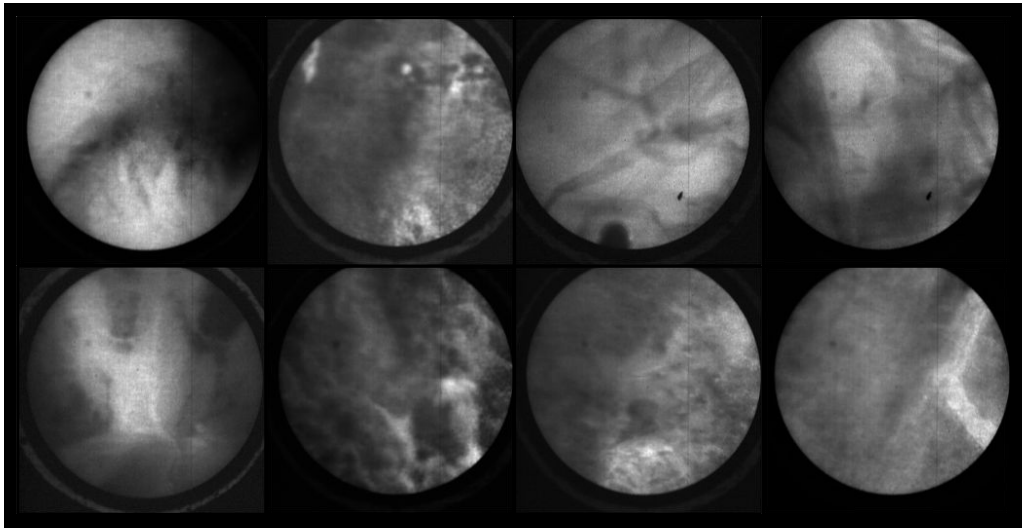


Figure 3.6: *In vivo* confocal microlaparoscope images of the human ovary using topically applied fluorescein sodium as the contrast agent. (Circular field of view is 450 μm .)

In vivo images in Figure 3.6 and an *in vivo* video in Figure 3.7 are from ovary stained with fluorescein sodium. As expected, these images have low contrast because fluorescein sodium binds non-specifically to proteins. Much of the observed contrast can be attributed to the distribution of proteins on the tissue surface and uneven pooling of the dye. Although the contrast was limited, we were able to demonstrate that the focus system and dye delivery system performed properly.

Ex vivo images and videos of ovarian tissue stained with AO are shown in Figures 3.8-3.10. These images and videos were collected on *ex vivo* tissue immediately following removal of the ovary. The results show normal ovarian epithelium in Figure 3.8(a,b) and Figure 3.9, partially denuded epithelium in Figure 3.8(c), normal ovarian stroma in Figure 3.8(d), and adenocarcinoma of the ovary in Figure 3.8(e-h) and Figure 3.10. The bright regions in these images correspond to uptake of AO in the cell nuclei. Nor-

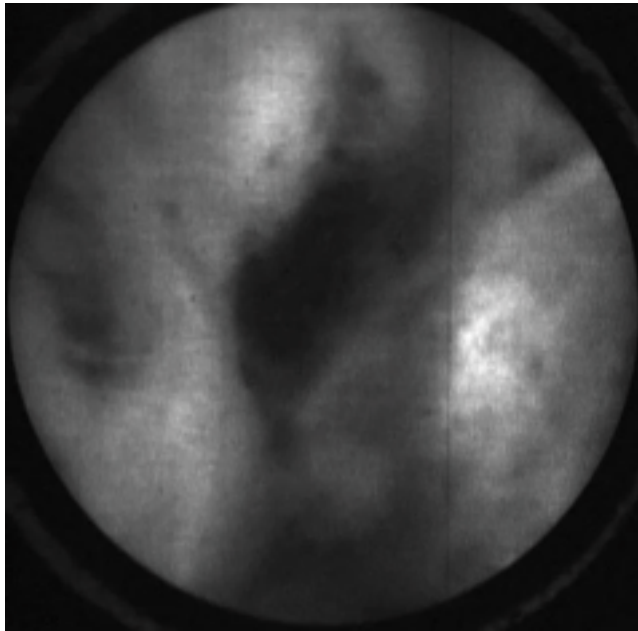


Figure 3.7: (VIDEO) *In vivo* confocal microlaparoscope video of the human ovary using topically applied fluorescein sodium as the contrast agent. The pathology report diagnosis was serous cystadenoma. (Circular field of view is 450 μm .) Video URL: <http://www.tanbakuchi.com/permanent/dissertation/Ch3V1.mov>

mal ovarian epithelium typically has an appearance such as that shown in Figure 3.8(a). The ovary shown in Figure 3.8(b) has smaller nuclei and micro-structural tissue features visible on the surface which may be associated with a cyst that was observed in pathology. Figure 3.8(f) and Figure 3.8(g) were obtained from the same ovary with pathology reporting serous adenocarcinoma and a tumor measuring in excess of 5 mm.

The results suggest that the confocal microlaparoscope has sufficient resolution to differentiate cellular structures and to diagnose cancer. The images show a uniform nuclear distribution for normal tissues and a heterogeneous nuclear distribution for cancerous tissue. The quality of the *ex vivo* images obtained in this study is similar to, if not better than, the image

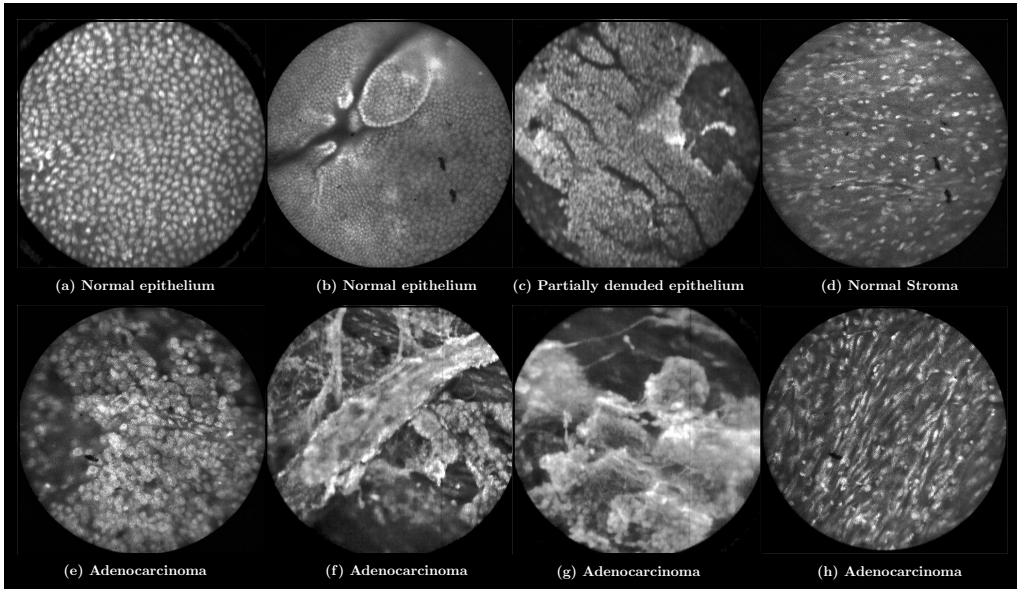


Figure 3.8: *Ex vivo* images of ovarian tissue stained with acridine orange. Sub-captions indicate pathology diagnosis. (Circular field of view is 450 μm .)

quality observed during another *ex vivo* AO imaging study using a previous version of the confocal microlaparoscope that was able to identify ovarian cancer with a 98 percent sensitivity and 90 percent specificity employing computer-aided diagnosis.

Figure 3.11 shows results from the patient imaged *in vivo* using AO. The pathology report diagnosis was serous cystadenoma. The confocal laparoscope's ability to locally identify normal and abnormal regions is highlighted by the two kinds of images obtained in Figure 3.11. The group of results in Figure 3.11(a) have the same appearance as normal epithelium as observed *ex vivo* in Figure 3.8(a). The four images in Figure 3.11(b) appear abnormal and are believed to have been taken in the region that contained the cystadenoma. The dark region visible in the upper right hand quadrant of the images suggests that the probe may not have been in complete contact

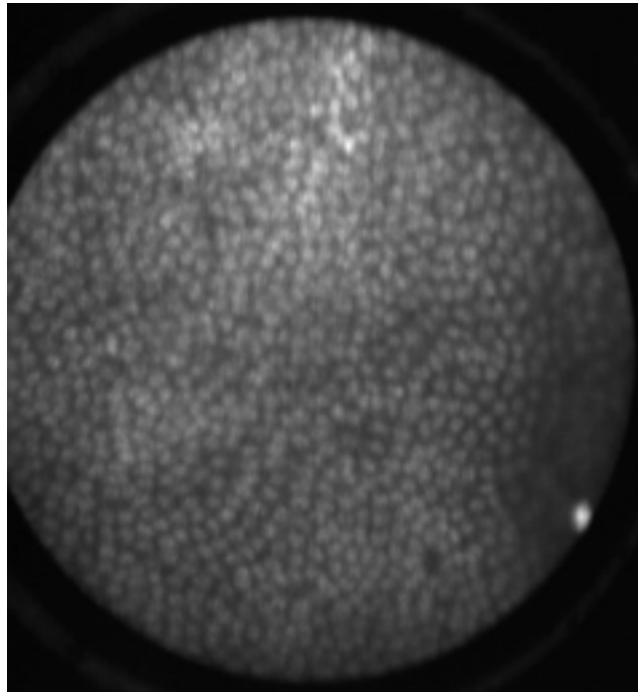


Figure 3.9: (VIDEO) *Ex vivo* video of normal appearing ovary epithelium tissue stained with acridine orange. (Circular field of view is 450 μm .) Video URL: <http://www.tanbakuchi.com/permanent/dissertation/Ch3V2.mov>

with the tissue. Some of the images also appear to show denuding of the epithelium which may be a result of the partial-resection and placement of the ovary in the endobag before imaging. We expect that with further system optimization and more physician practice using the microlaparoscope, the same quality images seen with AO *ex vivo* will be attainable *in vivo*.

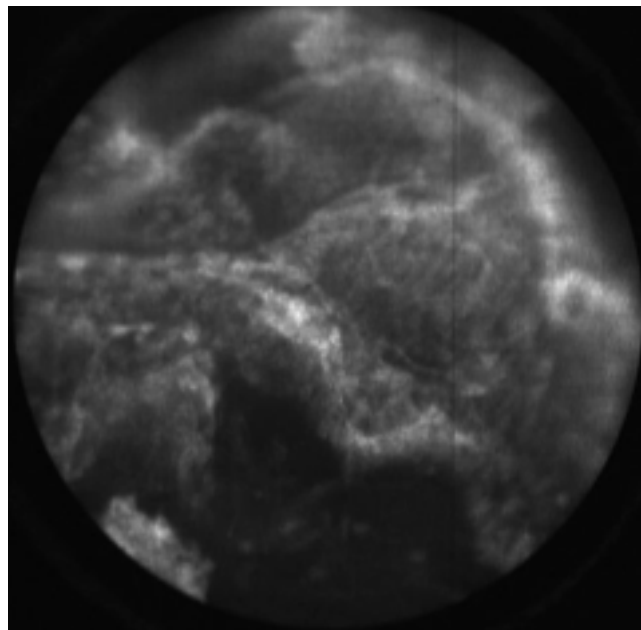


Figure 3.10: (VIDEO) *Ex vivo* video of abnormal appearing ovary epithelium tissue stained with acridine orange. The pathology report diagnosis was serous cystadenoma. (Circular field of view is 450 μm .) Video URL: <http://www.tanbakuchi.com/permanent/dissertation/Ch3V3.mov>

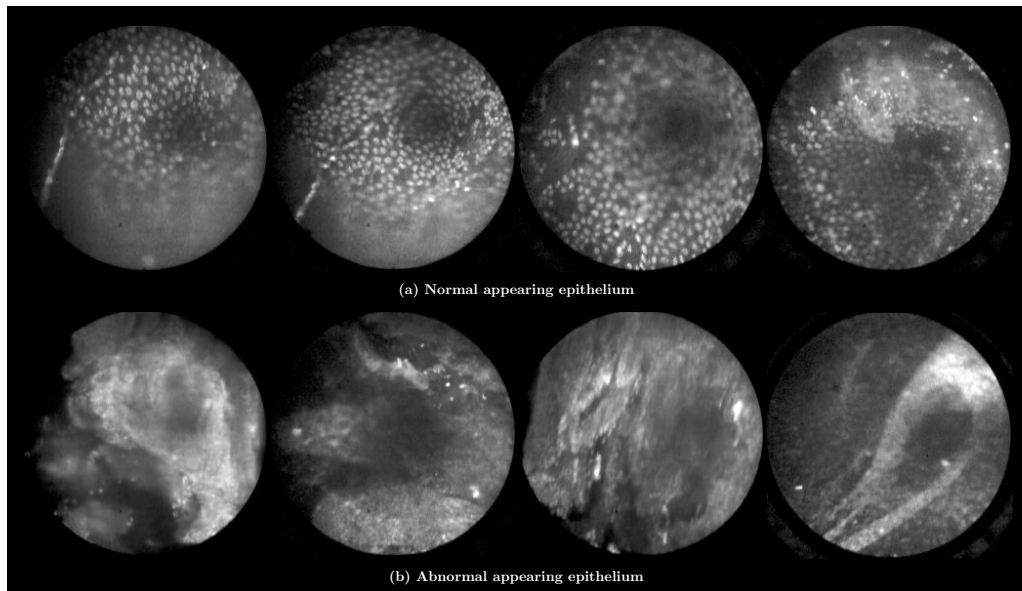


Figure 3.11: *In vivo* images of ovarian tissue stained with acridine orange from the same patient. The top row of images (a) depict epithelial cells that have a normal appearance. The bottom row of images (b) depict epithelial cells that have an abnormal appearance. The pathology report diagnosed the ovaries with serous cystadenoma. (Circular field of view is 450 μm .)

Chapter 4

Monte Carlo analysis

CHAPTERS 2 AND 3 DESCRIBED the development and testing of a slit-scan confocal microlaparoscope for *in vivo* optical biopsy. To better understand the axial and lateral performance of the system, a Monte Carlo model was developed to study the effects of tissue scattering.

4.1 Introduction

Parallelized confocal fluorescence systems are becoming more prevalent in the laboratory and in the clinic because they operate at very high speeds enabling video rate imaging and real-time visualization of biological processes.[44, 59] Confocal microscopes use a small aperture to reject out of focus light, allowing imaging of thin sections within thick samples. Standard confocal microscopes employ a single pinhole aperture that must be spatially scanned to collect a two or three dimensional image. To reduce image acquisition times, parallelized confocal systems use an array of pinholes or a slit aperture to simultaneously collect multiple image points, reducing

acquisition times in proportion to the number of simultaneous detection points used. The drawback of parallelized systems is cross-talk between the individual apertures. In highly scattering media, such as tissue, the cross-talk can be large resulting in a significant reduction in system performance.

Although the theoretical optical sectioning properties of fluorescence confocal systems for various aperture configurations have been studied[60, 61], the actual performance in tissue is typically degraded due to scattering. Previous studies have characterized confocal systems with pinhole apertures in turbid media[62, 63]. However, little work has been done to characterize slit apertures and pinhole array apertures in turbid media. In this paper, we characterize the performance of parallelized confocal fluorescence systems imaging in turbid media. For comparison, we also characterize single pinhole aperture performance under the same conditions.

Existing real-time parallelized confocal systems use a variety of aperture configurations that can be broken down into three general types. Fig 4.1(a) illustrates a single pinhole aperture and Fig 4.1(b)-(d) illustrates the general categories of parallelized apertures: slit, Nipkow, and a linear array of pinholes. To collect a two-dimensional image and cover an equivalent field of view (illustrated by the box in Fig 4.1), each of the four apertures must employ a scanning system. A pinhole aperture requires scanning in two axes. A slit composed of many adjacent detection points requires only one scan axis. Nipkow apertures are large disks with many pinholes that are rapidly rotated to cover the imaging field. Finally, a linear array of pinholes (hereafter referred to as a linear array) requires scanning in two axes like a single pinhole but the range of motion in one axis can be reduced. Each of the parallelized apertures has benefits and limitations in terms of

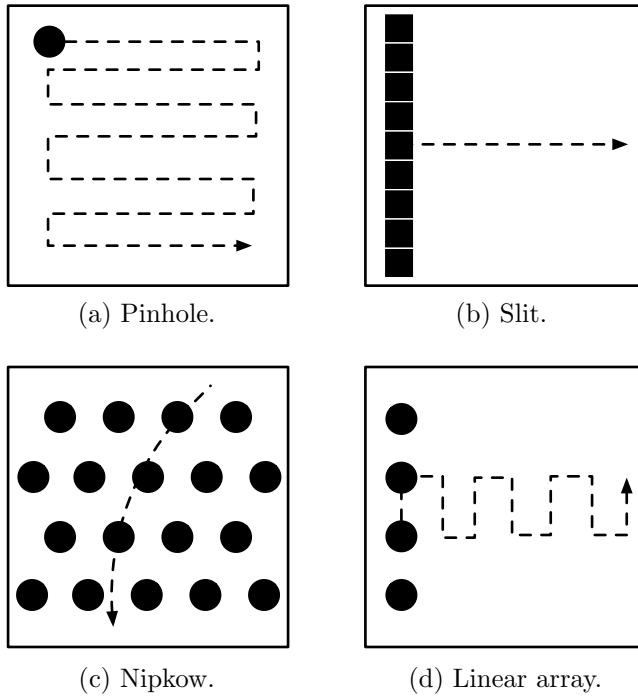


Figure 4.1: Four types of confocal apertures. Dotted arrow shows the scanning patterns required to cover equivalent fields of view.

its light efficiency, optical sectioning, scattering cross-talk, scanning time, and instrumentation complexity.

A Monte Carlo model was implemented that simulates the confocal system shown in Fig. 4.2. The system consists of a laser source and optical elements that uniformly illuminate the confocal aperture. The aperture can be either a pinhole, slit, Nipkow disk, or linear array. The aperture and illumination beam are imaged into the tissue via the objective lens. Fluorescence signal is collected by the objective lens and imaged back onto the confocal aperture. Light passing through the aperture is brought back to focus. A dichroic beam splitter directs the emitted fluorescence signal to a detector. In the case of a pinhole aperture, a single detector is used; in the case of a parallelized aperture, an array of detectors are used.

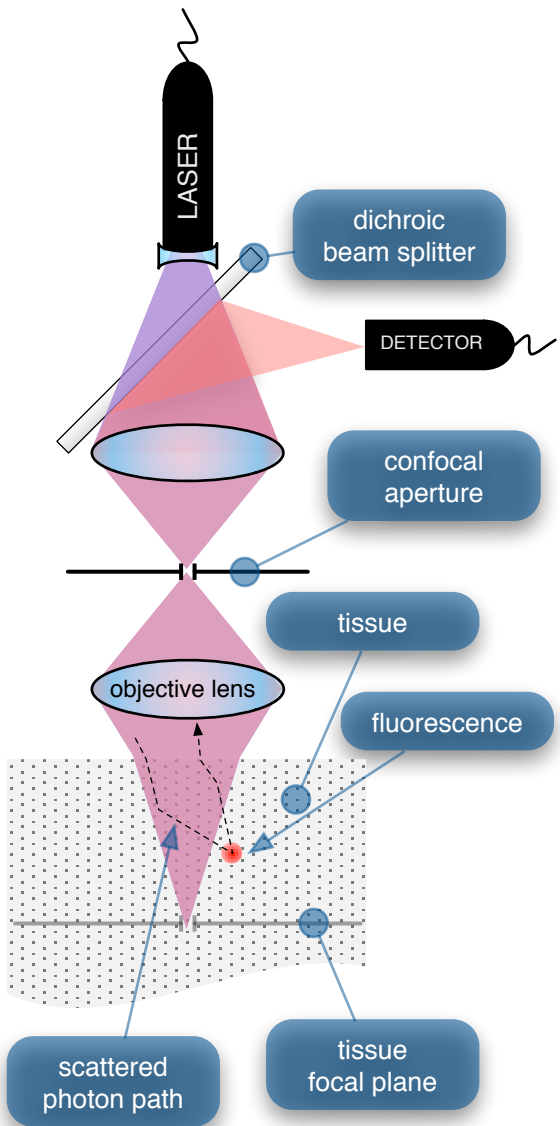


Figure 4.2: Simplified optical layout of a fluorescence confocal system. Cones illustrate non-scattering system illumination and collection beam paths. Dashed line depicts an excitation photon that scatters outside the typical beam path, fluoresces, and couples back into the confocal system.

In a non-scattering medium, a confocal imaging system has the ability to reject a significant amount of light generated away from the plane of focus. Signal generated at the imaging plane comes to focus at the confocal aperture and passes through to the detector. Light coming from a point out of focus produces a defocused beam at the aperture because it is not conjugate to this plane. Thus, a significant proportion of the beam's energy will be rejected by the aperture resulting in reduced signal from out of focus planes. This is what gives the confocal microscope its *optical cross-sectioning* property. Ideally, for a point lying in the plane of focus, all light generated over the numerical aperture (NA) of the objective should pass through the aperture to maximize the collected signal. However, due to diffraction, an infinitely large aperture would be required to collect all the light. Moreover, to reject all light from out of focus planes, an infinitely small pinhole would be required. In practice, a pinhole size somewhat larger than the width of the Airy diffraction pattern will provide a good signal-to-noise ratio and reasonable rejection of background signal.[60]

In a scattering medium, some of the illumination light is scattered out of the beam path increasing the illuminated volume. When induced fluorescence from scattered illumination couples back into the collection path the axial and lateral resolution degrade.

Tissue scattering, non-radiative absorption, and fluorophore concentration all effect the system performance. The excitation beam can scatter before reaching the imaging plane resulting in non-uniform illumination with tissue closer to the surface receiving more excitation energy. This non-uniform illumination leads to an increased probability of fluorescence signal generation near the tissue surface. Tissue non-radiative absorption

and fluorophore concentration amplify the surface bias effect. These effects reduce the energy available for conversion to fluorescence signal at the focal plane. Another event that reduces system performance is scattering of the fluorescence emission. Fluorescence signal generated at out of focus planes can scatter into the collection path reducing the axial and lateral performance.

In the following sections we describe the Monte Carlo model that was implemented to simulate parallelized fluorescence confocal systems imaging in turbid media and then present a comparative performance analysis of the four confocal aperture configurations.

4.2 Monte Carlo model of a fluorescence confocal system

A direct Monte Carlo[64] simulation of individual photons traveling through turbid media was implemented. The model is based on previous work by Wang et al.[65], Wilson and Adam[66], and Prahl et al.[67]. Although variance reduction schemes[68, 69] and multiple independent run methods[70, 71] exist to increase simulation speed, the direct method was chosen because it makes fewer assumptions and is less susceptible to binning artifacts. With modern computers and careful attention to efficient implementation, the direct model was sufficiently fast to generate the required number of photons for accurate modeling.

Conceptually, the direct Monte Carlo model of a fluorescence confocal system imaging in turbid media starts with the creation of an excitation photon in the confocal aperture. The photon's position is randomly gener-

ated using the intensity distribution in the confocal aperture. It's direction is chosen to be within the optical system's numerical aperture. Then the photon is propagated through the system optics until it reaches the surface of the tissue where it refracts and enters the tissue. In tissue, the photon is repeatedly propagated and scattered until it (1) is absorbed and emitted as excited fluorescence energy, (2) is non-radiatively absorbed, or (3) exits the surface of the tissue. When a photon is re-emitted as excited fluorescence, the scattering process continues until the photon is either non-radiatively absorbed or exits the tissue surface. In the case where the photon is absorbed non-radiatively, the photon is terminated. If the photon exits the surface, it refracts and is then traced back through the optical system. If an excited photon makes it into the NA of the collection system and passes through the confocal aperture then it is recorded as collected energy. All other photons that exit the tissue surface are rejected. The process is repeated until a sufficient number of photons are collected to enable analysis of the axial and lateral system response.

Model Principles

The implemented Monte Carlo model makes six assumptions. First, fluorescence emission is assumed to be isotropic[63, 72]. Second, we assume that scattering dominates over diffraction effects so that diffraction can be ignored. Previous studies have shown that this is valid for a confocal system in turbid media.[73]. Third, since the diffraction limited properties of a confocal system are known[61] and we are only interested in studying the effects introduced by scattering, we model the optical system as ideal with uniform aperture illumination and uniform energy across the NA. Fourth,

the detection system is ideal; all collected photons are detected. Fifth, we assume the tissue absorption and scattering properties do not dramatically change between the excitation and emission wavelengths. Sixth, we assume that the fluorophore quantum conversion efficiency is one and that the fluorophore is uniformly distributed on a macroscopic scale in the media.

Because our model assumes an ideal optical system, propagation of the initial photon from the confocal aperture through the optics to the tissue can be done efficiently. Since the confocal aperture is conjugate to the tissue focal plane, we can avoid skew ray tracing and use the magnification between these two planes to move the photon to the imaging plane. Of course, in turbid media there is no direct mapping between these planes, but we can envision that the photon follows a path that satisfies this mapping until it reaches the surface of the tissue. Thus, an efficient approach is to “generate” the excitation photon in the ideal image of the confocal aperture in the tissue focal plane and geometrically back-project the photon to the surface of the tissue. At the surface, the photon’s trajectory and position are the same as they would have been if the photon had been propagated via skew ray tracing through the optical system. Using this same logic, when an fluorescence photon exits the tissue, it is geometrically back-projected to the tissue focal plane where it can be analyzed to determine if it falls within the image of the confocal aperture and the collection NA of the optical system. In other words, the position and angle of this back projected photon will determine if the photon exciting the tissue will be collected by the optical system.

By using this method of generating and collecting the photons, we allow our analysis to be completely carried out in the tissue space. Presenting

results in the tissue space is more intuitive and directly useful for characterizing how the system performs. Moreover, as long as the confocal aperture and lens NA can be described in tissue space, the Monte Carlo model can be described independently of the optical system and its magnification.

Fig. 4.3 shows an example of a photon that is absorbed and re-emitted as a fluorescence photon and then collected by the system. First the excitation photon's spatial position and trajectory are generated randomly in the aperture image at \mathbf{r}_0 . Then the photon is back projected to where it encounters the tissue surface at \mathbf{r}'_0 . At this location, it is launched back into the turbid medium and scattered until it is absorbed by the fluorophore and fluoresces at \mathbf{r}_s . The fluorescent photon's new direction is randomly selected from an isotropic distribution and then scattered until it exits the tissue at \mathbf{r}'_d . To determine if the photon is collected by the system, it is back projected to \mathbf{r}_d . Since \mathbf{r}_d falls within the aperture's opening and the photon's angle is within the maximum collection angle ϕ_{\max} as determined by the NA, the photon is recorded as collected signal. Ideally, in a non-scattering media with an infinitely small pinhole, \mathbf{r}_s will equal \mathbf{r}_d .

To account for the effects of detector sampling, the photon's final position is recorded as the center of the i th pinhole or detector element that it falls within \mathbf{r}_{ci} . Fig 4.4(a) and (b) depict how \mathbf{r}_{ci} is determined for pinhole based apertures. We assume each pinhole has one detector behind it resulting in \mathbf{r}_d being recorded as the center of the i th pinhole \mathbf{r}_{ci} that the photon is collected in. Since a slit aperture has many detectors (Fig 4.4(c)), \mathbf{r}_{ci} is the center of the detector element that contains \mathbf{r}_d . The example shown in Fig 4.3, assumes that the aperture is a single pinhole. Therefore, all detected photons are recorded with the collected position of \mathbf{r}_{c1} .

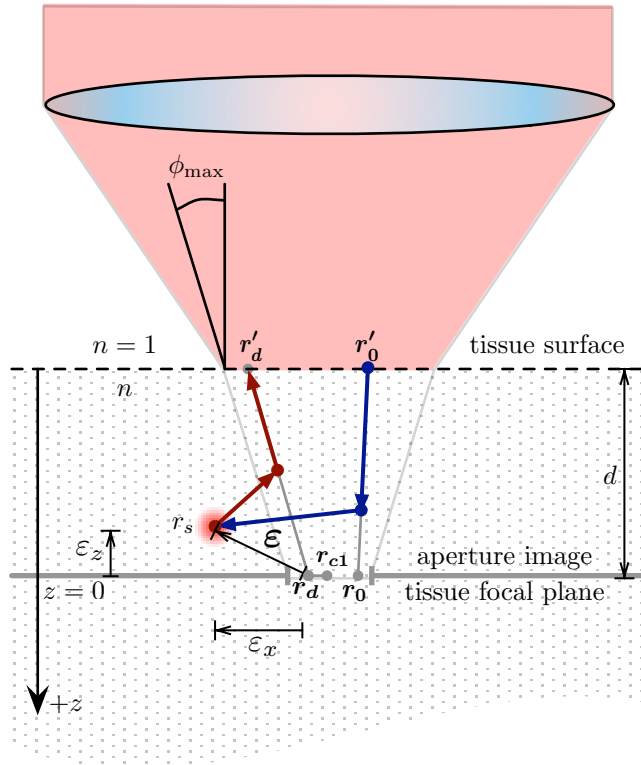


Figure 4.3: Example of a photon that scatters, fluoresces, scatters, and is collected by the confocal system with a single pinhole aperture.

There is an error in the collected signal as defined by the vector $\boldsymbol{\varepsilon} = \mathbf{r}_{ci} - \mathbf{r}_s$. The distribution of ε_z characterizes the axial sensitivity of the confocal system and the bivariate distribution of ε_x and ε_y characterizes the lateral blur induced by scattering. Once \mathbf{r}_d is shifted to the central point in the detection element receiving the photon, the bivariate distribution of ε_x and ε_y also accounts for the detector sampling.

Implemented model

Fig. 4.5 depicts the ten steps in the implemented Monte Carlo model. The model was implemented in C using the GNU Scientific Library[74]. To gen-

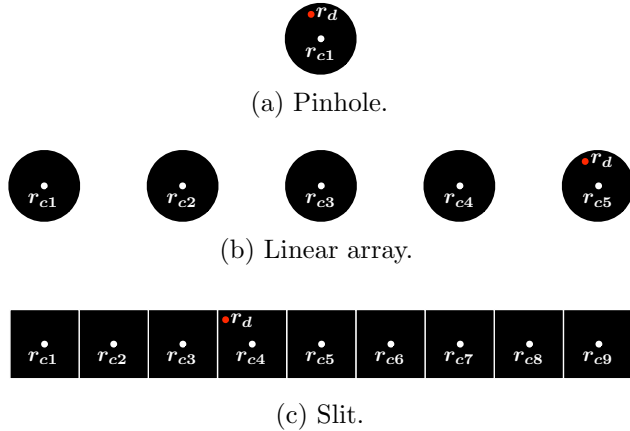


Figure 4.4: Illustration showing the final collected position \mathbf{r}_{ci} of a detected photon incident in an aperture at \mathbf{r}_d . For a single pinhole aperture (a), all detected photons are recorded with a collected position at the center of the aperture \mathbf{r}_{ci} . If a detected photon is inside the fifth pinhole of a linear array aperture (b), its final collected position is \mathbf{r}_{c5} . If a detected photon is inside the fourth detector of a slit aperture (c), its final collected position is \mathbf{r}_{c4} .

erate simulation quality random numbers, a combined multiple recursive generator[75] with a period of 2^{185} (about 10^{56}) was used. To generate results in a timely manner, the code was run on a 40 GHz distributed Xgrid cluster. In the following paragraphs, each step is discussed in detail.

STEP ONE: By mapping the uniformly illuminated confocal aperture to the tissue focal plane ($z = 0$), the initial spatial position of the photon $\mathbf{r}_0 = (x_0, y_0, z_0 = 0)$ can be randomly generated.

In general, a random variable X with an arbitrary probability density function $f(x)$ can be generated using a random variable ξ uniformly distributed between 0 and 1.[76] To generate X , first the cumulative probability density function $F(x)$ is computed using

$$F(x) = \int_{-\infty}^x f(x') dx'. \quad (4.1)$$

Then $F(x)$ is inverted to yield the inverse cumulative probability density

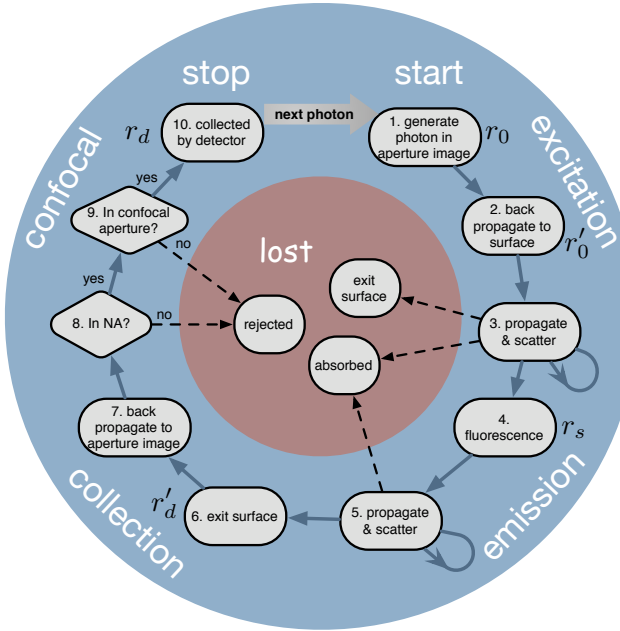


Figure 4.5: Flow diagram for the Monte Carlo simulation of photons through a fluorescence confocal system imaging in turbid media.

function $F^{-1}(x)$. Finally, the random variable X can be generated as

$$X = F^{-1}(\xi). \quad (4.2)$$

Note that in the following sections, each instance of ξ represents a new uncorrelated sampling of a uniformly distributed (0 to 1) random variable.

Since we assume that the aperture is uniformly illuminated, the initial $\mathbf{r}_0 = (x_0, y_0, z_0 = 0)$ coordinates for the photon in the aperture image can be generated for a single pinhole with radius a using

$$a' = \sqrt{\xi \cdot a^2}$$

$$\theta' = \xi \cdot 2\pi$$

$$x_0 = a' \cos \theta' \quad (4.3)$$

$$y_0 = a' \sin \theta',$$

where a' is a random radial distance from the aperture center and θ' is a random angle. To uniformly generate photons in x and y , the random radial position a' must have an increasing probability away from the center. In the case of a linear pinhole array or a Nipkow aperture, first a pinhole in the aperture is randomly selected with equal probability for all pinholes. Then equation set 4.3 is used to find the random offset position for that pinhole. For the slit aperture, x_0 and y_0 are uniformly distributed within the aperture width and height.

Once the initial photon position is generated, its initial trajectory must also be randomly generated. Let the optical axis be along z . Assuming the intensity of the beam does not vary with angle, the trajectory of the photon can be in any orientation in the x - y azimuthal plane and maximally depart from the z axis by the zenith angle $\phi_{\max} = \sin^{-1}(\text{NA}/n)$, where NA and n are the numerical aperture and index of refraction in the turbid media. The initial trajectory can be described with the random variables θ and ϕ which are the zenith angle and azimuthal angle respectively. The azimuthal angle θ has a uniform distribution that ranges from 0 to 2π . The zenith angle requires a uniform sampling of $\cos \phi$ for ϕ ranging from 0 to ϕ_{\max} in order to achieve uniform sampling within the NA.

STEP TWO: This step consists of back-projecting the photon from \mathbf{r}_0 to $\mathbf{r}'_0 = (x', y', z' = -d)$ at the surface of the turbid media so that the scattering process can begin.

In general, to propagate a photon, the new coordinate can be related to

the old coordinate by

$$\begin{aligned}x' &= x + \alpha\Delta s \\y' &= y + \beta\Delta s \\z' &= z + \gamma\Delta s,\end{aligned}\tag{4.4}$$

where direction cosines α , β , and γ are given by

$$\begin{aligned}\alpha &= \sin \phi \cdot \cos \theta \\ \beta &= \sin \phi \cdot \sin \theta \\ \gamma &= \cos \phi\end{aligned}\tag{4.5}$$

and the propagation distance is given by

$$\Delta s = \Delta z / \gamma.\tag{4.6}$$

In this case, we are propagating from $z = 0$ to the surface lying a distance d above, therefore $\Delta z = -d$. Since scattering will begin in the tissue after this point, we need not consider refraction at the tissue surface.

STEP THREE: With the photon position and angle initialized, the propagation and scattering process begins. The photon can be scattered through the semi-infinite volume of the tissue until it is absorbed or exits the surface. The relevant tissue properties are μ_s [cm⁻¹], μ_a [cm⁻¹], and g [unitless], which are the scattering coefficient, the non-radiative absorption coefficient, and the anisotropy factor describing the scattering angle distribution. The fluorophore properties are described by the fluorescence coefficient $\mu_f = \Gamma \cdot C$ [cm⁻¹] which can be expressed in terms of the fluorescence extinction coefficient Γ [cm⁻¹ · L/mol] (assuming a quantum efficiency of one) and the fluorophore concentration C [mol/L].

The mean free path a photon travels before it scatters is $1/\mu_s$. The distribution of path lengths Δs that photons travel before scattering is described by the Beer-Lambert law probability density function

$$f(\Delta s) = \mu_s e^{-\Delta s \cdot \mu_s}. \quad (4.7)$$

To randomly generate an individual path length Δs , equations 4.1 and 4.2 are used to define the generator function for Δs ,

$$\Delta s = -\frac{\ln(\xi)}{\mu_s}. \quad (4.8)$$

Once Δs is generated, the photon is propagated using equation 4.4 to the position at which the scattering event occurs. The scattering event causes the photon to change its trajectory. The azimuthal direction change is described by the uniformly distributed random variable $\Delta\theta$ ranging from 0 to 2π . The change in zenith angle $\Delta\phi$ is modeled using the Henyey-Greenstein phase function[77]

$$f(\Delta\phi) = \frac{1 - g^2}{(1 + g^2 - 2g \cos \Delta\phi)^{3/2}}. \quad (4.9)$$

The random generator computed from equations 4.1 and 4.2 for $\cos \Delta\phi$ is

$$\cos \Delta\phi = \frac{1}{2g} \left(1 + g^2 - \left(\frac{1 - g^2}{1 - g + 2g\xi} \right)^2 \right). \quad (4.10)$$

Jacques et al.[78] has shown experimentally that the Henyey-Greenstein phase function provides a good characterization of single scattering events in tissue. In the limit of $g = 0$ in equation 4.10, scattering is isotropic and $\cos \Delta\phi$ is uniformly distributed between -1 and 1 .

Given the scattered angle $(\Delta\theta, \Delta\phi)$ and the propagation direction (α, β, γ) of the incoming photon, the new direction $(\alpha', \gamma', \beta')$ is given by

$$\begin{aligned}\alpha' &= \frac{\sin \Delta\phi}{\sqrt{1 - \gamma^2}} (\alpha\gamma \cos \Delta\theta - \beta \sin \Delta\theta) + \alpha \cos \Delta\phi \\ \beta' &= \frac{\sin \Delta\phi}{\sqrt{1 - \gamma^2}} (\beta\gamma \cos \Delta\theta + \alpha \sin \Delta\theta) + \beta \cos \Delta\phi \\ \gamma' &= -\sin \Delta\phi \cdot \cos \Delta\theta \cdot \sqrt{1 - \gamma^2} + \gamma \cos \Delta\phi.\end{aligned}\quad (4.11)$$

The propagation and scattering process continues until the photon either exits the surface, is absorbed and re-emitted as fluorescence, or is non-radiatively absorbed. When an incident photon reaches the tissue surface, it reflects back into the tissue with a probability R , where R is the reflection coefficient. The test condition for reflection is $\xi \leq R$. The reflection coefficient R is the average of the Fresnel reflection coefficients for the s and p polarization states

$$\begin{aligned}R &= \frac{1}{2} \left(\frac{n_1 \cos \phi_i - n_2 \sqrt{1 - \left(\frac{n_1}{n_2} \sin \phi_i\right)^2}}{n_1 \cos \phi_i + n_2 \sqrt{1 - \left(\frac{n_1}{n_2} \sin \phi_i\right)^2}} \right)^2 \\ &\quad + \frac{1}{2} \left(\frac{n_1 \sqrt{1 - \left(\frac{n_1}{n_2} \sin \phi_i\right)^2} - n_2 \cos \phi_i}{n_1 \sqrt{1 - \left(\frac{n_1}{n_2} \sin \phi_i\right)^2} + n_2 \cos \phi_i} \right)^2,\end{aligned}$$

where $\phi_i = \cos^{-1} \gamma$ is the angle of incidence, n_1 is the tissue index, and n_2 is the index outside of the tissue. For ϕ_i greater than the critical angle, the photons always reflect back into the tissue. If the photon exits the surface, it is lost since the system rejects non-fluorescence signal.

To determine where the excitation photon terminates in the tissue, the path length to fluorescence l_f , and the path length to absorption l_a , are determined in the same manner that Δs was determined using the random

generator

$$l_f = -\frac{\ln(\xi)}{\mu_f}$$

and

$$l_a = -\frac{\ln(\xi)}{\mu_a}.$$

Note that l_f and l_a are determined only once per photon. If $l_a < l_f$, the photon will be non-radiatively absorbed before it has a chance to be converted into fluorescent energy. Since we are only interested in the distribution of collected fluorescent signal, the photon need not be propagated. If $l_f < l_a$, the photon will be absorbed and re-emitted as fluorescence when its total path length L is equal to the fluorescence path length l_f . The total path length L is the accumulated path length for the number of scattering events

$$L = \sum_i \Delta s_i.$$

Photons with $l_f < l_a$ travel until $L = l_f$ where they are converted into excited fluorescence photons in the next step. If the next propagation step size Δs causes the total path length to exceed l_f , the propagation terminates part way through that path at the point where the total path length equals l_f .

STEP FOUR: When the photon has traveled a distance $L = l_f$, it is absorbed and emitted as fluorescent energy. The position where fluorescence occurs represents the location of the signal and is recorded as \mathbf{r}_s . Since we assume fluorescent emission photons are isotropically generated from the fluorophore, a new photon direction $(\Delta\theta, \Delta\phi)$ is randomly generated with a uniform probability. The photon path length L is reset to zero.

STEP FIVE: Just as in step 3, the fluorescence photon is propagated and scattered through the tissue with random path lengths Δs . The propagation

continues until the photon exits the tissue surface or the photon is absorbed when $L = l_a$ using a newly generated l_a .

STEP SIX: If the fluorescence photon reaches the surface and exits, the scattering process is terminated.

STEP SEVEN: At this step the fluorescence photon is geometrically back-projected from \mathbf{r}'_d on the surface to the point \mathbf{r}_d in the focal plane.

STEP EIGHT: The angle of the photon at the tissue focal plane is compared to the acceptance NA of the optical system to determine if the photon is collected. If the angle of the photon from the z axis is too large, it is rejected.

STEP NINE: The spatial position of the photon is checked to see if it falls within the image of the confocal aperture. If it is outside the aperture, the photon is rejected.

STEP TEN: If the photon is not lost via confocal rejection, NA rejection, absorption, or non-fluorescence, it is detected. To account for the effect of multiple detectors, the final signal position is recorded as the central coordinate of the detector element \mathbf{r}_{ci} that collects the photon (illustrated in Fig 4.4).

Since the modeled tissue is semi-infinite, if the tissue absorption is low enough, it is possible for a photon to scatter many times. A photon that scatters a large number of times has an extremely low probability of being collected because it tends to drift far away from the imaging region. To prevent the simulation from following a photon that has an extremely low probability of being collected in the system, we terminate any excitation photon or fluorescent photon that scatters more than 100 times. In systems where $\mu_a \ll \mu_s$ it is not unusual for an individual photon to undergo a large

number of scattering events. However, under the conditions studied in this paper, it was extremely rare for a photon with more than 100 scatter events to be collected. The performance metrics we use to characterize the axial and lateral response are resistant to rare events, therefore terminating these photons does not effect the results.

With the termination of a photon by collection or it being lost, the process is repeated until the desired number of photons N_c are collected by the system.

4.3 Results and Discussion

The scattering model in the Monte Carlo code was checked by measuring the total reflectance and total transmission for finite slabs of various optical thicknesses and ratios of μ_a/μ_s with matched boundary conditions ($n = n'$). The predicted values were validated against solutions to the radiative transport equation and results of van de Hulst.[79, 80] Total diffuse reflectance and total diffuse transmission were validated against Giovanelli's 1955 results[81] for mismatched boundary conditions (tissue $n > 1$) for a semi-infinite slab bounded by glass slides. Finally, to verify that the fluorescence confocal aspects were correctly implemented, we were able to reproduce the normalized axial intensity functions modeled by Blanca and Saloma[63] for a fluorescence confocal system with a pinhole aperture. Since Blanca and Saloma did not report μ_s , it was not possible to reproduce the same z scale, but the relative intensity shapes and heights matched.

Our primary interest was to compare the axial and lateral performance of parallelized apertures to a single pinhole aperture. In all simulations,

the confocal apertures were uniformly illuminated. We used realistic parameters based on an existing clinical confocal microendoscope for imaging esophagus tissue.[44] An NA of 0.5 in tissue space was used. The simulations were run until the number of collected photons N_c was 100,000 when axial distributions were studied and 10,000 when measures of the lateral and axial distribution's spread were studied. Our results show that the values of N_c were large enough to limit the error of the spread measurements to two orders of magnitude less than the nominal value. To achieve these values of N_c for all configurations presented in this paper, some simulations had to generate in excess of 1.5 billion photons. The analysis and visualization of the data were accomplished with R.[82]

The four apertures were specified in terms of their size in tissue space for a system designed to image a 450 μm square region. The pinhole aperture was 1.5 μm in diameter. The slit aperture was 1.5 μm by 450 μm with the long dimension oriented along y . Inside the slit, three hundred 1.5 μm square detectors recorded signal in parallel. The linear array consisted of a line of pinhole apertures 1.5 μm in diameter spaced 30 μm center-to-center, spanning 450 μm (fifteen pinholes total). For the Nipkow aperture, a two-dimensional array of sixty 1.5 μm apertures were spaced 60 μm apart. The linear array and the Nipkow apertures were optimized to maximize the number of apertures while maintaining performance comparable to a single pinhole aperture down to an imaging depth of 62.5 μm . The optimization of the linear array and Nipkow apertures is discussed in section 4.3.

For a pinhole aperture system, an approximate formula for the optimum pinhole radius as determined by the half-power width of the Airy diffraction

pattern in tissue space is[60]

$$a = \frac{0.25\lambda}{\text{NA}}. \quad (4.12)$$

For a confocal system with an NA of 0.5, the optimal pinhole diameter would be 0.633 μm , assuming λ is 632.8 nm. The pinhole diameter in the modeled system is larger because better signal efficiency is achieved with radii greater than that given by Equation 4.12.

We simulated human esophagus tissue for a range of imaging depths below the tissue surface. Because tissue and fluorophore properties can vary significantly, we analyzed a range of typical tissue and fluorophore parameters μ_a/μ_s , g , and μ_f/μ_s to show how they affect the results. We did not study the effects of the tissue index n since it does not substantially vary and it only effects the fresnel reflections at the surface of the tissue.

Unless otherwise specified, we present results for esophagus tissue at a wavelength of 632.8 nm with values $\mu_s(1 - g) = 12 \text{ cm}^{-1}$, $\mu_f = 40 \text{ cm}^{-1}$, and $\mu_a = 0.4 \text{ cm}^{-1}$.[83] The optical index of refraction modeled was $n = 1.37$.[84] For a typical tissue value of $g = 0.85$, the scattering coefficient is $\mu_s = 80 \text{ cm}^{-1}$. We also assume the average fluorophore concentration is uniform throughout the tissue with $\mu_f = 0.5\mu_s$. Our analysis used a nominal imaging depth of $d = 62.5 \mu\text{m}$. However, the results can be generalized for other tissues with different scattering coefficients by expressing the imaging depth in terms of the average number of mean free paths $d \cdot \mu_s$. Similarly, we can generalize the axial error from focus ε_z as the average number of mean free paths from focus $\varepsilon_z \cdot \mu_s$.

Our approach in modeling the fluorophore concentration as uniform throughout the tissue is different than previous approaches. Others have

modeled a high frequency fluorescence pattern in the tissue or modeled a plane of fluorescence that is moved through the plane of focus. Modeling a high frequency fluorescent pattern makes the results dependent on the pattern that was used. A fluorescent plane moving through focus masks the effects of decaying excitation signal due to the absorption of photons at planes above the plane being analyzed. Real tissue will have spatially varying fluorescence due to the cellular structure, but modeling a uniform concentration of fluorophore throughout the tissue approximates the fluorescence as an average fluorescence signal over a volume. This results in simulations that realistically characterize axial sensitivity and properly account for decaying signal with depth due to fluorescence and non-radiative absorption.

Characterizing aperture imaging performance

Fig 4.6 (movies) shows the three dimensional distributions[85] of the collected fluorescence photon signal positions \mathbf{r}_s for the four aperture configurations imaging in simulated tissue at an imaging depth of $d \cdot \mu_s = 0.5$ mean free paths (62.5 μm). In each of the figures, the tissue surface lies in the x - y plane at $z = -62.5 \mu\text{m}$ and the plane of focus is at $z = 0$. Fig 4.6(c) and Fig 4.6(d) appear more granular than the single pinhole result in Fig 4.6(a) because the same number of collected photons is distributed over a larger area.

Fig 4.7 shows the projection[86] of the the collected fluorescence photon signal \mathbf{r}_s onto the x - y plane. This plot identifies how much signal is collected outside the aperture. Although the signal is extremely large within the aperture, the distribution of energy outside the aperture indicates blur-

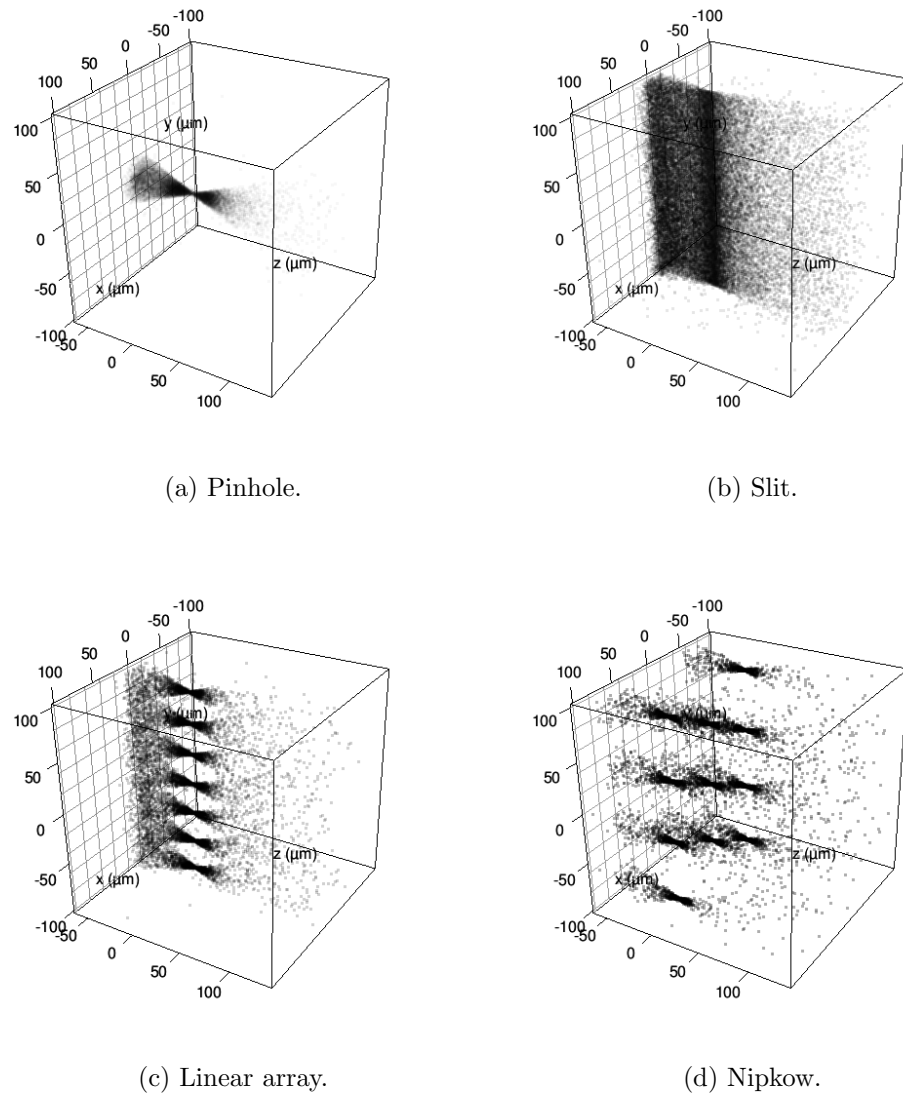


Figure 4.6: (VIDEO) Movies of the three-dimensional distribution of collected photon signal positions \mathbf{r}_s for each aperture configuration in simulated tissue. Tissue surface is at $z = -62.5 \mu\text{m}$ (grid plane), focus is at $z = 0$. Video URL: <http://www.tanbakuchi.com/permanent/dissertation/Ch4V1.mov> (QuickTime 5.1 MB)

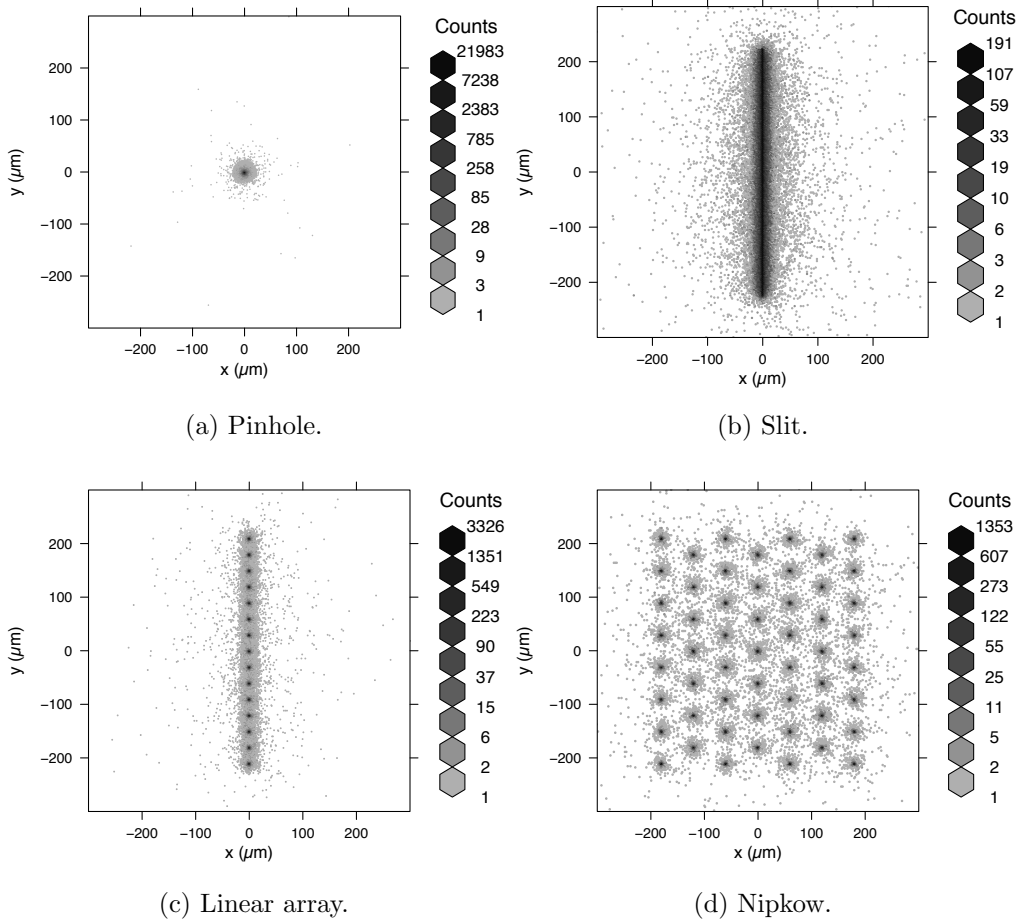


Figure 4.7: Lateral x - y signal distribution for \mathbf{r}_s for each aperture configuration in esophagus tissue. Note log color map scale.

ring due to scattering. The slit aperture has the most spread out signal, indicating a substantial lateral blur. Both the linear array and the Nipkow aperture have a distribution of photons centered around each aperture that seems comparable to the single pinhole aperture.

It is difficult to directly compare the performance of the aperture configurations using the distribution of fluorescence photon locations shown in Fig 4.6 and Fig 4.7. A better comparison can be made by plotting the error distribution of photon positions $\boldsymbol{\varepsilon} = \mathbf{r}_{ci} - \mathbf{r}_s$ as shown in Fig 4.8. In an ideal

confocal system, $|\epsilon|$ should be zero for all collected fluorescent photons. As the distribution of ϵ_z broadens, the axial performance of the system decreases. Similarly, as the distribution in the lateral plane broadens, the lateral resolution performance of the system degrades.

Compared to the pinhole aperture in Fig 4.8(a) the slit aperture in Fig 4.8(b) shows significant error, especially near the surface. Fig 4.8(b) also shows an interesting V-shaped region of sensitivity error moving away from the surface. The parallelized pinhole apertures in Fig 4.8(c) and (d) appear to have distributions nearly identical to the single pinhole except for some subtle signal at intervals of the pinhole spacing.

To more quantitatively compare the aperture performance shown in Fig 4.8, the data are presented in Fig 4.9 as projections of ϵ on the axial planes $\epsilon_z-\epsilon_x$ and $\epsilon_z-\epsilon_y$ and the lateral plane $\epsilon_x-\epsilon_y$ for the four aperture configurations. Since the majority of the energy is localized near $\epsilon = 0$, the plots are shown with a log color scale.

The axial plots (left and center columns) in Fig 4.9 show that the apertures have a strong sensitivity within the NA (cone region) of the optical system. The sensitivity decreases away from $\epsilon = 0$. The pinhole aperture appears to have very little sensitivity outside the NA, whereas the parallelized apertures are more sensitive outside this region. The asymmetry of the slit and linear array apertures is apparent as they both have increased sensitivity towards the surface in the $\epsilon_z-\epsilon_y$ plane. The interesting V-pattern in the $\epsilon_z-\epsilon_y$ plot for the slit is due to the cross-talk between the detectors along the slit. The repetitive pattern in the parallelized pinhole apertures is a result of cross-talk between pinhole apertures. This pattern is not apparent in the slit aperture because the detectors are adjacent to

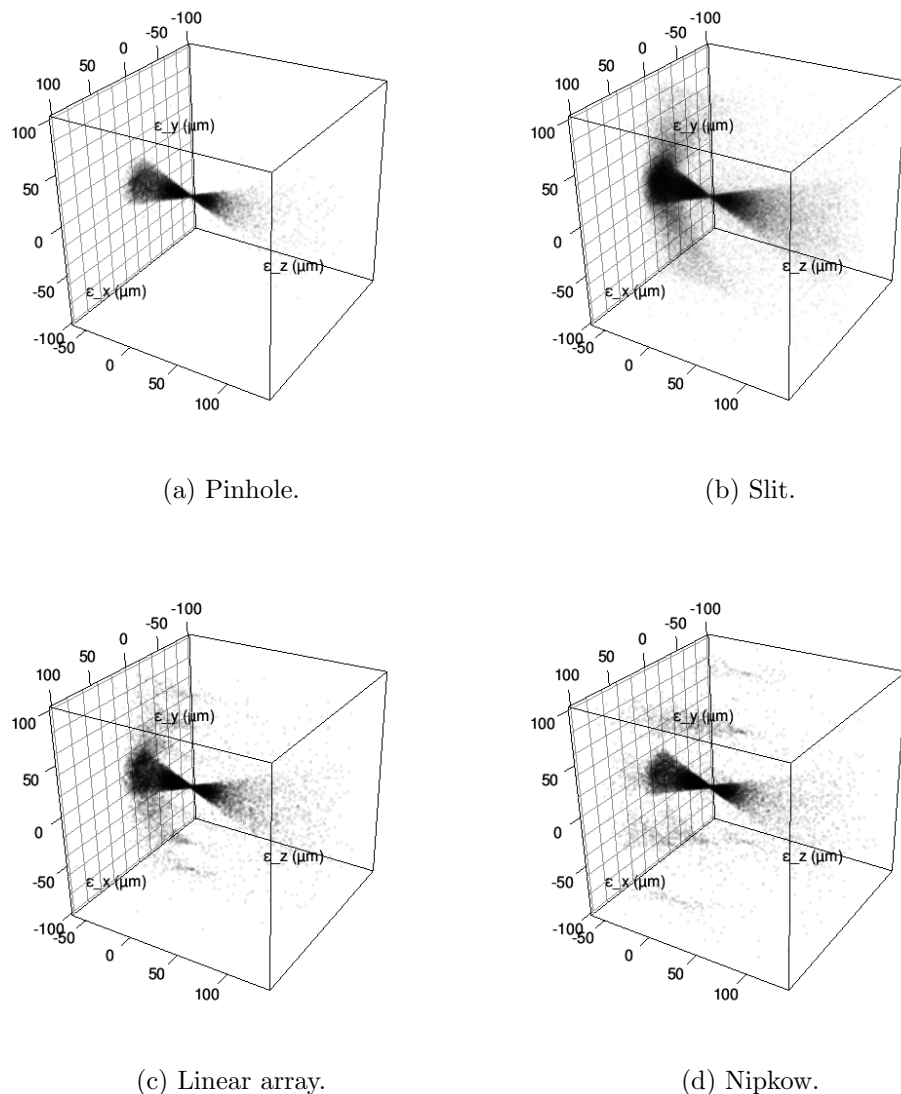


Figure 4.8: (VIDEO) Data from Fig 4.6 shown in terms of error in collected position ϵ for each aperture configuration in esophagus tissue. Video URL: <http://www.tanbakuchi.com/permanent/dissertation/Ch4V2.mov> (QuickTime 3.9 MB)

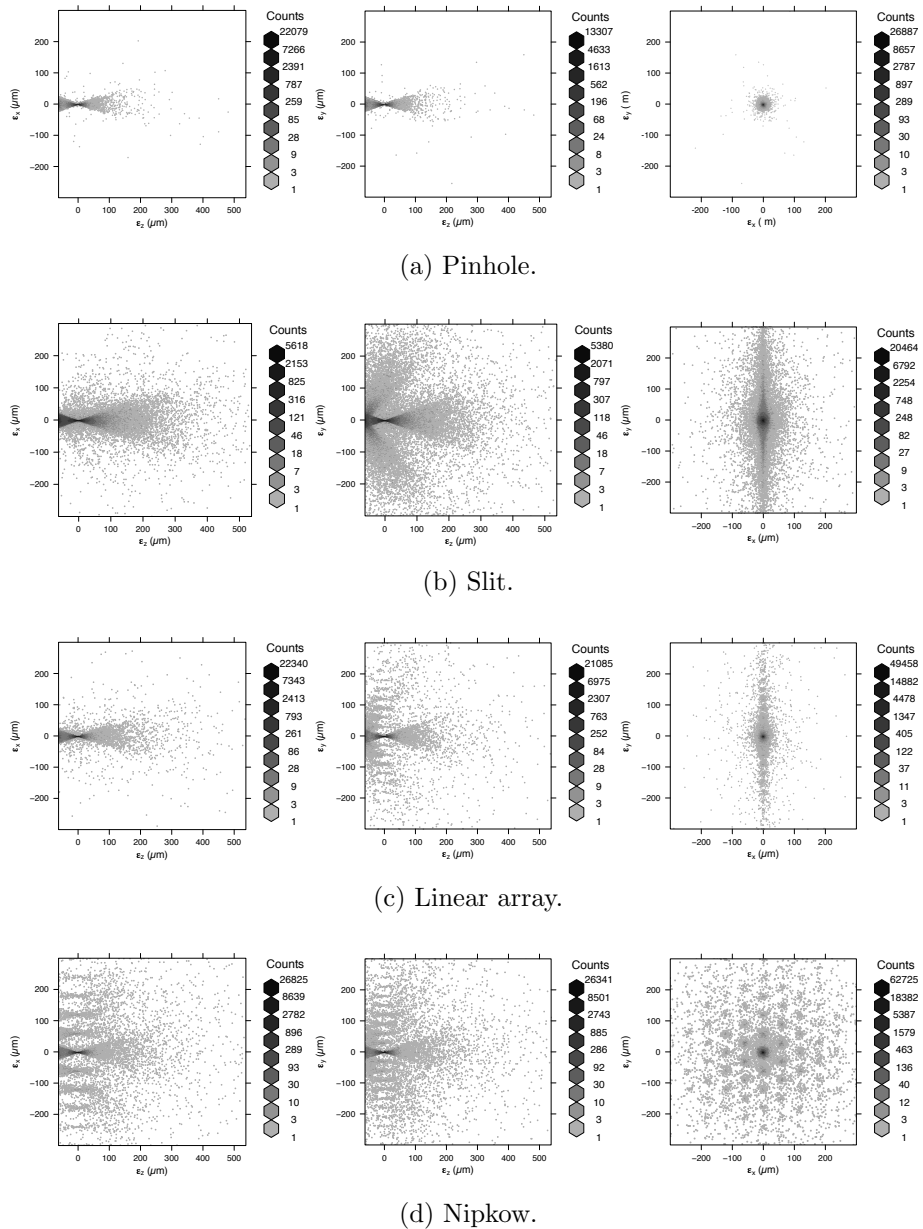


Figure 4.9: Bivariate projections of the data shown in Fig 4.8 in the axial planes $\varepsilon_z-\varepsilon_x$ (left column) and $\varepsilon_z-\varepsilon_y$ (middle column) and the lateral plane $\varepsilon_x-\varepsilon_y$ (right column) for each aperture configuration. Tissue surface is at $z = -62.5 \mu\text{m}$, focus is at $z = 0$, $d \cdot \mu_s = 0.5$.

one another.

The lateral error plots (right column) in Fig 4.9 illustrate the lateral blur induced by the tissue scattering. The elongation of the slit lateral plot in Fig 4.9(b) is due to the cross-talk between detector elements in the aperture. The repetitive clusters of signal away from $\epsilon = 0$ in the linear array Fig 4.9(c) and the Nipkow Fig 4.9(d) apertures indicates the potential for ghosting in the image.

To understand how the apertures differ in terms of their ability to reject out of focus signal, Fig 4.10 plots the axial sensitivity for each of the apertures and breaks it down into the ballistic photons (fluorescence photons that do not scatter before collection) and scattered photons. The horizontal axis is given in terms of the number of mean free paths $\epsilon_z \cdot \mu_s$ (unit-less) away from focus. The nominal focus is at $\epsilon_z \cdot \mu_s = 0$ and the tissue surface is at $\epsilon_z \cdot \mu_s = -0.5$. Each of the three curves are probability density functions describing the probability of collected photons as a function of mean free paths away from focus. For a probability density function, the area under the curve is always one and the vertical axis units are the reciprocal of the horizontal axis units.

Fig 4.10 shows that the pinhole-based apertures (pinhole, linear array, and Nipkow) have a strong peak sensitivity at focus that rapidly drops off. This represents the desired axial sensitivity in a confocal system. The pinhole-based aperture signals are composed primarily of ballistic photons near the focus. This is indicated by the overlap of the ballistic photon density plot (dashed line) with the density for all photons (solid line). There are small performance differences in the scattered photon density (dotted lines) for the pinhole-based apertures. The parallelized pinhole apertures

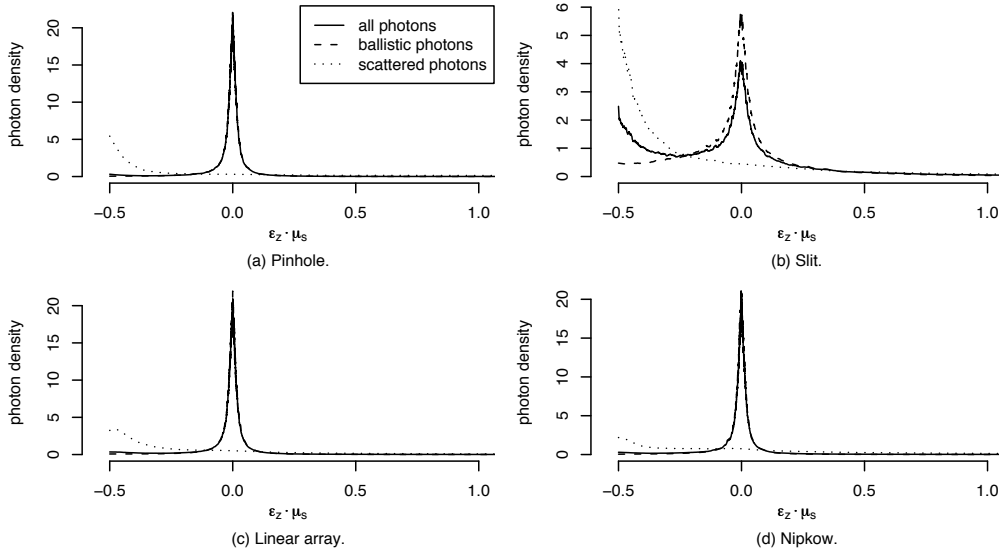


Figure 4.10: Collected photon signal density broken down into ballistic and scattered densities for each confocal aperture. Focus is at $\varepsilon_z \cdot \mu_s = 0$ and the tissue surface is at $\varepsilon_z \cdot \mu_s = -0.5$.

have more sensitivity moving away from the surface compared to the single pinhole aperture. The slit aperture Fig 4.10(b) has a significant photon density at the tissue surface due to scattered photons.

To illustrate how the confocal system's sectioning properties change with imaging depth, Fig 4.11(a) shows the ratio of the number of collected ballistic photons to the total number of collected photons as a function of imaging depth (focal position in tissue) $d \cdot \mu_s$ for each of the apertures. Fig 4.11(b) shows the standard deviation of 10 runs for each point in Fig 4.11(a) to estimate the error in the Monte Carlo model. The model errors are typically at least two orders of magnitude less than the estimated values indicating that N_c is sufficiently large to reliably estimate the relative ballistic signal. Ideally, the relative ballistic component should be equal to one. The pinhole aperture maintains more than ninety-five percent ballistic signal down to $d \cdot \mu_s = 1$. The linear array and Nipkow maintain at least ninety

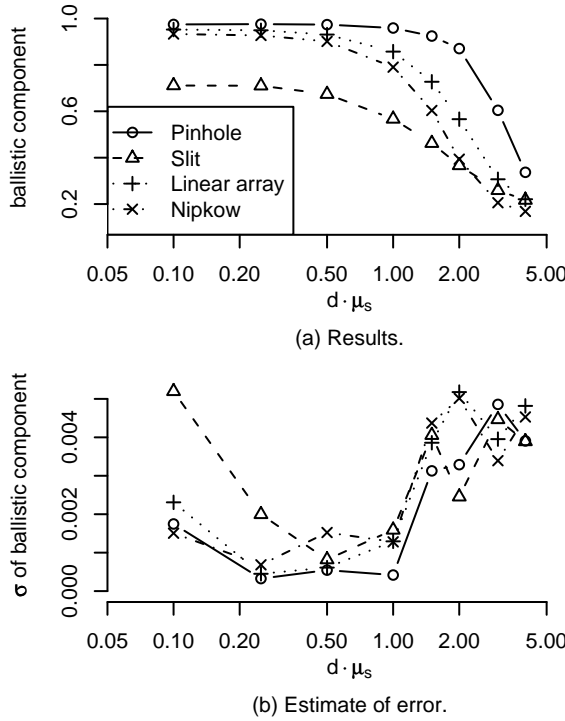


Figure 4.11: Comparison of the ratio of the number of collected ballistic photons to the total number of collected photons as a function of imaging depth $d \cdot \mu_s$ for each of the apertures is shown in (a). The standard deviation of 10 runs for each point in (a) is shown as an estimate of the Monte Carlo model error in (b).

percent ballistic signal down to $d \cdot \mu_s = 0.5$ but drop off thereafter. The drop off after $d \cdot \mu_s = 0.5$ is a result of the optimization for imaging down to $d \cdot \mu_s = 0.5$. The figure highlights that the slit aperture has the worst performance, limited to seventy-one percent at best for $d \cdot \mu_s = 0.25$.

While the relative ballistic signal helps to highlight the difference in the four aperture configurations, it fails to capture the confocal system's ability to reject defocused light that is ballistic. In general, the spread of the axial response along ε_z quantifies the axial sensitivity of the confocal system. However, a single measure of axial spread can be misleading since the axial sensitivity function is not a simple unimodal function. To provide a char-

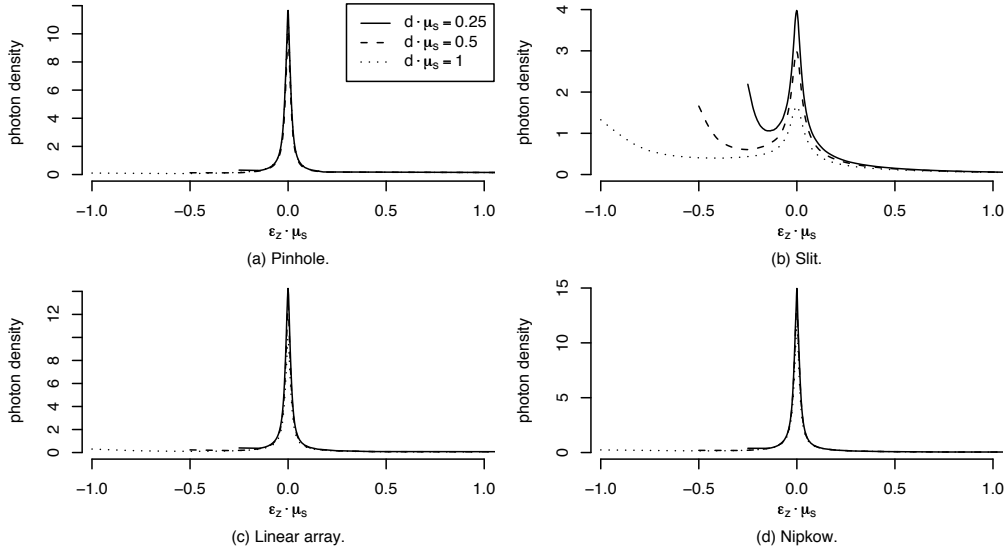


Figure 4.12: Axial density at three imaging depths for each of the aperture configurations.

acterization of axial response, we present the axial density function ε_z for a range of imaging depths, tissue properties, and fluorophore concentrations.

Fig 4.12 shows how the axial sensitivity for the four apertures varies as a function of departure from focus $\varepsilon_z \cdot \mu_s$ for three different imaging depths. The pinhole, linear array, and Nipkow apertures have nearly identical performance. The slit aperture clearly has additional sensitivity at the surface.

Quantifying the lateral and axial response in a single number such as FWHM or RMS is problematic because the distributions have long tails. FWHM does not capture the spread in the tails and RMS gives greater weight to extreme values. To quantify the spread of the lateral and axial response, we report the interquartile range (IQR), which represents the range that bounds an area of 0.5 centered about the median value. The IQR is a stable estimate of spread in the presence of extreme values.

In lens design, the lateral response of an abberated system is often relat-

ing to the diffraction limited response by comparing the RMS spot diameter to the diffraction limited Airy disk diameter. We can make a similar comparison using the lateral distribution of ε and the Airy IQR. To find the Airy IQRs, the intensity of the Airy pattern (Fraunhofer diffraction pattern)

$$I(\rho) = I_0 \left(\frac{2 J_1(k \rho \text{NA})}{k \rho \text{NA}} \right)^2$$

can be integrated to give the total power contained in a radius ρ

$$P(\rho) = P_0 [1 - J_0^2(k \rho \text{NA}) - J_1^2(k \rho \text{NA})].$$

J_0 and J_1 are the zeroth and first order Bessel functions and the $k = 2\pi/\lambda$ is the wave number. Solving for the radius that contains the middle fifty percent of the power, we find that the Airy IQR is twice this radius or $0.535\lambda/\text{NA}$. At $\lambda = 632.8$ nm and an NA of 0.5, the Airy IQR is 0.662 μm .

The diffraction limited non-scattering axial FWHM responses for pinhole and slit aperture confocal systems have been previously described.[60] For the pinhole and slit systems modeled here, the axial FWHM is 6.15 μm and 8.72 μm respectively. The central lobe of the axial response can be reasonably approximated with a gaussian profile. Since the standard deviation σ for a gaussian function in terms of the FWHM is

$$\sigma = \frac{\text{FWHM}}{\sqrt{2 \ln 2}}$$

and the IQR is $\pm 0.674 \cdot \sigma$, the diffraction limited axial IQRs for the modeled pinhole and slit systems are 3.52 μm and 4.99 μm , respectively.

Fig 4.13(a) presents lateral and axial IQR values as a function of imaging depths $d \cdot \mu_s$. To characterize the lateral distribution of ε , we compute the IQR of the signed radial response $\varepsilon_\rho = \sqrt{\varepsilon_x^2 + \varepsilon_y^2} \cdot \text{sign}(\varepsilon_x) \cdot \text{sign}(\varepsilon_y)$.

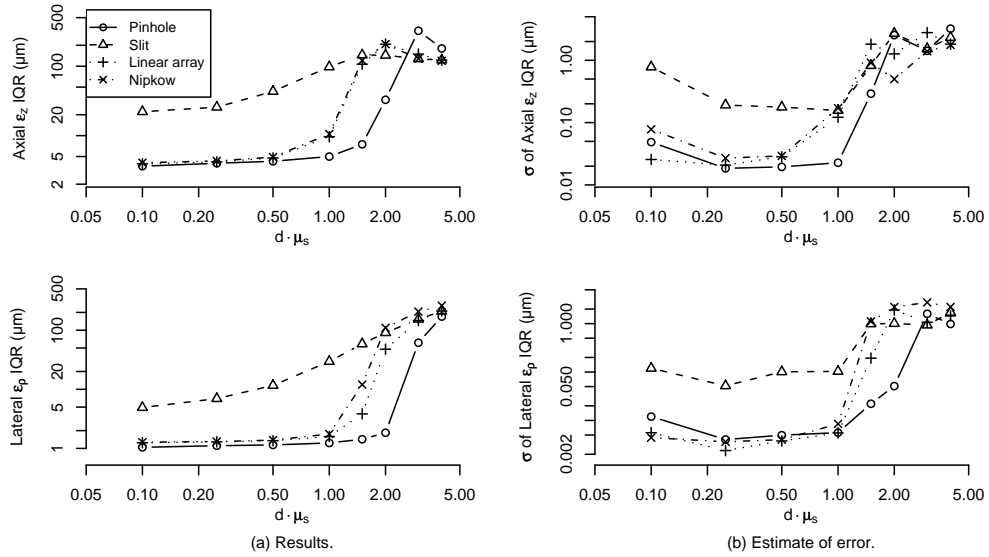


Figure 4.13: Lateral and axial IQR performance (in μm) as a function of imaging depth $d \cdot \mu_s$ for each aperture is shown in (a). The standard deviation of 10 runs for each point in (a) is shown as an estimate of the Monte Carlo model error in (b).

Since the lateral IQR values are at least twice the Airy IQR, the combination of the finite detector size and scattering effects are substantially more than the diffraction limited performance, which supports our decision to ignore diffraction effects in our model. Similarly, the axial IQR values for the pinhole and slit are also at least as large as the diffraction limited values. Fig 4.11(b) shows the standard deviation of 10 runs for each point in Fig 4.11(a) to estimate the error in the Monte Carlo model. The model errors are typically at least two orders of magnitude less than the estimated values indicating that N_c is sufficiently large to reliably estimate the IQR.

Fig 4.13 shows how the pinhole aperture has a stable axial performance of about $4 \mu\text{m}$ and lateral performance of about $1 \mu\text{m}$ down to $d \cdot \mu_s = 1$. The linear array and Nipkow aperture maintain performance comparable to the pinhole aperture down to their optimized depth $d \cdot \mu_s = 0.5$ (op-

timization discussed in section 4.3). The slit aperture has substantially degraded performance. All apertures fail for $d \cdot \mu_s > 2$ and the point of failure decreases with increasing parallelization (more pinholes).

Fig 4.13 shows that after a certain depth, the aperture performance appears to stabilize or even improve; however, this is not true. At very deep imaging depths, there is almost no signal being collected at or below the plane of focus. The resultant axial density falls off from the surface with no peak at focus causing the IQR to shift towards the surface. At these depths, the image is almost completely composed of defocused signal from near the surface.

Optimizing pinhole spacing

To maximize the speed performance of systems using parallelized apertures, the highest possible aperture density should be used. To determine the maximum possible density that can be used while still maintaining reasonable confocal performance, the maximum imaging depth $d \cdot \mu_s$ must be specified. Since the axial and lateral performance degrades as the imaging depth is increased, the pinhole spacing δ should be optimized to obtain the minimum acceptable performance at the maximum required imaging depth. To stay consistent with our previous discussion, δ is specified in terms of the aperture imaged into tissue space.

Fig 4.14(a) and Fig 4.14(b) show the axial sensitivities for three values of δ at $d \cdot \mu_s = 0.5$ and $d \cdot \mu_s = 1$ respectively. As δ increases, the performance increases. Fig 4.14(c-d) shows how the axial and lateral IQR improve asymptotically towards the limit of the single pinhole aperture as δ increases. For the target imaging depth of $d \cdot \mu_s = 0.5$, the axial and lateral

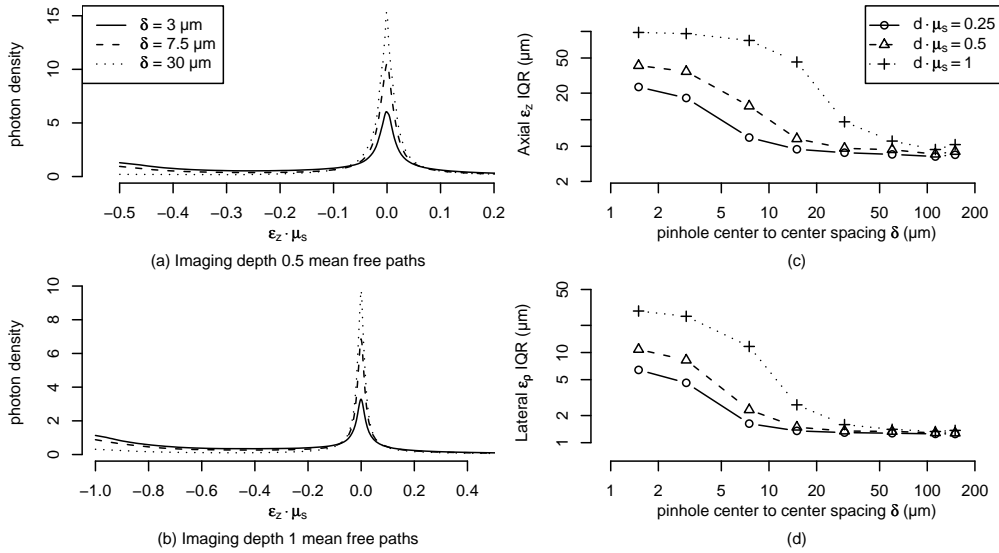


Figure 4.14: Linear array aperture pinhole spacing δ optimization. No substantial improvement for $\delta > 30 \mu\text{m}$ at target depth $d \cdot \mu_s = 0.5$.

performance does not substantially improve beyond $\delta = 30 \mu\text{m}$. Thus, for the system modeled, an optimized linear array would have fifteen pinholes spaced 30 microns in a 450 micron line.

Fig 4.15 shows the same analysis for optimizing the pinhole spacing in the Nipkow aperture. Since the Nipkow aperture has pinholes in a two dimensional arrangement, a larger δ is required to achieve the same level of performance since cross-talk can occur in two dimensions. Fig 4.15(c-d) shows that the IQR performance does not improve substantially for values of δ greater than 60 μm . Therefore, for the system modeled, a Nipkow disk with sixty pinholes spaced 60 μm in a 450 μm square area is nearly optimal.

Characterizing effects of tissue properties.

Changes in μ_s , μ_a , and g can have substantial effects on the axial and lateral performance. Since we present our results in terms of $\varepsilon_z \cdot \mu_s$ and $d \cdot \mu_s$ they

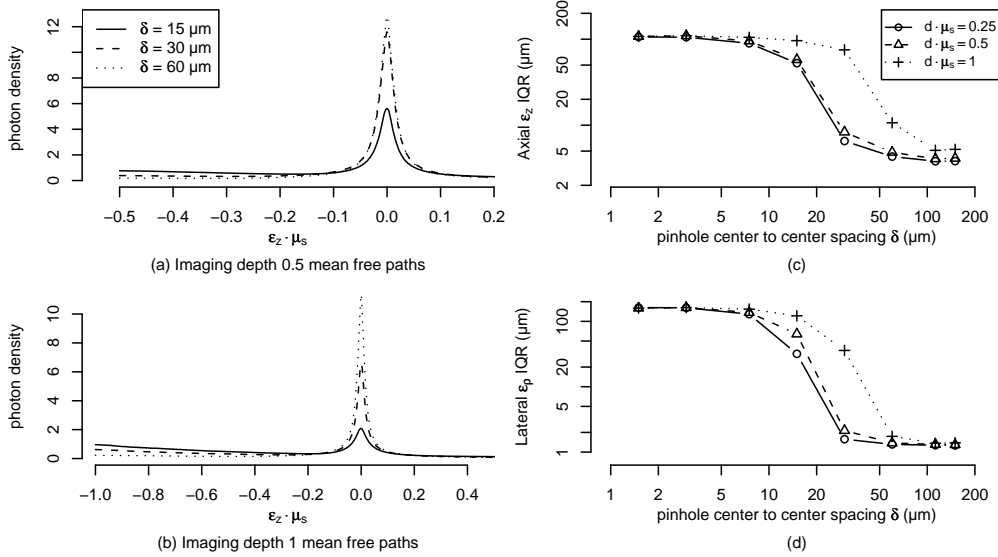


Figure 4.15: Nipkow aperture pinhole spacing δ optimization. No substantial improvement for $\delta > 60 \mu\text{m}$ at target depth $d \cdot \mu_s = 0.5$.

are inherently generalized for μ_s . To determine how μ_s , μ_a , and g effect the system performance, we analyzed a range μ_a/μ_s and g values that might be encountered when imaging tissues. We only present the effects for the pinhole and slit apertures since these two represent the extreme cases.

Soft tissues generally have $\mu_a/\mu_s < 1$, therefore we analyzed this ratio in the range 0 to 1.[87] Fig 4.16 shows how the axial sensitivity and the lateral and axial IQR are effected by changing μ_a/μ_s . The effect on the axial sensitivity is subtle. As μ_a/μ_s increases, the focus peak slightly increase because the increased absorption causes a decrease in the tails for $\varepsilon_z \cdot \mu_s > 0$. There is also a small increase in signal towards the tissue surface, although the effect is only appreciable in the slit aperture since it is more sensitive to signal from the surface. The relatively flat IQR lines at different imaging depths indicate that both the pinhole aperture and the slit aperture are resistant to the effects of changing μ_a/μ_s .

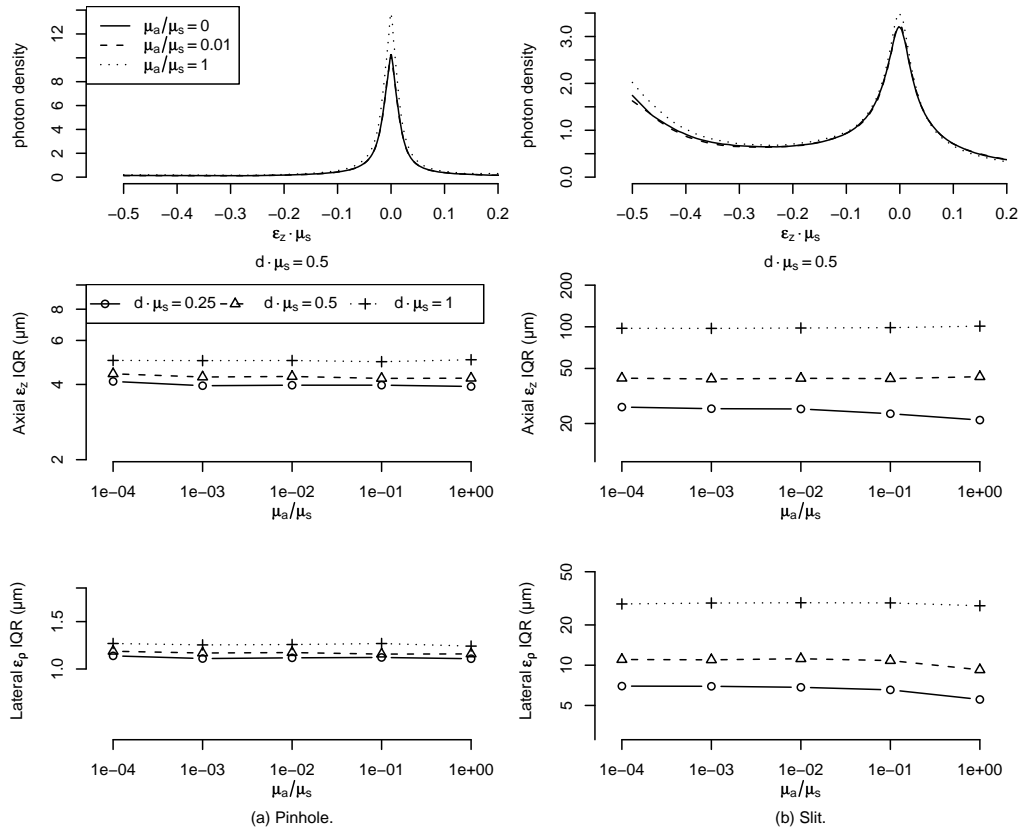


Figure 4.16: Effect on the lateral and axial performance with changing μ_a for the pinhole and slit apertures.

We studied g in the range of 0.8 to 0.95 since this is the typical range for soft tissues.[87]. Fig 4.17 shows how the axial sensitivity and the lateral and axial IQR are affected by changing g . As was the case with variations in μ_a/μ_s , the results show that the axial sensitivity density is not very sensitive to changes in g .

Characterizing the effect of fluorophore concentration.

We also studied the effect of changing μ_f/μ_s in the range of weak fluorophore concentration ($\mu_f/\mu_s = 0.1$) to a very strong concentration ($\mu_f/\mu_s = 2$). Fig 4.18 shows that there are changes in the axial sensitivity and the lateral

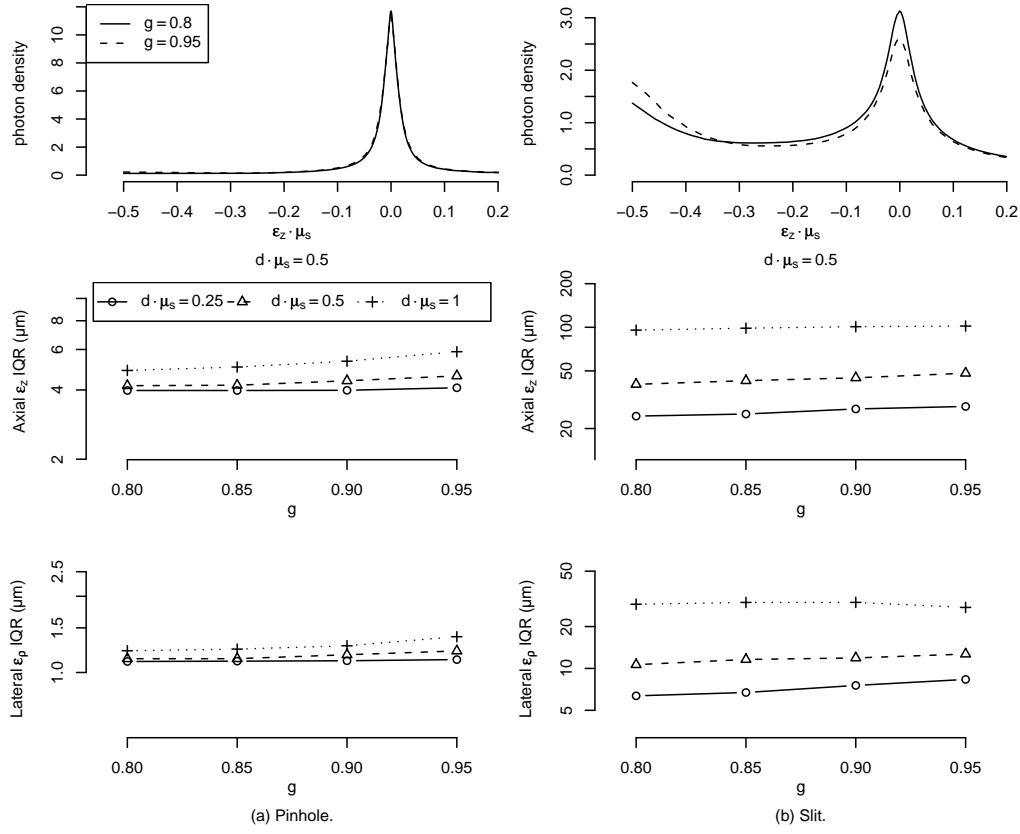


Figure 4.17: Effect on the lateral and axial performance with changing g for the pinhole and slit apertures.

and axial IQR values for high μ_f/μ_s . Increasing μ_f/μ_s causes the surface sensitivity of the slit to increase. The IQR plots indicate that the pinhole performance is stable down to $d \cdot \mu_s = 0.5$, but beyond this depth increasing μ_f/μ_s degrades the performance.

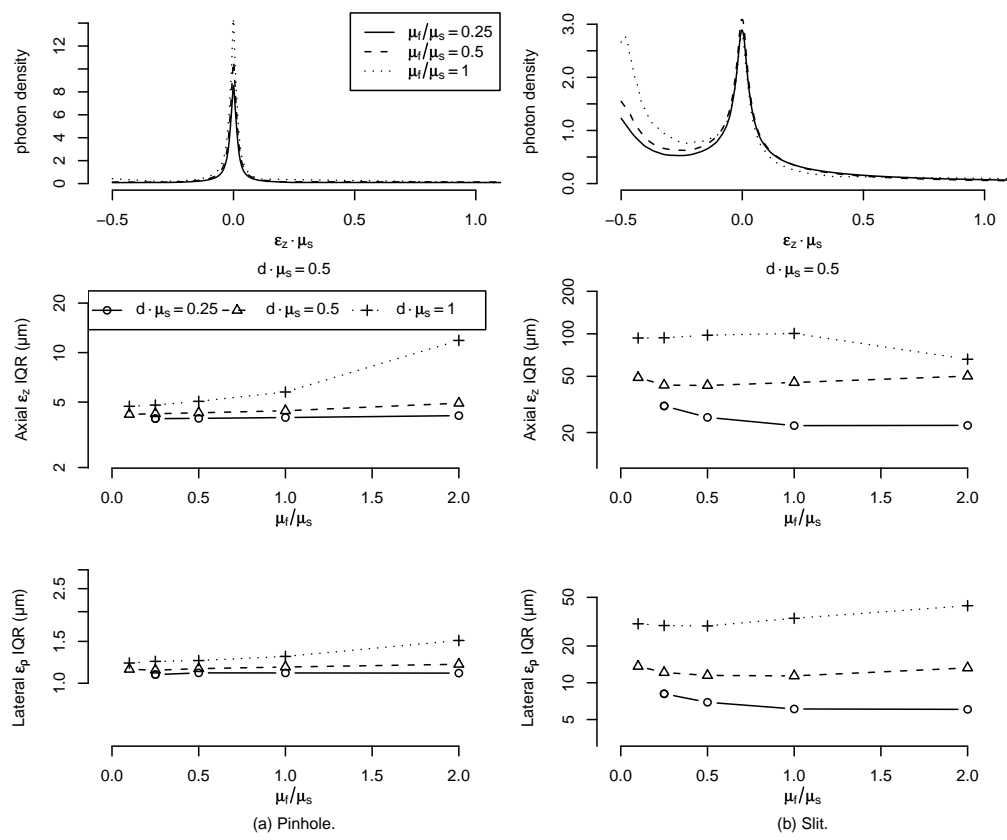


Figure 4.18: Effect on the lateral and axial performance with changing μ_f for the pinhole and slit apertures.

Chapter 5

New miniature objective lens

IN THE FOLLOWING SECTIONS WE DESCRIBE a new miniature lens designed to increase the performance of future confocal microlaparoscopes and microendoscopes. To reduce tissue abrasion from the dye delivery port and allow dye to be delivered closer to the imaging field, the new lens integrates the dye delivery channel. To improve imaging performance, the new lens doubles the wavelength range over which the system can operate, increases the field of view, increases the resolution, and increases the tissue space NA while decreasing the number of optical elements as compared to the existing miniature lens.

5.1 Existing miniature lens

The confocal microlaparoscope described in Chapter 2 uses a miniature objective lens to image the tissue focal plane onto a fiber bundle. The miniature objective lens used in the microlaparoscope (shown in Fig 5.1) was designed by Rouse[6] in 2004 for use with a previous generation laboratory

microendoscope. The results in Chapter 3 show that the lens performs exceptionally well in the microlaparoscope.

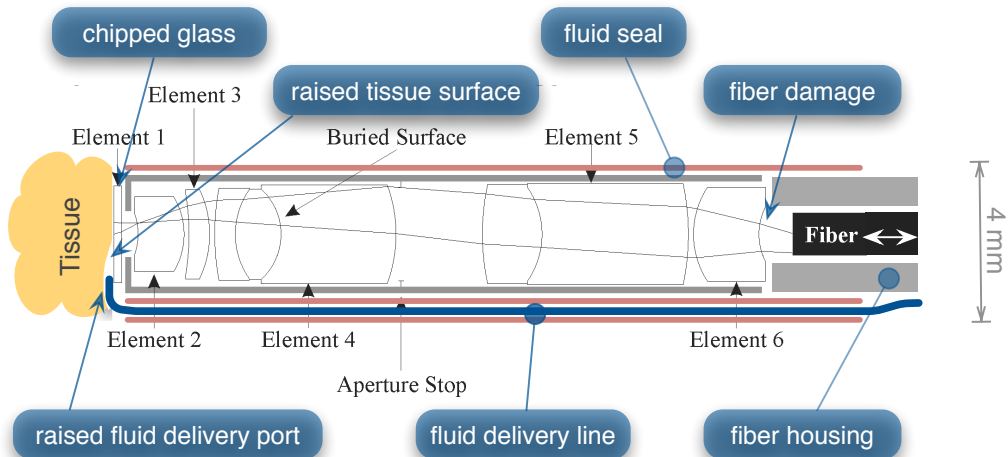


Figure 5.1: Existing lens (Rouse 2004) shown with modifications added for use on the confocal microlaparoscope.

During the clinical trials, four problems were observed concerning the miniature objective lens. First, the front element, a microscope cover slip, was designed to be an inexpensive element that could easily be replaced if scratched during use. In practice, the front element was never scratched within the clear aperture but the exposed edges did frequently chip. In addition, the front element was glued to the face of the lens housing and there was concern that during use the element might detach, which poses a safety issue. In addition, the air glass interface of the front element was difficult to have antireflection coated. Moreover, the front element has no power, but contributes aberrations to the system, which must be corrected by other elements. Second, the focus mechanism does not have a mechanical stop to prevent the fiber bundle from hitting the rear element. During focusing, the fiber bundle was inadvertently rammed into the rear element

causing damage. Third, the lens housing was not designed to be sealed against bodily fluids, therefore an additional housing had to be placed over the lens causing the outer diameter to increase. Finally, because the dye delivery channel was built onto the outside of the lens and curved around the front element, it was difficult to deliver fluid to the edge of the field without lifting the tissue and potentially causing abrasion of the epithelium.

5.2 New miniature lens

A completely new lens was designed to solve the observed problems and substantially increase the system's imaging performance. Fig 5.2 shows the new design. The front element is thick, mounted inside the housing, and the front face is flush with the outside housing. This alleviates the safety issues with edge cracking and detachment. Additionally, the front element has power contributing to the optical performance. The front surface that contacts the tissue has a slight positive curvature to help the tissue conform to the focal plane. The new design also integrates a dye delivery channel into the housing. This allows larger diameter elements to be used while maintaining the same overall outer diameter as compared to the previous lens. The front element is tapered so that the dye channel exit port is closer to the imaging field. Moreover, the integrated dye channel allows the exit port to be flush with the front of the lens rather than sticking out. On the rear end of the lens, the fiber bundle is mounted in a housing that has a flange to prevent damage of the rear lens surface when focusing.

Table 5.1 compares the existing lens properties with the new lens properties. The basic goals for the new design were to increase the chromatic

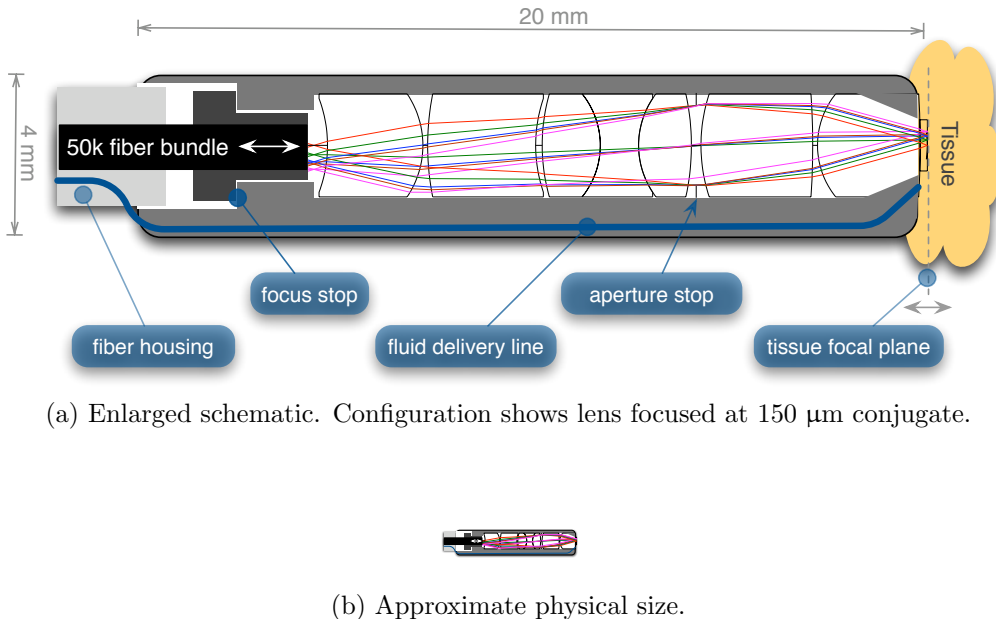


Figure 5.2: New lens design. Lens elements are to scale, housing is only approximately to scale.

correction out to 830 nm, increase the tissue space NA and increase the magnification to 1.75 while maintaining a similar packaged size. The original lens has nine optical elements (eight with power) and twelve air-glass interfaces. In the new design, the number of optical elements was reduced to seven and the number of air glass-interfaces was reduced to nine. This simplification will decrease manufacturing costs, reduce the amount of background light due to reflections, and improve the overall performance since fewer lenses need to be aligned. By increasing the chromatic correction to 830 nm, the spectral bandwidth has been doubled compared to the previous lens. This allows the use of longer excitation wavelengths and opens up a whole new range of potential contrast agents. Since tissue scattering decreases at longer wavelengths this will enable imaging deeper in tissue.

To further enhance the optical sectioning properties of the confocal sys-

Table 5.1: New and existing lens properties.

	EXISTING LENS (Rouse 2004)	NEW LENS (Tanbakuchi 2008)
number of elements	9	7
number of glass-air interfaces	12	9
length	13 mm	15 mm
length with focus housing	20 mm	20 mm
clear aperture \varnothing	2 mm	2 mm
housing with dye channel \varnothing	4 mm	4 mm
chromatic correction	486 – 656 nm	486 – 830 nm
imaging depth range	0 – 200 μm	0 – 150 μm
NA at fiber	0.29	0.29
NA in tissue	0.46	0.51
magnification	1.6	1.75
field of view	450 μm	630 μm
fiber bundle elements	30,000	50,000
fiber spacing in tissue	1.88 μm	1.5 μm
telecentric at fiber	COMPLETELY	COMPLETELY
telecentric at tissue	COMPLETELY	NEARLY

tem, the NA was increased from 0.46 to 0.51. The magnification was increased to 1.75. Although increasing the system's magnification improves visualization of cellular features, the field of view decreases, but maximizing the field of view is also important. To increase the field of view, the new lens was designed to use a larger fifty-thousand element fiber bundle. This results in a larger 630 μm field of view while still increasing the resolution in tissue space. Although the previous lens was designed to image down to 200 μm , the results in Chapter 4 indicate that imaging performance is severely degraded at this depth. Therefore, the new lens was only designed to image down to 150 μm .

An initial design was created containing two positive lenses near the tissue. The front element had its near planar side in contact with the tissue. A

triplet was placed to the left of the two front elements in a collimated space. On the rear side of the lens, two additional positive elements were added to focus the beam onto the fiber. The initial configuration was based on of the principles used in high NA oil immersion objective lenses. These lenses employ a few positive elements near the tissue to minimize the accumulated spherical aberration by slowly bending the strongly diverging beams into a collimated space. In the collimated space, doublets and triplets are used to correct the chromatic aberrations and balance the odd aberrations. Unlike microscope objectives, the new lens must also refocus the beam onto the fiber bundle requiring the additional positive elements.

To allow the new lens to be used in a flexible confocal microgastroscope, the rigid length was limited to 20 mm. With the length and diameter constrained, the most challenging aberrations to correct were spherical and chromatic. With a high NA in tissue space and a maximum depth of 150 μm , the cone size at the entrance of the front lens is already large compared to the maximum possible lens diameter. This requires rapid bending of the beam to prevent vignetting—inducing significant spherical aberration. Although more elements increase the degrees of freedom, there is a finite limit to the number of elements that can be added in a 20 mm space and more elements tend to decrease the toleranced performance. Significant time was spent selecting the appropriate glass combination to balance the chromatic and spherical aberrations while limiting the astigmatism across the field. During the optimization process, elements were added and removed and their bending factors adjusted. The process was repeated until the the lens was sufficiently insensitive to manufacturing tolerances.

Fig 5.3 shows the optical path difference (OPD) plot for the new lens at

15 μm depth. The lens is corrected to approximately $\pm\lambda/4$ across the field indicating near diffraction-limited performance. The primary aberrations present are spherochromatism and astigmatism with some minor blur due to Petzval field curvature at the fiber plane. At the 150 μm depth the lens is dominated by astigmatism. To efficiently control the aberrations while maintaining the tight constraints on the maximum clear apertures, vignetting was employed. At the full field position, the tangential rays are vignetted by approximately twenty-five percent. The tissue plane is slightly curved for a flat field at the fiber plane. Fig 5.4 shows that the distortion is well controlled, and less than 2.5 percent at the 15 μm depth. Distortion decreases with increasing depth.

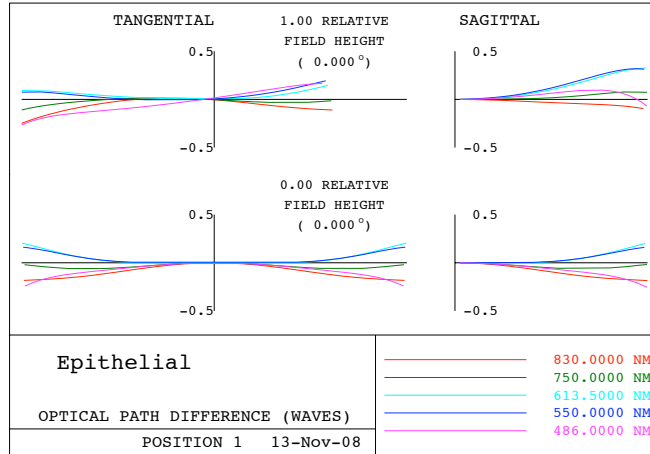


Figure 5.3: Lens OPD at the 15 μm conjugate for the full field position (top) and central field (bottom).

The design goal was a fifty percent MTF as-built performance at the target frequency for each conjugate depth. The lens was optimized to have near diffraction-limited performance when imaging near the tissue surface at a nominal depth of 15 μm . The new design was not optimized to diffraction-limited performance below the nominal depth. Since the results in Chap-

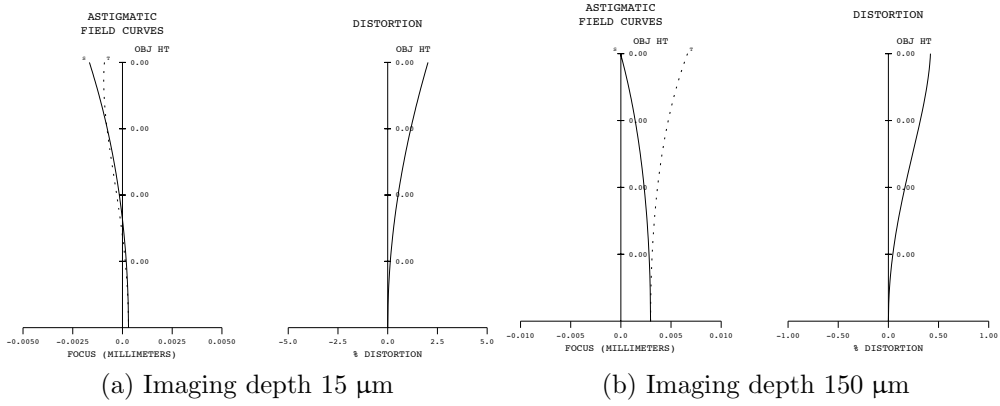


Figure 5.4: Field curvature and astigmatism for the extreme conjugates.

ter 4 show that the system resolution is limited by scattering and severely degrades with depth, the lens was optimized to the lower performance limits for a slit-scan system. The individual fiber spacing in the fiber bundle acts as the Nyquist sampling frequency. The Nyquist frequency f_N in tissue is therefore

$$f_N = \frac{1}{\delta} \cdot \frac{1}{M},$$

where δ is the fiber spacing and M is the lens magnification. Since the fibers are spaced by $3 - 4 \mu\text{m}$ and the lens has a magnification of two, f_N is maximally 583 cycles/mm. The highest unaliased tissue frequency that could be recorded by the fiber bundle is 292 cycles/mm. Since a slit-scan system's lateral resolution performance is degraded slightly from the diffraction-limit at the surface, the target frequency for epithelial imaging ($15 \mu\text{m}$ conjugate) was reduced to 272 cycles/mm. This frequency is substantially greater than the actual scattering limited resolution obtained by a slit-scan system, which will allow the lens to work with future optimized parallelized confocal apertures. The $50 \mu\text{m}$ mid conjugate target frequency was set to 136 cycles/mm, half the epithelial frequency. The deepest con-

jugate ($150 \mu\text{m}$) target frequency was set to 68 cycles/mm, half the mid conjugate. Fig 5.5 shows the optimized MTF performance at the three conjugates. The lens design was analyzed and it was determined that the fifty percent MTF goal would be met for the target frequencies. To simplify manufacturing, each lens surface was fitted to an existing test plate owned by Liebmann Optical Company (Easthampton, Massachusetts), our selected manufacturer.

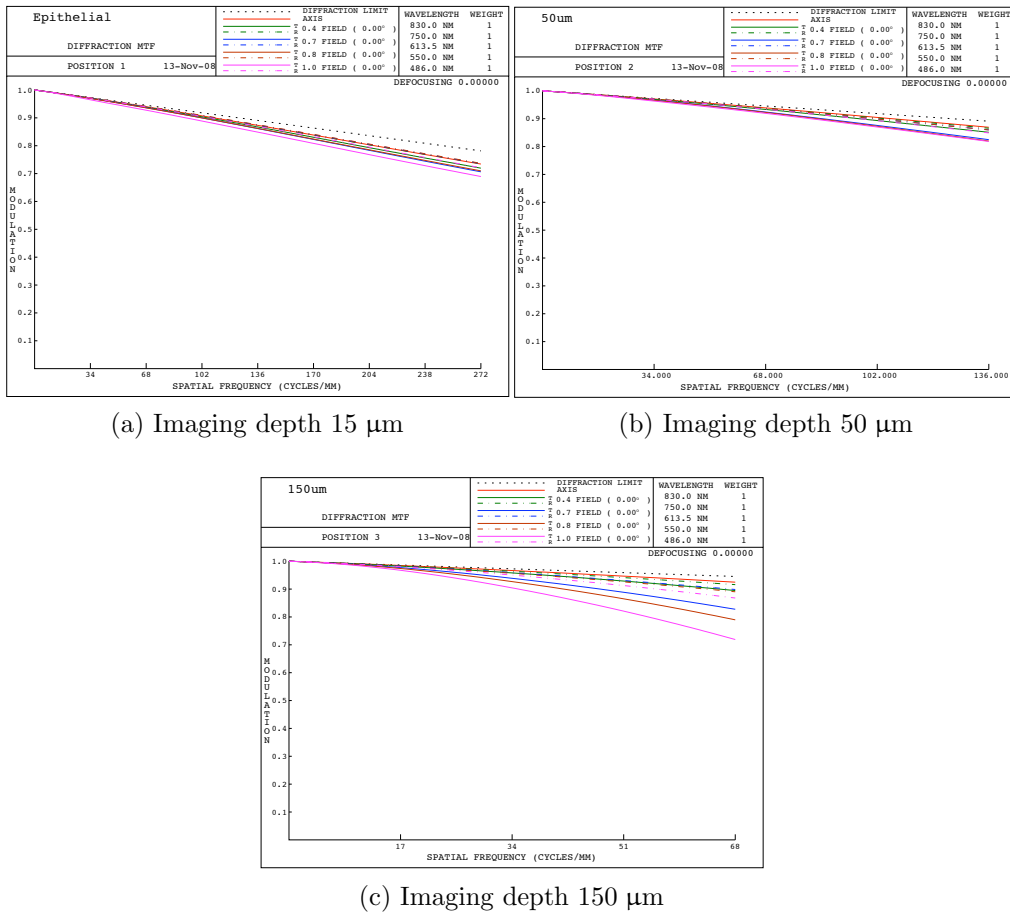


Figure 5.5: MTF of the new lens design at the three primary conjugates.

The final lens prescription is shown in Table 5.2. The majority of the development work involved creating a lens that could meet the design goals

Table 5.2: Lens prescription

	Surf.	Rad. (mm)	Thick. (mm)	Material	CA ϕ (mm)
Fiber bundle	OBJ	∞			1.025
Focus space	1		0.415 – 0.100		2.00
	2		0.166		2.00
Meniscus A	3	-2.93	1.984	SF4	2.00
	4	-2.00	0.100		2.00
Meniscus B	5	5.80	2.417	SF4	2.00
	6	3.18	0.126		2.00
Triplet	7	4.12	1.124	NBF2	2.00
	8	-1.78	0.800	SF4	2.00
	9	1.85	1.076	NLAK22	2.00
	10	-5.26	0.100		2.00
Aperture	STO		0.100		1.68
Front elem. B	12	3.60	2.308	NLASF31A	2.00
	13	-16.63	0.100		2.00
Front elem. A	14	1.78	2.170	NLASF31A	2.00
Tissue	15	-20.09	0.015 – 0.150	WATER	1.25
	IMG	-1.76 – -2.04		WATER	0.63

in the final built system after tolerancing. The tolerance analysis indicates that there is a high probability that the final assembled lens will meet the desired fifty percent MTF at the target frequencies. Fig 5.6 shows that the most sensitive conjugate (at the 15 μm depth) has a more than ninety percent chance that the mid and central fields will achieve the design criteria. The edge of the field has a seventy percent chance of meeting the criteria. Precision tolerances will be required for the radii of surfaces 4-7, 9, 10, 12-14, and the thicknesses after surfaces 6, 13-14 (See Appendix B.1 for complete tolerance analysis). Elements 2, 3, 6, 7, and 8 are the most sensitive to wedge. Elements 2 and 6 are the most sensitive to tilt.

Fig 5.7 highlights where the precision tolerances are required on the lens

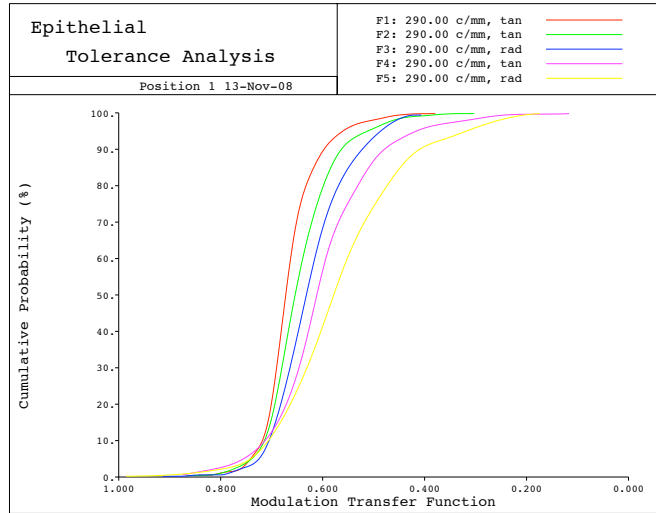


Figure 5.6: Tolerance analysis of assembled design at the 15 μm conjugate.

layout. The figure also illustrates the four glasses used in the design. All the glasses exhibit low fluorescence. Since the front element comes into contact with the tissue, it is lead and arsenic free and has good resistance to scratching and environmental staining. The rear element was also chosen to have good resistance to scratching and environmental staining since its left face (near the fiber) has more environmental exposure.

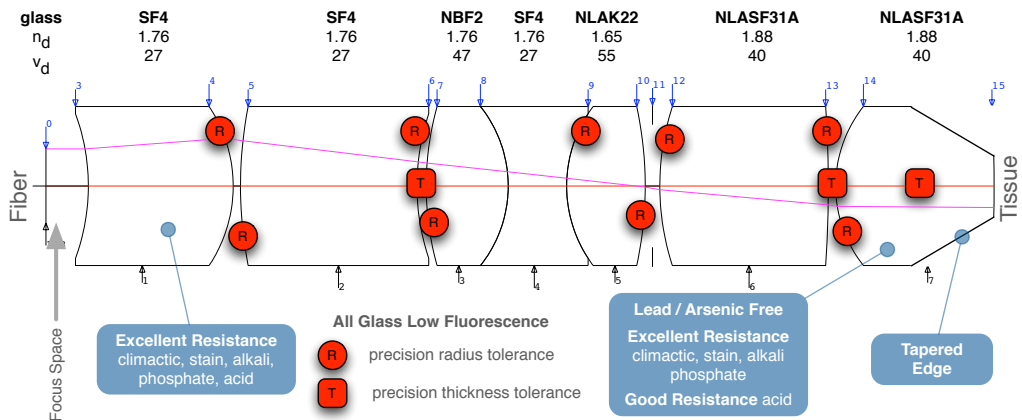


Figure 5.7: Lens tolerances and specifications.

All air-glass interfaces will be anti-reflection coated. Surfaces 3-7 and

10 will be coated with a multi-layer broad band anti-reflection coating to reduce surface reflections to less than half a percent. The high index difference interfaces at surfaces 12-14 can use a more economical single-layer MgF₂ coating to reduce the surface reflections to less than one percent. For safety reasons, the front surface will not be coated because most coatings use toxic materials and the coating could wear off during use. In addition to blackening the inside of the lens housing, the edges of the lenses will be blackened to reduce scattered light.

Chapter 6

Bare fiber probes

ALTHOUGH THE CONFOCAL MICROLAPAROSCOPE described in Chapter 2 represents the smallest diameter clinical confocal laparoscope presented to this date, the device is too large for some applications. To enable clinical imaging in small lumens such as the pancreatic duct and the fallopian tubes a 1 mm flexible bare fiber probe was developed. The probe is suitable for small lumen imaging in humans and animals. Unlike the microlaparoscope, a bare fiber probe is a fixed imaging device. It can only image the surface of the tissue that it is in contact with. Since the bare fiber has no lens system, the focus cannot be controlled and the axial sectioning properties are defined by the fiber NA and the tissue properties. Although this may seem like a significant limitation, in our experience, the tissue surface is the most important imaging plane for determining pathology.

It is possible to use a bare fiber bundle in contact with tissue and acquire confocal images *in vivo*. The face of the fiber bundle must be polished smooth and the tissue must make uniform contact with the epithelium to form a good image. Bare fiber bundle confocal probes were previously

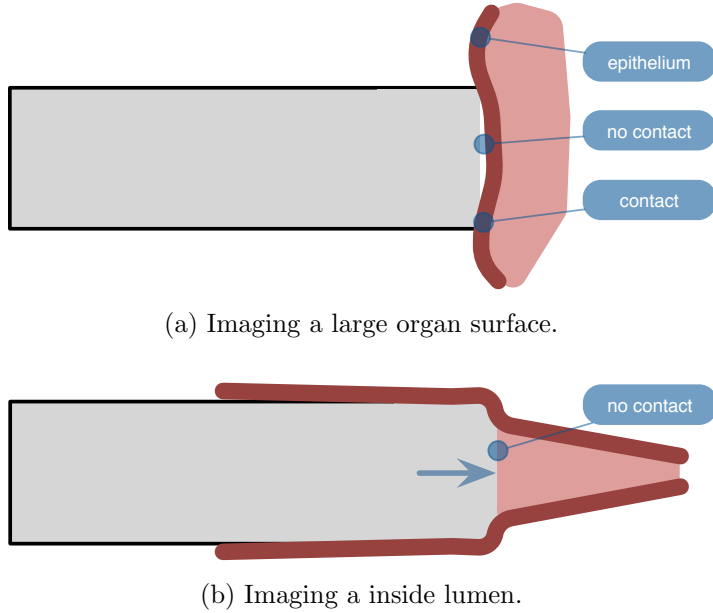


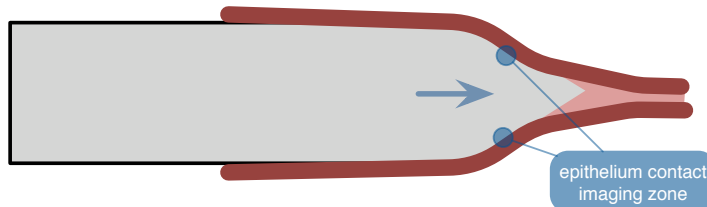
Figure 6.1: Illustration showing how a flat tip bare fiber has problems making uniform contact with the epithelium when imaging large organs (a) and inside lumens (b).

investigated by our group for brain imaging. Commercial bare fiber probes are now available[88] for laboratory and animal imaging applications.

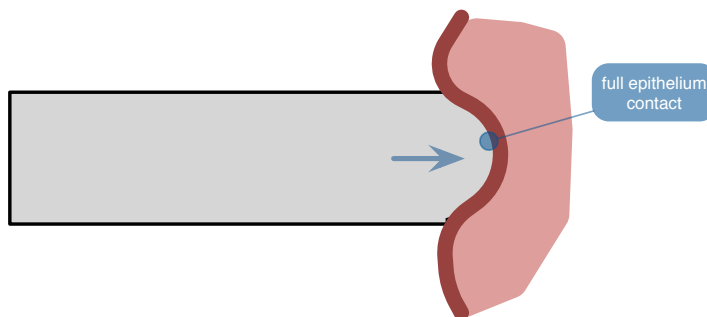
A limitation of the existing probes is their flat tipped design. If too much pressure is applied when pressing the tip against the epithelium of a large organ, the organ will deflect causing the center of the probe to lose contact with the epithelium as illustrated in Fig 6.1(a). Moreover, a flat probe is not well suited for imaging inside small lumens because the probe makes almost no contact with the epithelium (shown in Fig 6.1(b)).

6.1 Probe designs

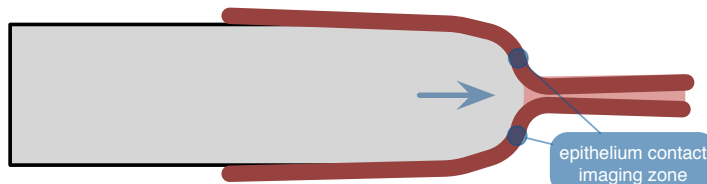
Since the image quality obtained with bare fiber probes is directly dependent on the quality of the fiber face's contact with the tissue, a contoured



(a) Cone tip imaging epithelium inside a lumen.



(b) Round tip imaging epithelium on a large organ.



(c) Round tip imaging epithelium inside a lumen.

Figure 6.2: Illustration showing how a contoured fiber tip can increase the amount of epithelium in contact with the probe.

tip design was conceived. For imaging inside a lumen, a cone tip was initially developed. A hemisphere tip was also created for lumen imaging and for imaging large organ surfaces. Fig 6.2 illustrates how the contoured tips improve tissue contact compared to the flat tipped design shown in Fig 6.1. The cone tip is capable of making a ring of constant contact against a lumen that contracts around the probe. A hemisphere tip works similarly to the cone in a lumen but has the added advantage that it can image large organ surfaces and provide more uniform contact as illustrated in Fig 6.2(b).

All three probe designs (flat, cone, and hemisphere tips) were developed.

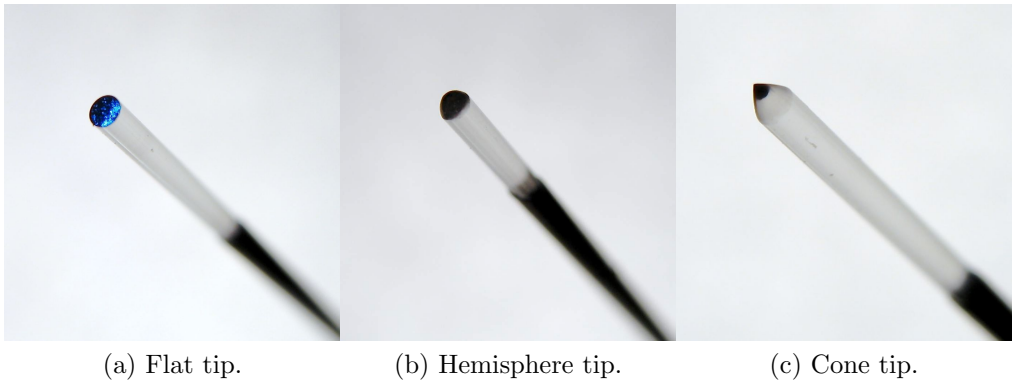


Figure 6.3: Three different bare fiber probes developed and tested.

Appendix D describes how the flat fiber tips were contoured. Fig 6.3 shows the three bare fiber probes that were tested. The probes were made using a 1 mm outer diameter fiber bundle containing thirty-thousand elements. The active image area in the fiber was 730 μm . The probes were connected to the same slit scan confocal optical scan unit described in Chapter 2. An additional hemisphere tipped probe was made using a 2 mm one-hundred thousand element fiber bundle.

6.2 Results

The Monte Carlo model described in Chapter 4 was used to characterize the imaging performance of the bare fiber probes in contact with tissue. The model was run using the parameters for the slit system, the thirty-thousand element fiber bundle's 3 μm fiber spacing and 2 μm fiber core sizes, and the fiber's NA of 0.29. The same esophagus tissue parameters presented Chapter 4 were used (see page 93).

In many cases fluorescent contrast agents may be applied to the surface of the tissue. Therefore, in addition to modeling uniform fluorophore con-

centration in the tissue, topical application of fluorophore on the tissue's surface was also modeled. For the uniform fluorophore case, the fluorophore coefficient was $\mu_f = 0.5\mu_s$. For the topical fluorophore case, the fluorophore coefficient was maximally $\mu_f = 5\mu_s$ at the tissue surface and decayed axially using a gaussian function with μ_f reaching half of its surface value at a depth of 25 μm .

The results of the Monte Carlo simulations are shown in Fig 6.4. The figure shows the lateral signal distribution for r_s (top row) and the lateral (middle row) and axial (bottom row) error distribution of $\vec{\varepsilon}$ for uniform fluorophore (a) (left column) and topical fluorophore (b) (right column). The axial response with the uniform fluorophore is much worse than the topical fluorophore. The axial IQR values for the uniform and topical fluorophore cases were 35.2 μm and 7.92 μm respectively. The lateral IQR values for the uniform and topical fluorophore cases were 3.70 μm and 1.74 μm respectively. Fig 6.5 compares the axial photon density for the two cases. The plot shows more surface sensitivity for the topical fluorophore whereas the uniform fluorophore has an extremely long tail of sensitivity deep into the tissue.

The hemisphere tipped probe was tested first on excised human esophagus tissue. Topical fluorophore application was used since the Monte Carlo results indicated that this fluorophore configuration provides the best axial and lateral performance. Results from normal squamous epithelium are shown in Fig 6.6(a) and results from Barrett's esophagus are shown in Fig 6.6(b). In comparison to the images of esophagus tissue obtained with the confocal microlaparoscope shown in Fig 2.17 (on page 56), the bare fiber images depict similar cellular structures. The dispersed nuclei

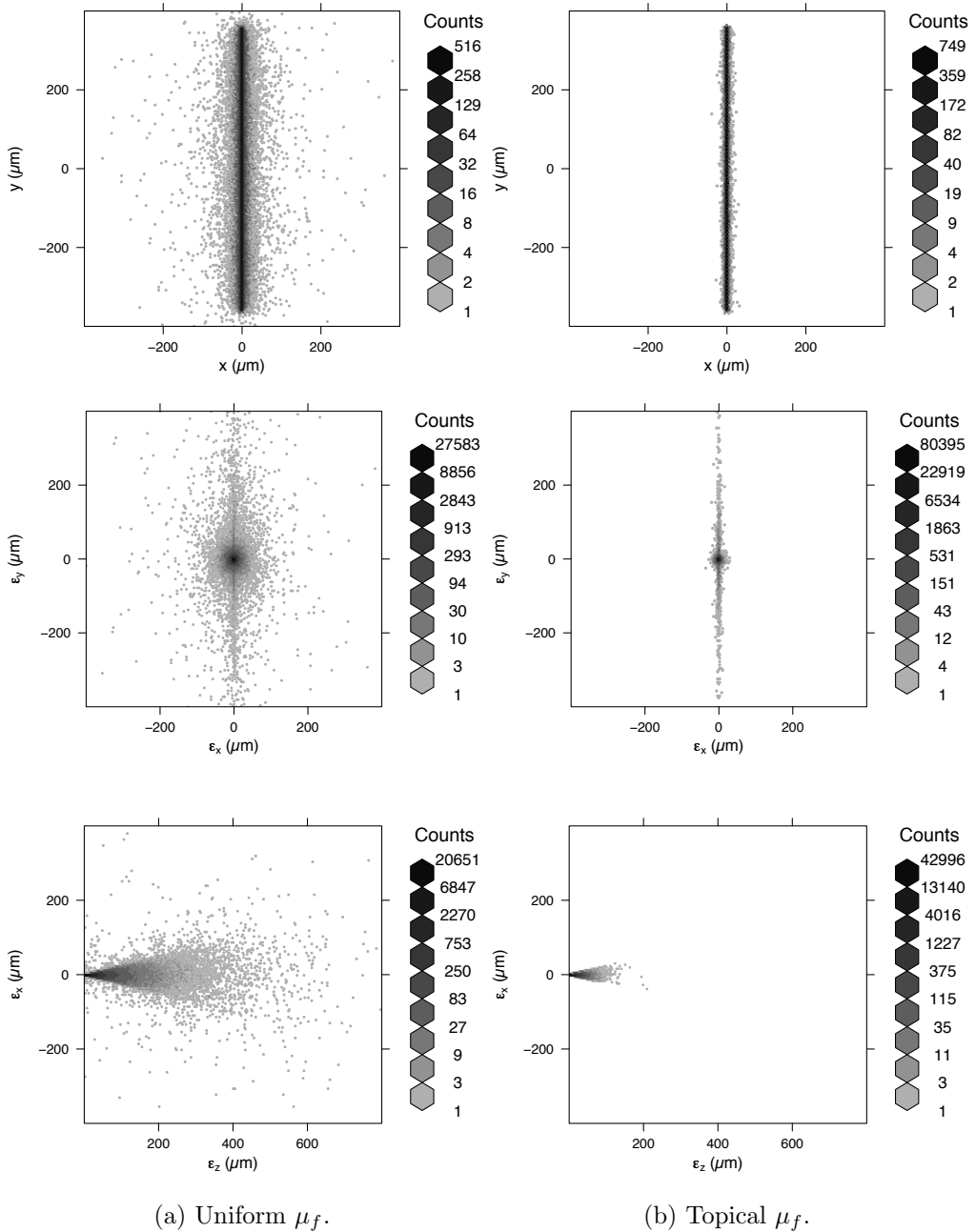


Figure 6.4: Lateral signal distribution for r_s (top row) and lateral (middle row) and axial (bottom row) error distribution of $\vec{\varepsilon}$ for uniform fluorophore (a) and topical fluorophore (b) with μ_f reaching half of its surface value at a depth of 25 μm .

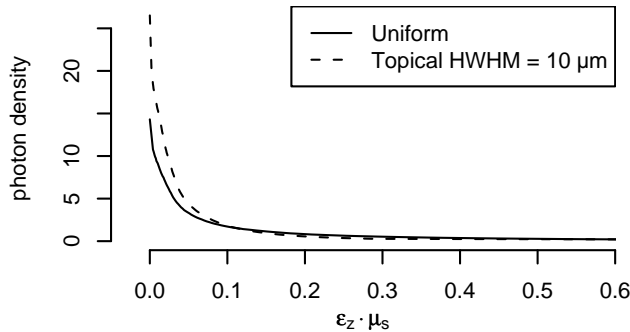


Figure 6.5: Axial photon density for uniform fluorophore and topical fluorophore with HWHM 25 μm .

in the normal squamous epithelium are visible and the crypts in the Barrett's tissue are also evident. The reduction in contrast as compared to the microlaparoscope can be attributed to the reduction in optical sectioning resulting in more background signal being collected from below the tissue's surface.

The most promising use of the contoured tipped bare fiber probes is for small lumen imaging. The cone tip and hemisphere tipped probes were tested *in vivo* for imaging in mice. During testing, it was discovered that the hemisphere tips could maintain much better contact with the lumen's surface and were less likely to cause trauma. The best imaging was obtained during entry into the lumen rather than exiting from the lumen. During entry the lumen is compressed against the hemispherical face. During exit, the lumen pulls away from the face and imaging is difficult.

Fig 6.7 shows images and Fig 6.8 shows videos from the hemispherical tip when used to image organs of a mouse. Fig 6.7(a)-(e) are examples from mouse esophagus. These mice were developed as a model to study Barrett's esophagus. When Barrett's esophagus develops in mice, unlike human, a

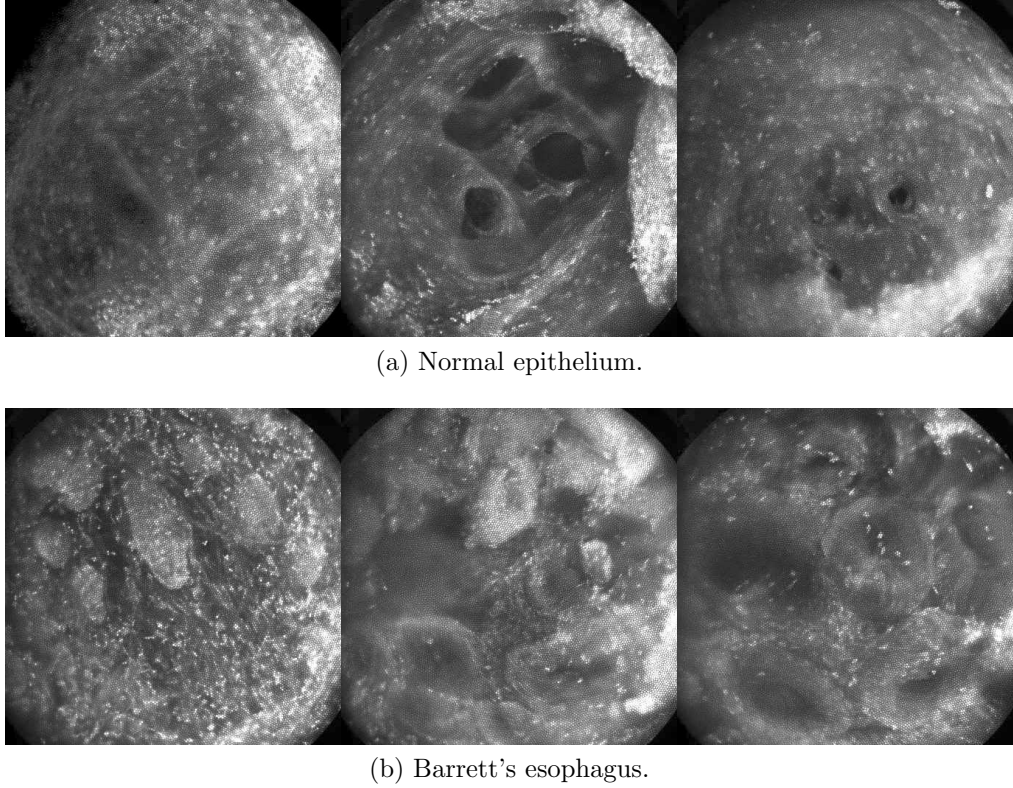


Figure 6.6: *Ex vivo* human esophagus results using a thirty-thousand element fiber with a hemisphere tip. Acridine orange was topically applied as the fluorescent contrast agent. Captions indicate tissue diagnosis. (Circular field of view is 700 μm .)

keratin layer develops. We believe the strong contrast seen in Fig 6.7(a) is due to a thick keratin layer and that a thinner keratin layer is present in Fig 6.7(b). Fig 6.7(d) appears to be normal epithelium. The bare fiber has good performance when imaging large flat organs such as the tongue in Fig 6.7(f).

Of particular interest is the distinct difference in the image quality obtained when imaging in the colon (Fig 6.7(g)) versus the eye socket (Fig 6.7(h)-(i)). The colon images appear to have significantly more background signal reducing the overall image contrast. Since the colon is designed to absorb, it is likely that this tissue rapidly transfers topically ap-

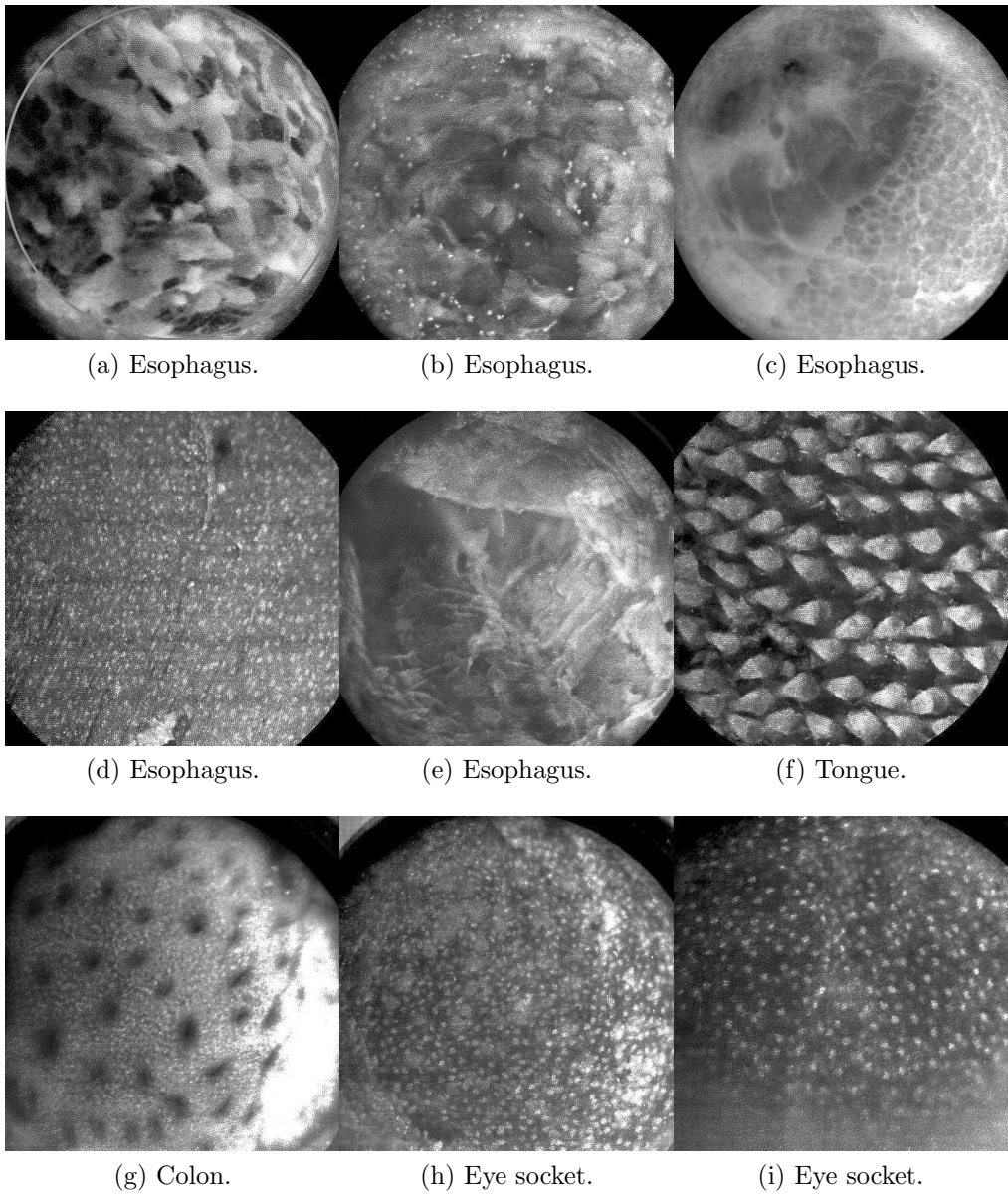


Figure 6.7: *In vivo* mouse results using a thirty-thousand element fiber with a hemisphere tip. Acridine orange was topically applied as the fluorescent contrast agent. Captions indicate region imaged. (Circular field of view is 700 μm .)

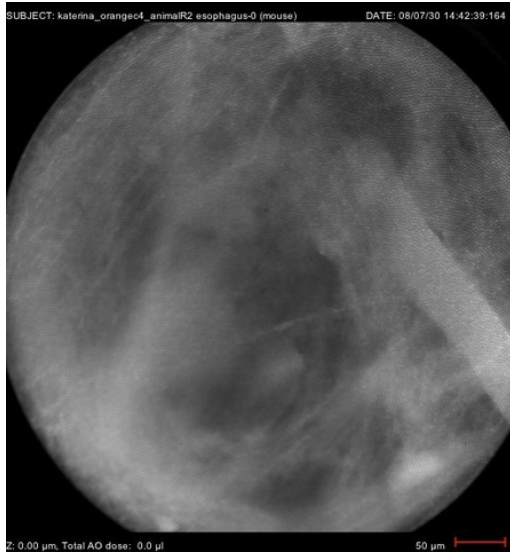


Figure 6.8: (VIDEO) *In vivo* video of mouse results using a thirty-thousand element fiber with a hemisphere tip. Acridine orange was topically applied as the fluorescent contrast agent. Captions indicate region imaged. (Circular field of view is 700 μm .) Video URL: <http://www.tanbakuchi.com/permanent/dissertation/Ch6V1.mov>

plied contrast agent into the tissue making a more uniform fluorophore distribution in depth. As the Monte Carlo results in Fig 6.4 indicate, the image quality should significantly degrade when the contrast agent distribution becomes axially uniform. The images from the eye socket epithelium have much better contrast indicating that the tissue membrane blocks the fluorophore from being absorbed into underlying tissues.

Fig 6.9 shows results when using a one-hundred-thousand element fiber bundle with a hemisphere tip imaging in mouse colon. Although the larger bundle provides larger field of view, significant falloff and aberrations are visible towards the edge of the image field. This reduction in image quality is present because to the optical scan unit is being used with a field larger than it was designed for.

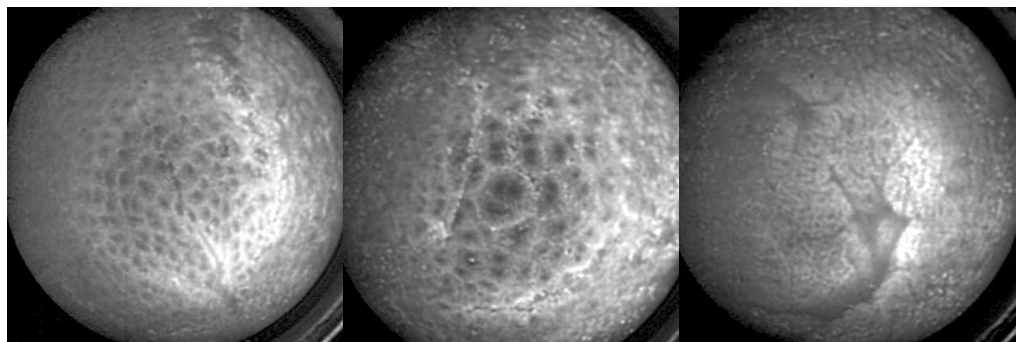


Figure 6.9: *In vivo* mouse colon results using a one-hundred-thousand element fiber with a hemisphere tip. Acridine orange was topically applied as the fluorescent contrast agent. (Circular field of view is 1.4 mm.)

Chapter 7

Conclusions

THIS DISSERTATION MADE THREE PRIMARY ACCOMPLISHMENTS. (1) The first real-time mobile clinical confocal microlaparoscope system was developed. The microlaparoscope is simple to use during surgery and integrates a contrast agent delivery system and depth scan mechanism inside of the ergonomic handle. (2) The microlaparoscope was successfully tested in humans and the results show that the device can resolve cellular morphology and sub-cellular details. (3) The imaging performance of the confocal microlaparoscope was characterized in turbid media using a Monte Carlo model. The results show that a slit aperture has degraded performance compared to pinhole apertures and future versions of the system should utilize a pinhole or pinhole array aperture.

7.1 Summary of work

A mobile confocal microlaparoscope system capable of performing live optical biopsies *in vivo* has been developed. The system is currently being

evaluated in clinical trials to assess its safety and efficacy for detecting ovarian cancer. The results in Chapter 3 show that the instrument is safe and can successfully image ovaries *in vivo*.

The confocal microlaparoscope has been successfully used in the surgical setting for *in vivo* laparoscopic imaging of the ovary. Images obtained *in vivo* with topically applied fluorescein sodium demonstrate that the device functions as designed and that the imaging procedure is safe. Due to the low contrast of topically applied fluorescein sodium, it is uncertain if it can provide sufficient contrast for diagnosis of ovarian pathology. *Ex vivo* images obtained with AO show excellent contrast that highlights cellular morphology and sub-cellular details. Preliminary evidence shows that the same contrast can be obtained *in vivo*.

The microlaparoscope described in Chapter 2 represents a new type of *in vivo* diagnostic imaging device and offers several advantages. With its ability to image cellular details in real time, it has the potential to aid in the early diagnosis of cancer. Rather than biopsying tissue, sending samples for analysis, and waiting for tissue processing, the microlaparoscope system instantly displays live cellular images at thirty frames per second whenever the device contacts the tissues. Nondestructive optical biopsy enables more extensive interrogation than traditional methods allow. Initially, the device may be used to locate unusual regions for guided biopsies. In the long term, the device may be able to supplant traditional biopsies altogether and allow the surgeon to identify early stage ovarian cancer *in vivo*.

It is difficult to characterize the slit-scan confocal microlaparoscope's performance through *in vivo* testing. Therefore, a Monte Carlo model was developed and implemented to study the performance and limitations of

parallelized fluorescence confocal systems. The results in Chapter 4 indicate that although a slit aperture offers high speed imaging, its axial and lateral performance is degraded. When imaging at a reasonable depth of $d \cdot \mu_s = 0.5$ with an NA of 0.5, a 1.5 μm by 450 μm micron slit has about an order of magnitude worse axial and lateral performance as compared to a 1.5 μm diameter pinhole aperture. Sparse parallelized apertures such as a linear pinhole array and a Nipkow aperture can be optimized to achieve fast imaging with performance comparable to a single pinhole aperture. The results also show that performance for all apertures degrades significantly for depths greater than two mean free paths.

The results of this study indicate that the lateral performance of a confocal system imaging in tissue is likely to be limited by scattering and not diffraction effects. This result is useful for the optical designer. For example, it would be wasteful to optimize a system for diffraction limited performance when tissue scattering imposes the overall limit on image quality.

In addition to modeling aperture effects, we also investigated how the tissue's non-radiative absorption coefficient μ_a , scattering anisotropy g factor, and fluorescence absorption coefficient μ_f affect system performance. We found that the tissue absorption coefficient and anisotropy have little effect on the system performance for typical ranges encountered in tissue. We found that the best imaging performance is achieved when the fluorescence absorption coefficient is small relative to the scattering coefficient. Since the fluorescence coefficient is directly coupled to the amount of collected signal, there is a competition between increasing μ_f to increase the signal to noise ratio and decreasing μ_f to improve the lateral and axial system performance. Therefore, the system designer and user of a confocal system

must determine the appropriate balance between signal to noise ratio and the axial and lateral resolution.

7.2 Future work

In the future, we will continue to investigate the wide range of potential applications for the confocal microlaparoscope system. We plan to quantitatively evaluate the sensitivity and specificity of the microlaparoscope when used to detect ovarian cancer. We will also continue to evaluate potential contrast agents that are safe for *in vivo* use and that provide diagnostically useful contrast.

Because the microlaparoscope is based on an inherently flexible fiber bundle, we plan on making a device with a flexible probe. We have previously shown a flexible imaging catheter (see Appendix Fig A.5) and plan to apply the technology developed for the microlaparoscope to a new confocal microgastroscope for interrogating the gastrointestinal tract. Chapter 5 presents a new miniature lens for use with future microlaparoscopes and microgastrosopes. The new lens improves dye delivery, increases the confocal sectioning, increases the system resolution and number of detection elements, and doubles the working spectral bandwidth.

Since the results of the Monte Carlo modeling indicate that a slit-scan system has severely limited axial and lateral performance in scattering media, the optical scan unit (OSU) should be redesigned to use a point or multi-point scan system. While redesigning the OSU, further advancements may be obtained by integrating real-time full field spectral collection using a secondary optical path (shown in Appendix Fig A.32). In addition,

since most biopsies are sliced cross-sectionally rather than en-face, the scan system could be modified to provide real time cross-section scans.

Chapter 6 showed that bare fiber probes with contoured tips can easily image inside small lumens. Future studies should be done to determine if the probes can provide sufficient resolution to diagnose diseases.

APPENDICES

Appendix A

Microlaparoscope design details

A.1 First generation design

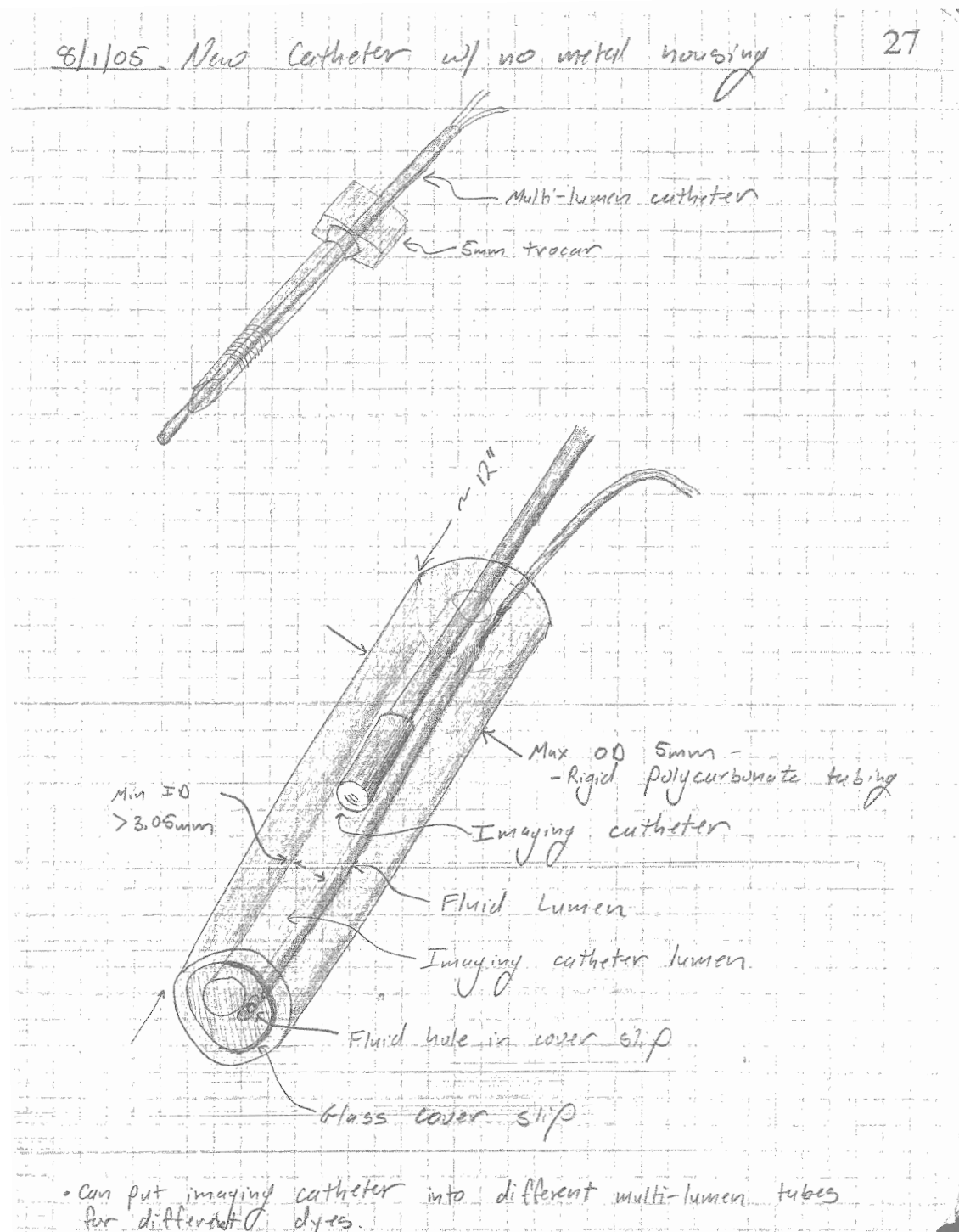


Figure A.1: First generation microlaparoscope sketch.

Single mount point catheter connector

8/1

111

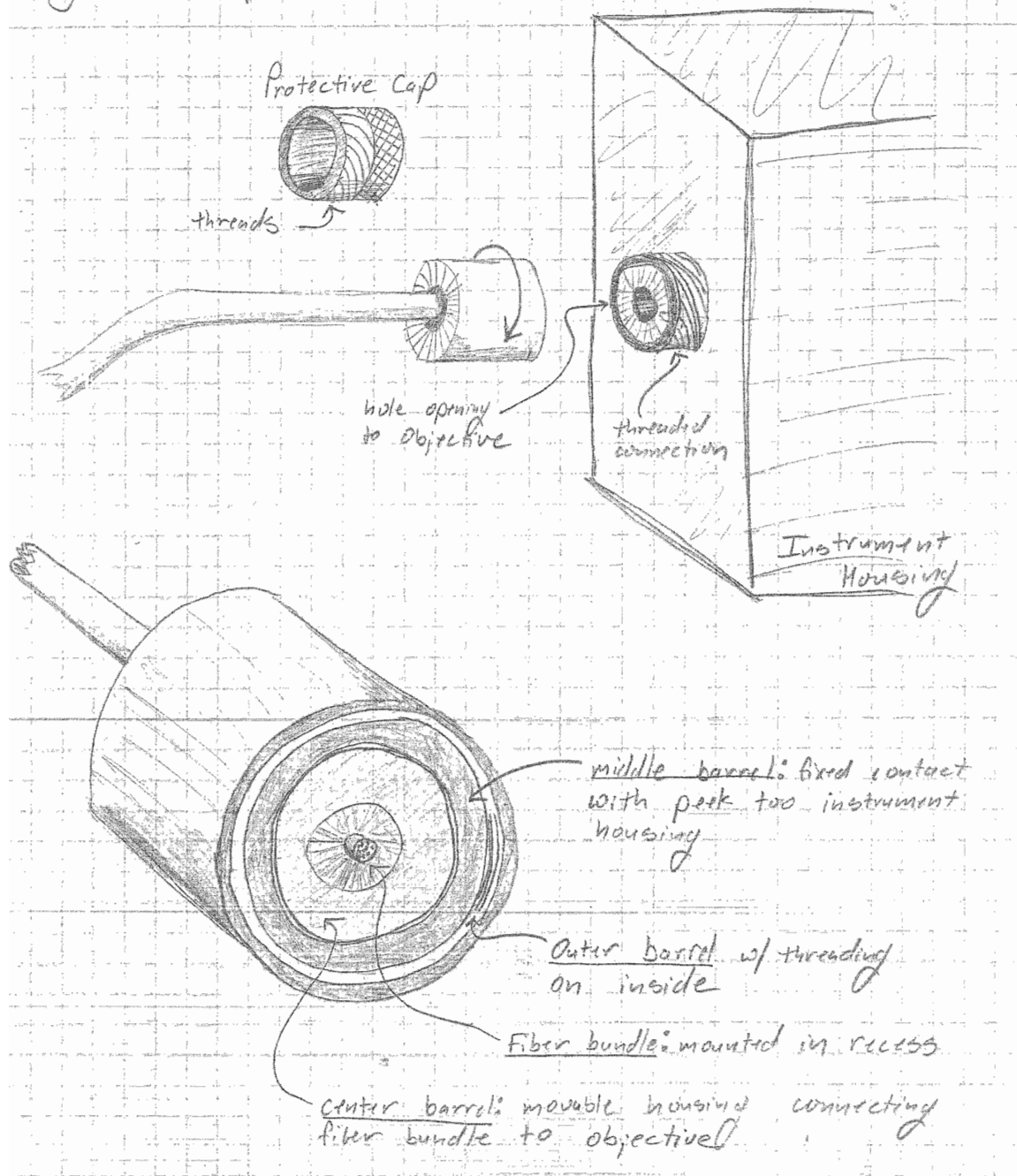
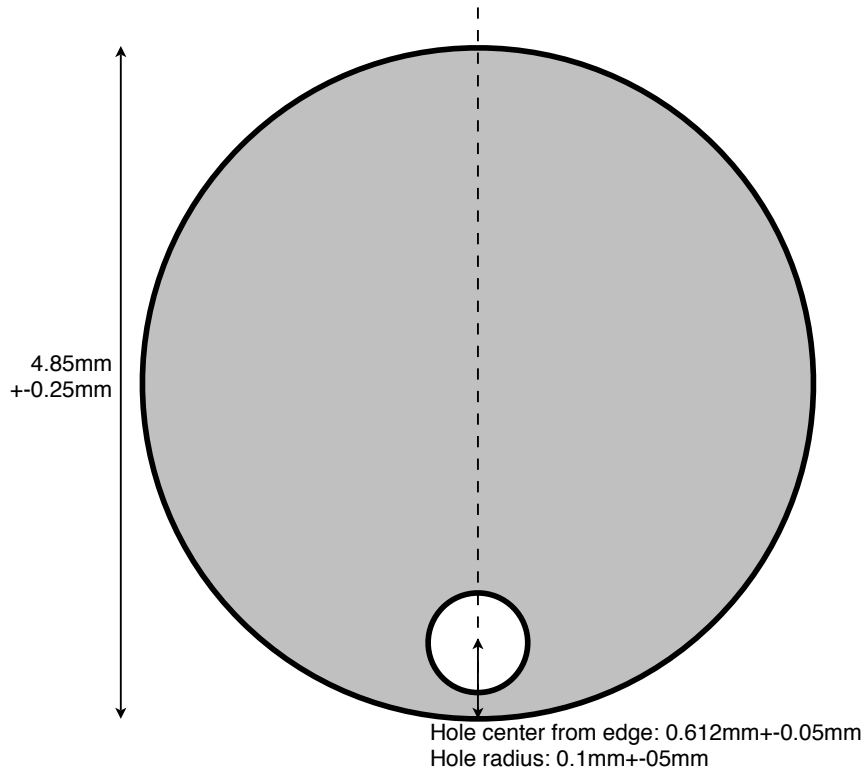


Figure A.2: Optical scan unit connector sketch.

Anthony Tanbakuchi, Radiology Research Labs, University of Arizona

Fluid Dispersing Cover Slip A.1



Design:

The fluid dispersing cover slip consists of a circular piece of plane parallel plate optical quality glass (microscope cover slip) with a drilled hole that passes fluid from the rear to the front.

Material:

Glass cover slip 160um thick.

Monday, June 6, 2005, pages 1 of 1

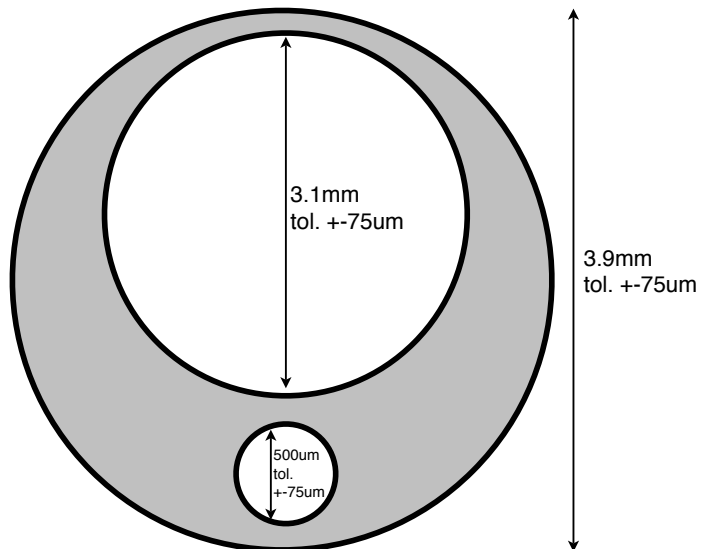
Figure A.3: First generation microlaparoscope coverslip design.

Anthony Tanbakuchi, Radiology Research Lab, University of Arizona

Multi-lumen tube design A.3

Tube Design:

The tube consists of a central lumen with one micro lumen.



Material:

Our requirements:

- medical grade for surgical use
- sterilize-able (chemically or thermally)
- rigid like PEEK or other hard tubing

Our thoughts on a material choice: Nylon 12 or PEEK.

Tuesday, July 5, 2005, pages 1 of 1

Figure A.4: First generation microlaparoscope multi-lumen housing.

A.2 Second generation design

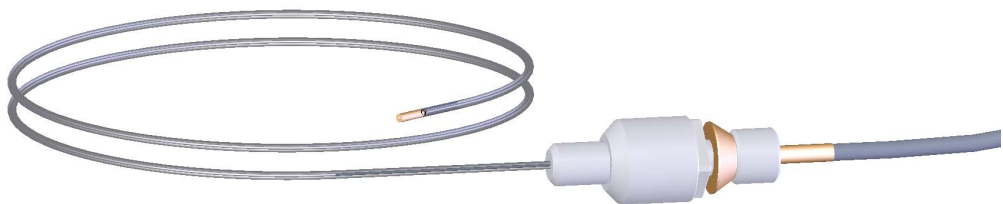


Figure A.5: Second generation microlaparoscope flexible design. Instead of a rigid tip, a flexible plastic tubing is used to house the fiber bundle and hold the miniature objective lens.

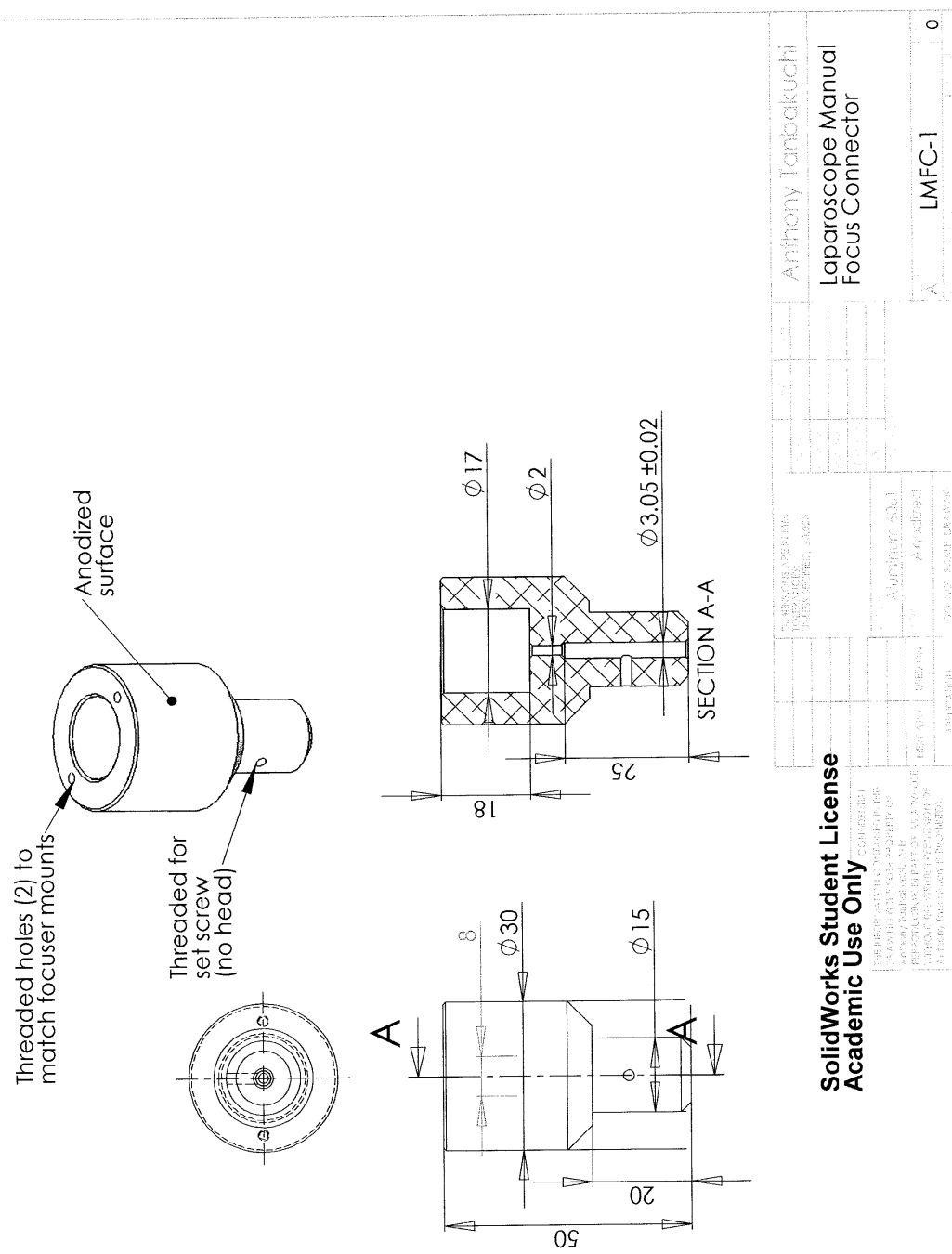


Figure A.6: Second generation manual focus design.

A.3 Third generation design

Thread info 2-56 for small holes in focus fiber holder, 4-40 elsewhere.

Set screws 2-56 x 1/16, cup point; 4-40 x 1/8 cup point.

Spring Small Parts Item: MW Comop Spring 0.300OD x 0.030WD x 1FL,
part number CSMW-0127-02, Mer: 013156-02

Focus coupling cover plate Design change made manually to cover plate.

It was shortened by 2 mm to allow mounting screw heads to fit.

Handle switch issues Motor 2 was introducing some noise on the switch lines (causing button 2 to randomly fire). Had to introduce some capacitors between the switch line and ground at the controller board to filter out this high frequency noise.

Stepper motors Use 2 Zaber NA08A16 stepper Motors with the TCD1000 controller via serial to usb adapter.

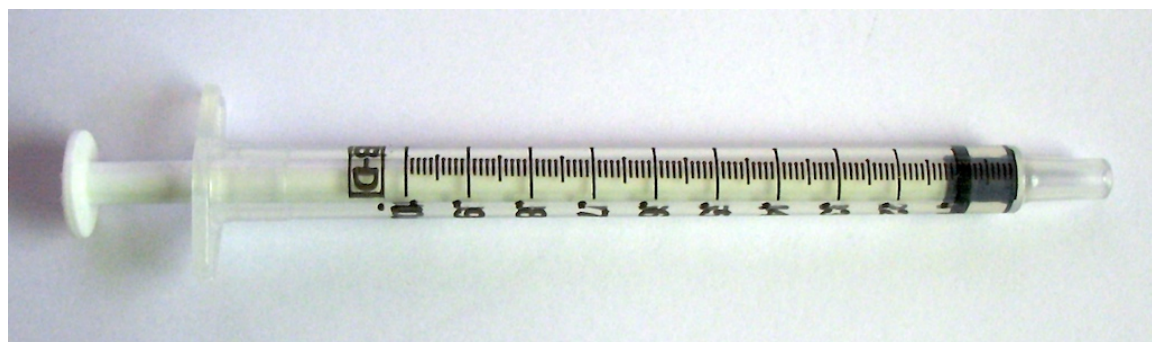
Button controller Use Universal joystick controller BU0836x from www.leobodnar.com. This acts as the button controller using the USB HID library.

Handle grip Uses the Cyber-Tech www.cyber-tech.net 8501-RB with 2 switches, 2 triggers, all button have a rubber water seal jacket. Wiring was for the DC setup.

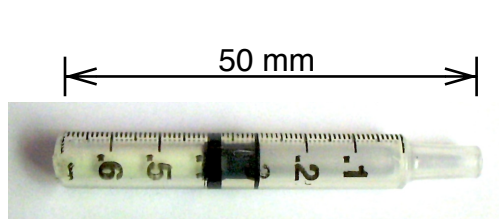
Handle cable to osu Cables Unlimited 25 foot Straight Thru RS232 DB25 M/F 2C, PCM-1600-25 .

Rigid tip housing The rigid 3 mm tip housing is AISI 304 stainless steel tubing purchased from Unimed S. A. in Switzerland. Article 160 / 200.010-A OD 3 mm, ID 1.01 – 1.05 mm.

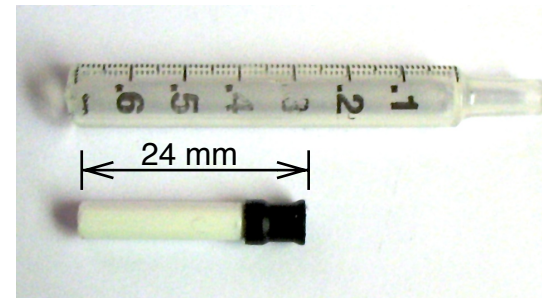
Syringe The system uses a BD 1 mL tuberculin slip tip syringe (Ref # 309602). The syringe plunger is retracted to the 0.3 mL mark and then cut on a band saw. The ends are smoothed and the syringe is sterilized before use. See figure A.7.



(a) BD 1 ml tuberculin slip tip syringe



(b) cut syringe



(c) individual cut components

Figure A.7: Third generation microlaparoscope syringe.

Mechanical drawings

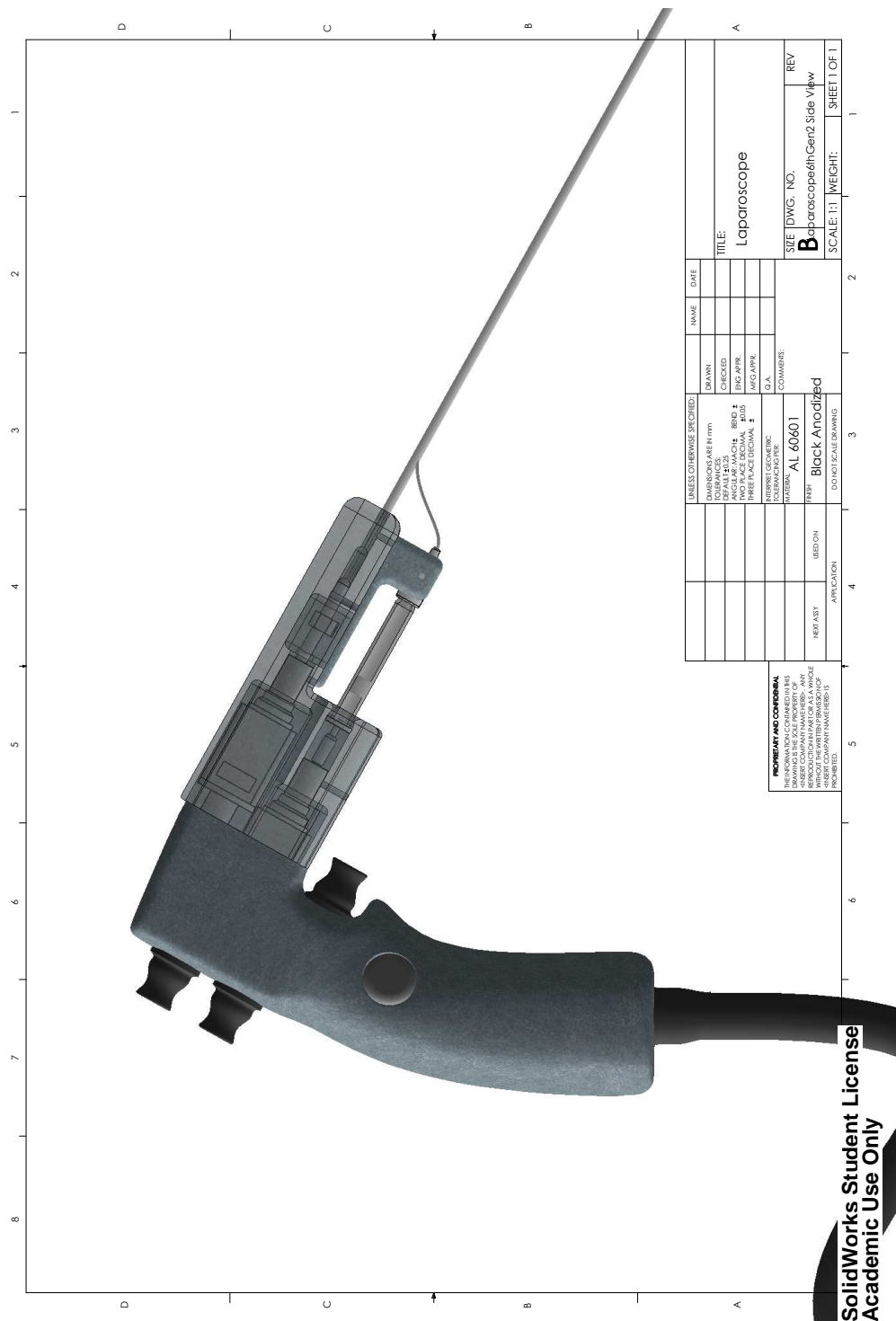


Figure A.8: Third generation microlaparoscope. Motor housing is transparent to show internal components.

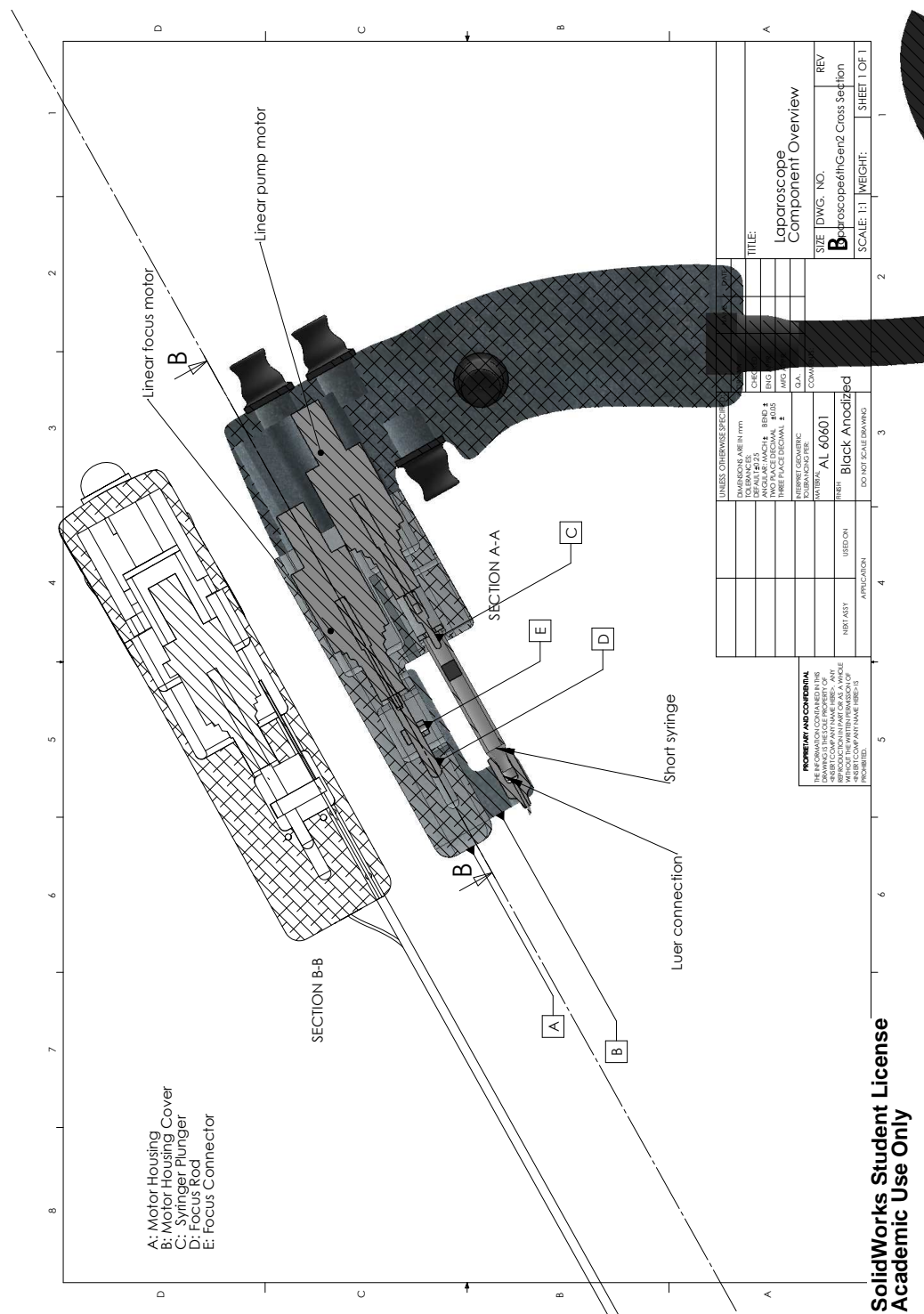
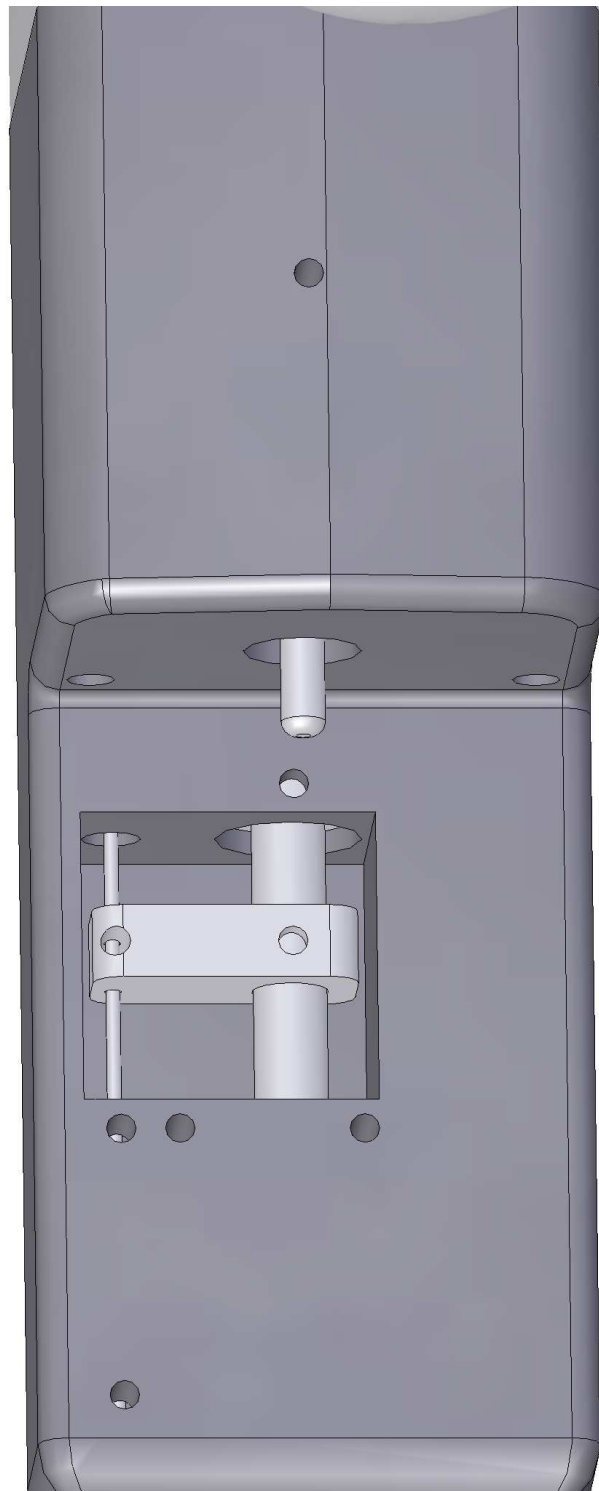


Figure A.9: Third generation microlaparoscope. Side view and top view.



SolidWorks Student License
Academic Use Only
X

Figure A.10: Looking up into the focus coupling inside the motor housing.

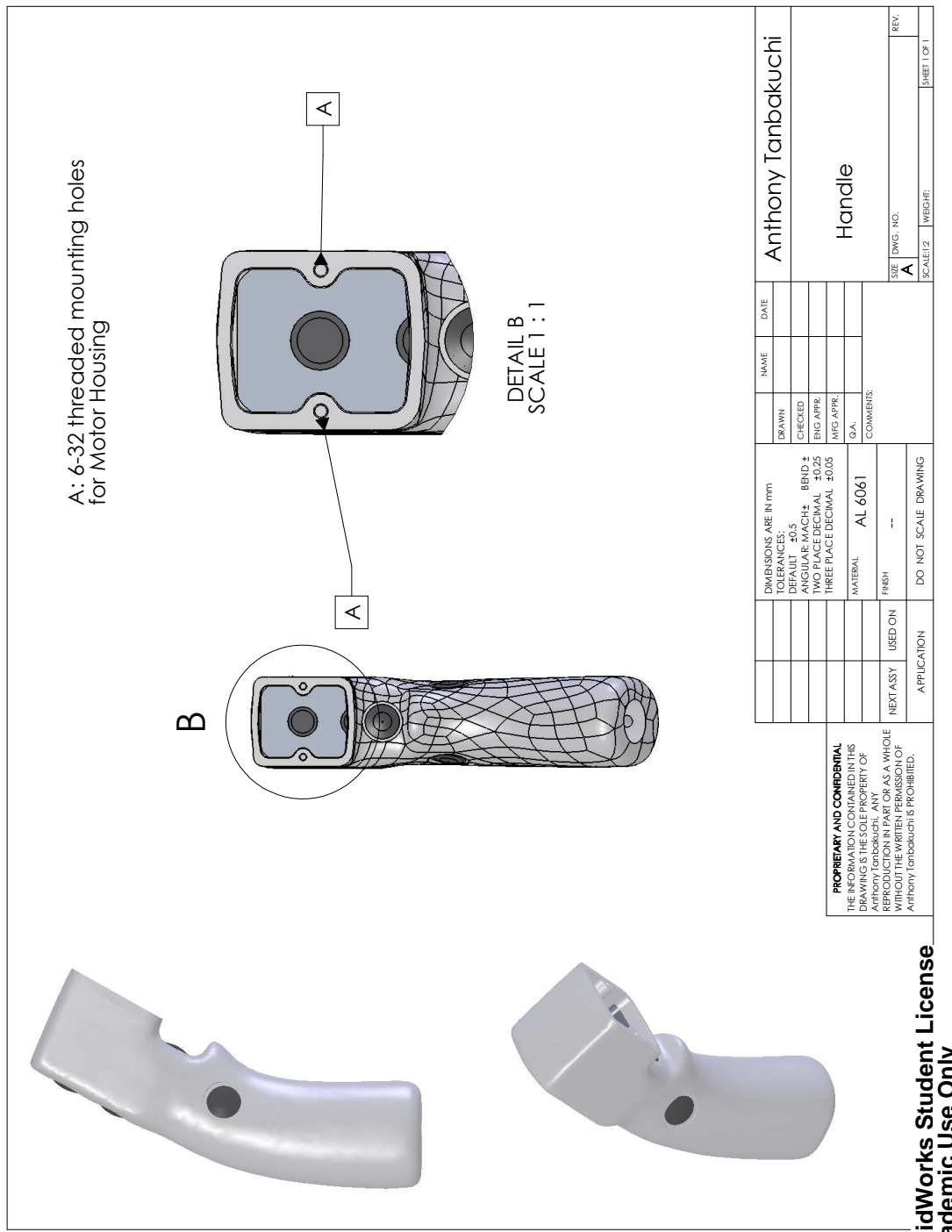


Figure A.11: Microlaparoscope handle Cyber-Tech model number 8501-RB (solid model geometry obtained from Cyber-Tech).

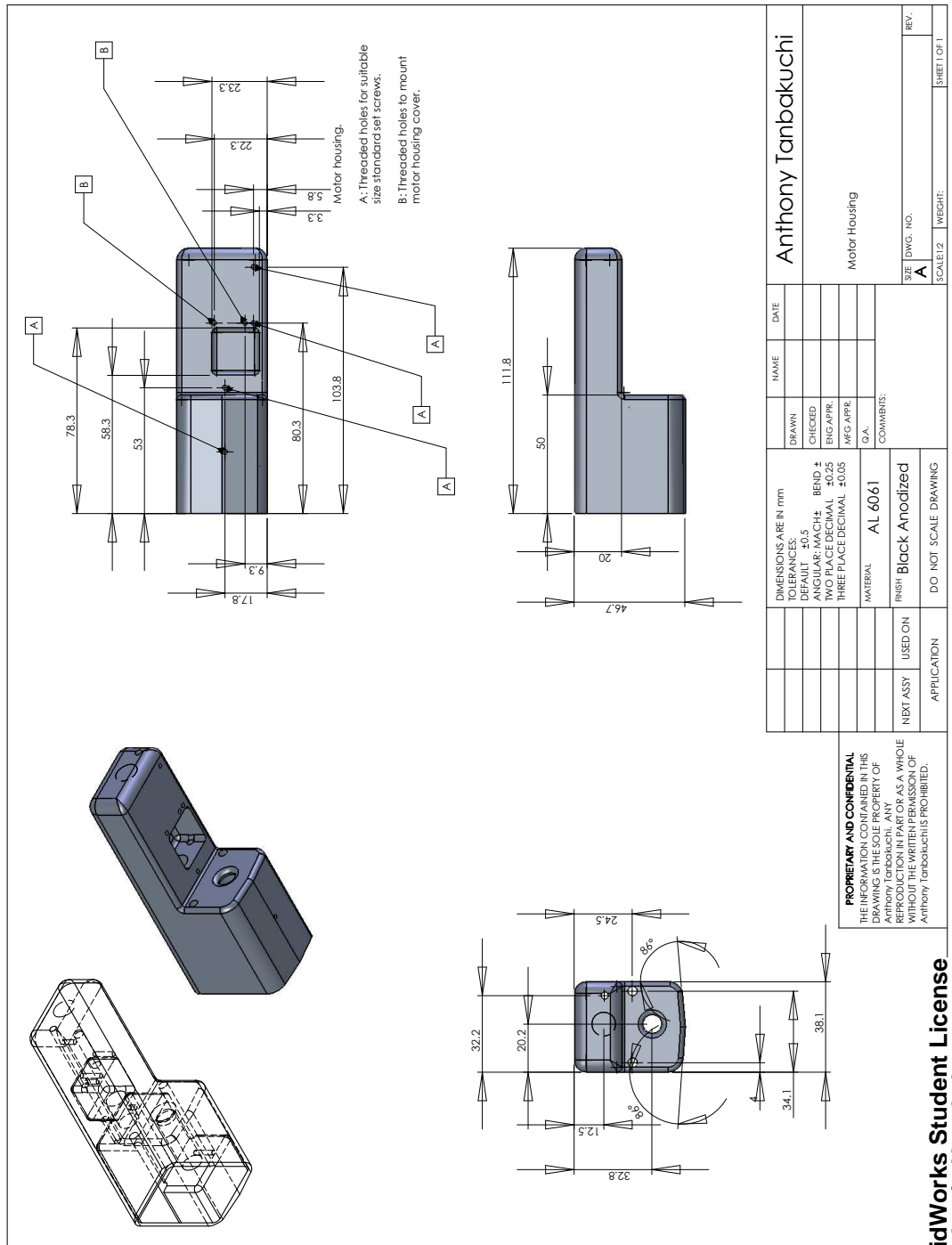


Figure A.12: Motor housing.

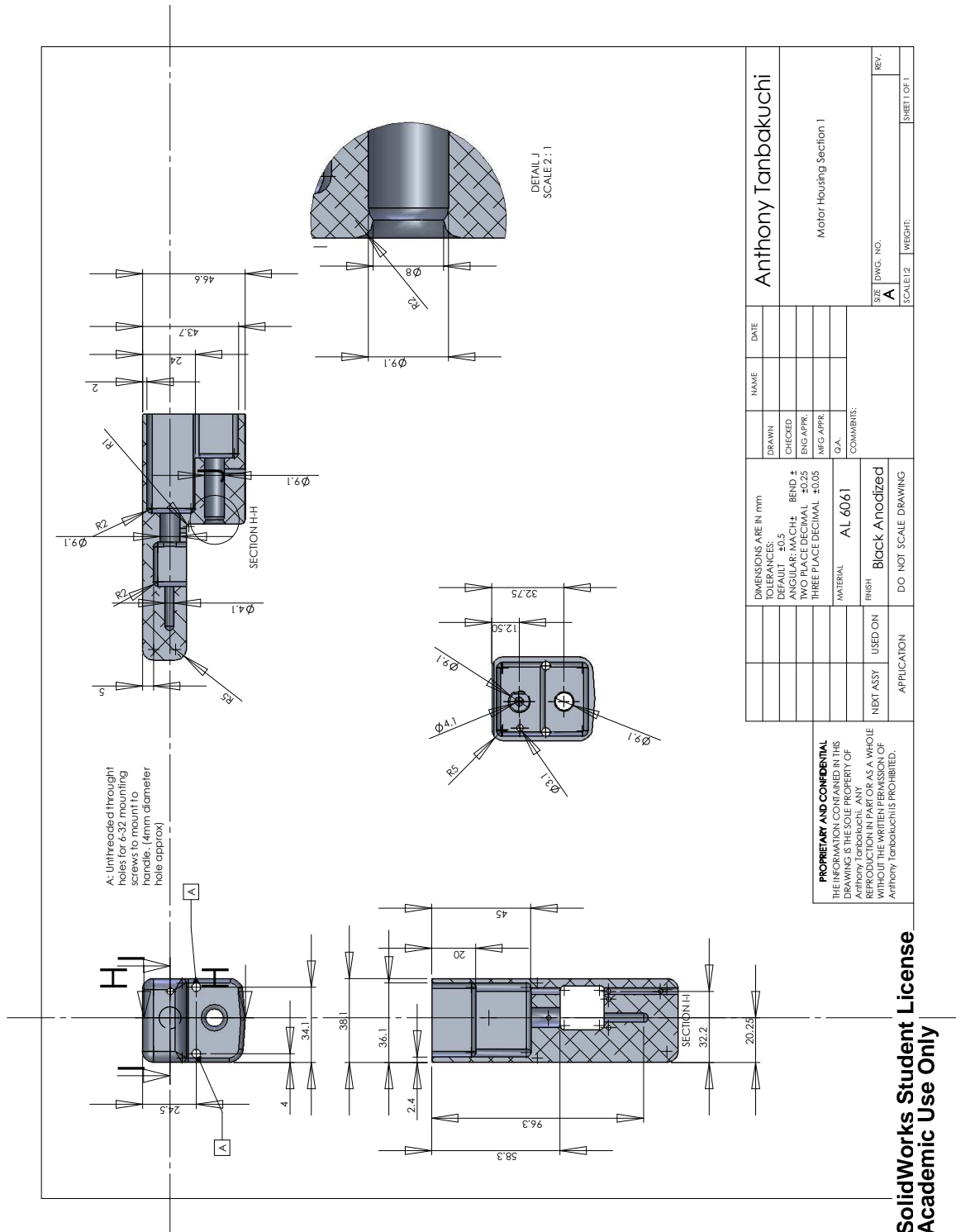


Figure A.13: Motor housing cross-section.

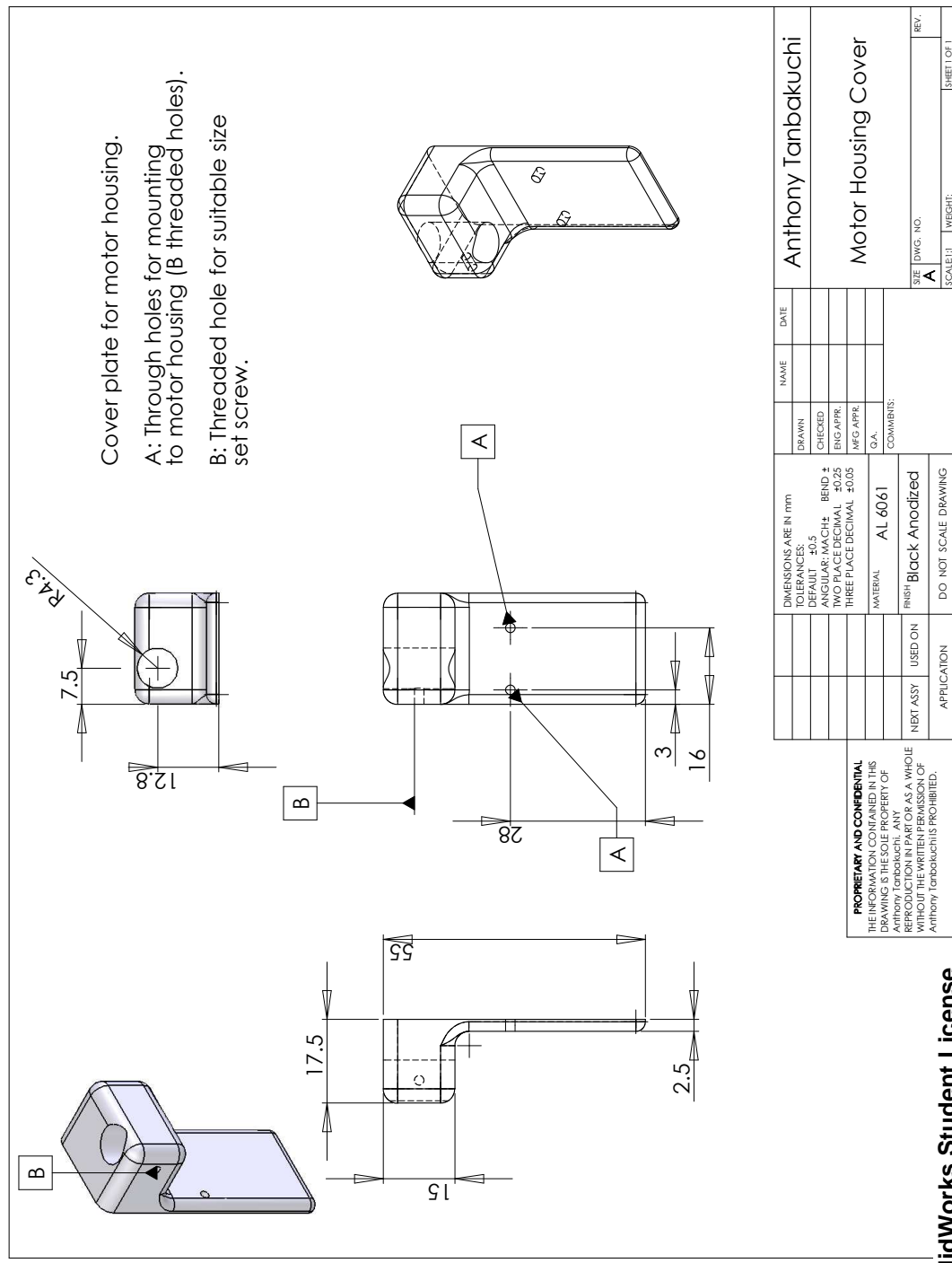


Figure A.14: Motor housing cover.

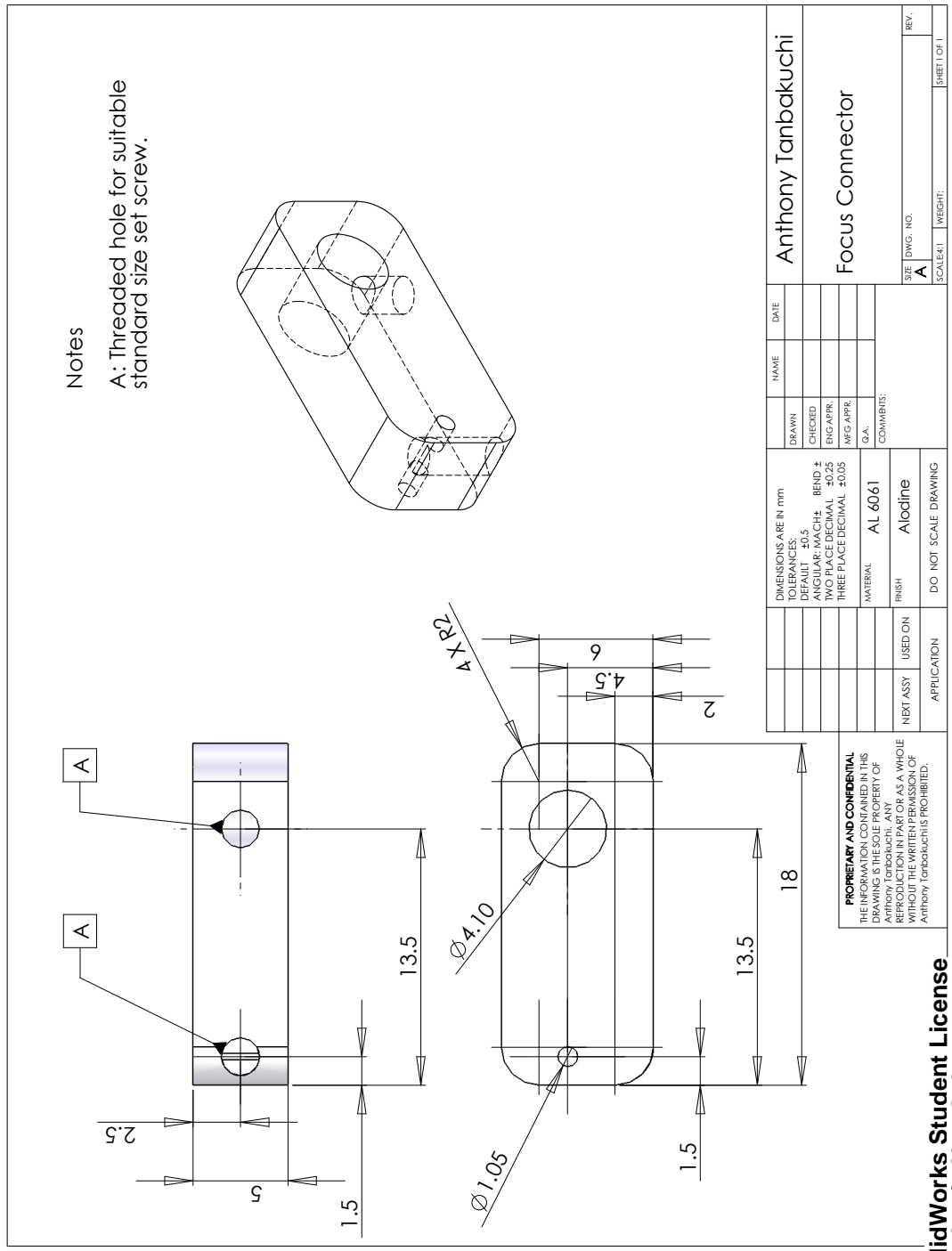


Figure A.15: Focus connector. Bridges the focus rod to the fiber bundle.

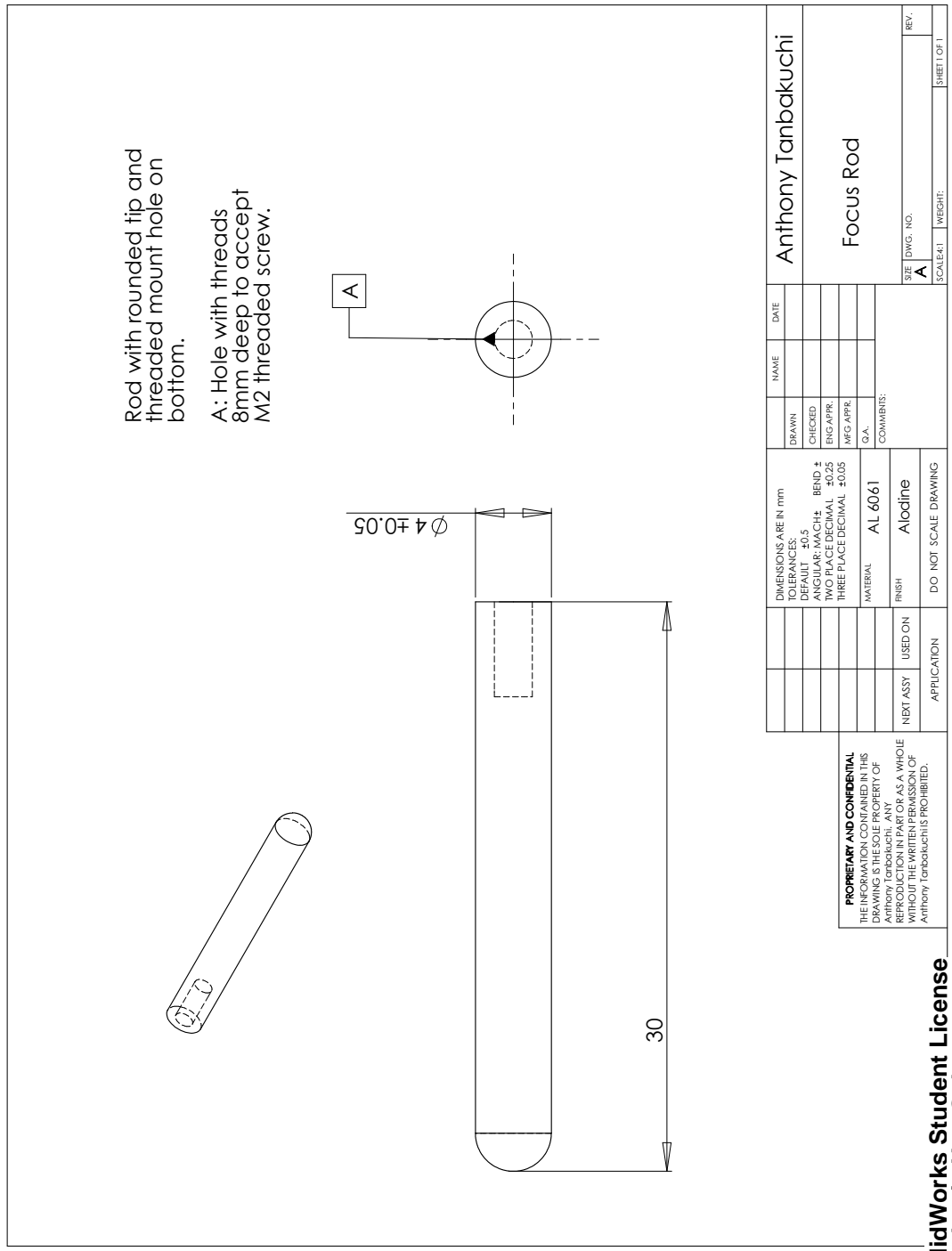


Figure A.16: Focus rod.

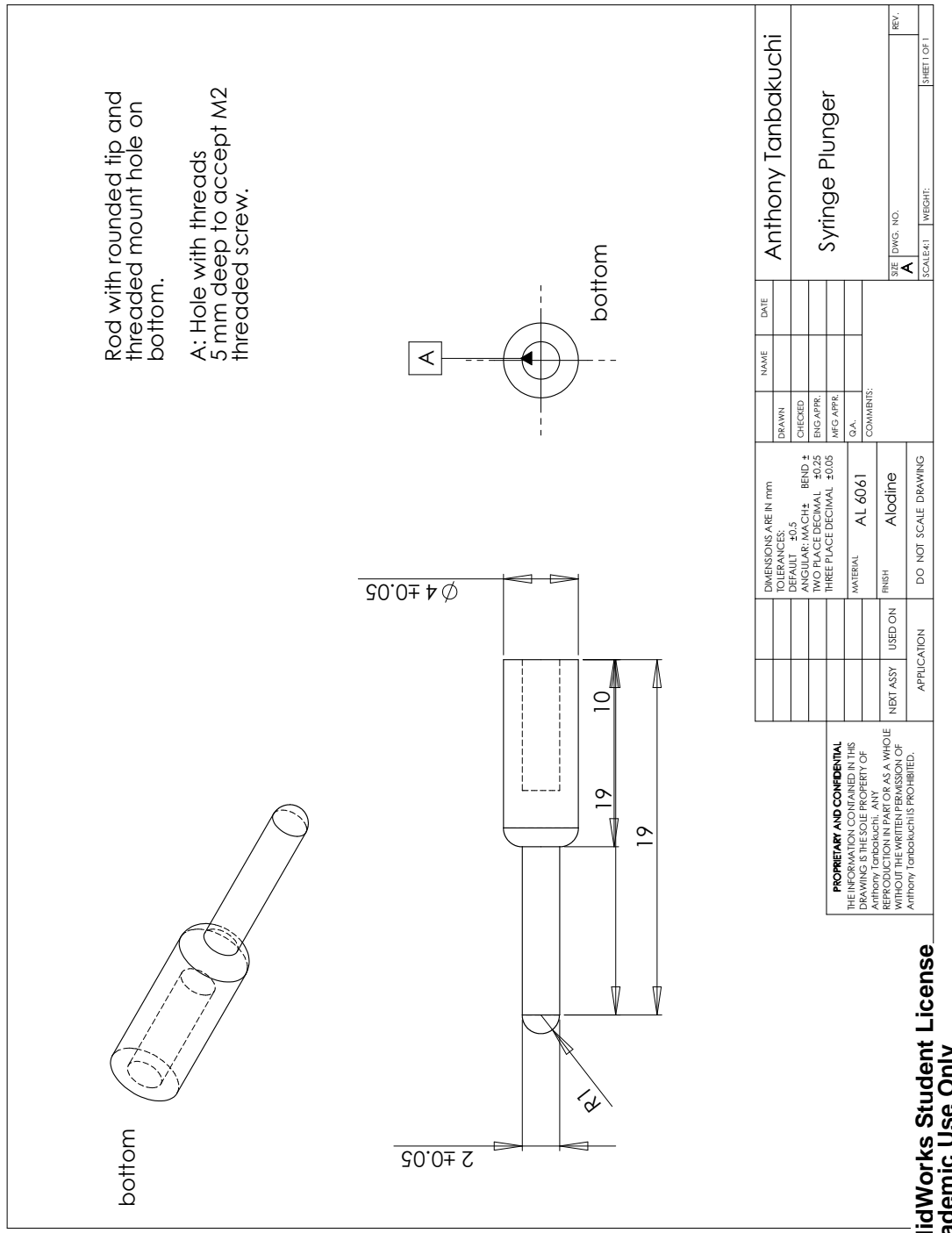


Figure A.17: Syringe plunger.

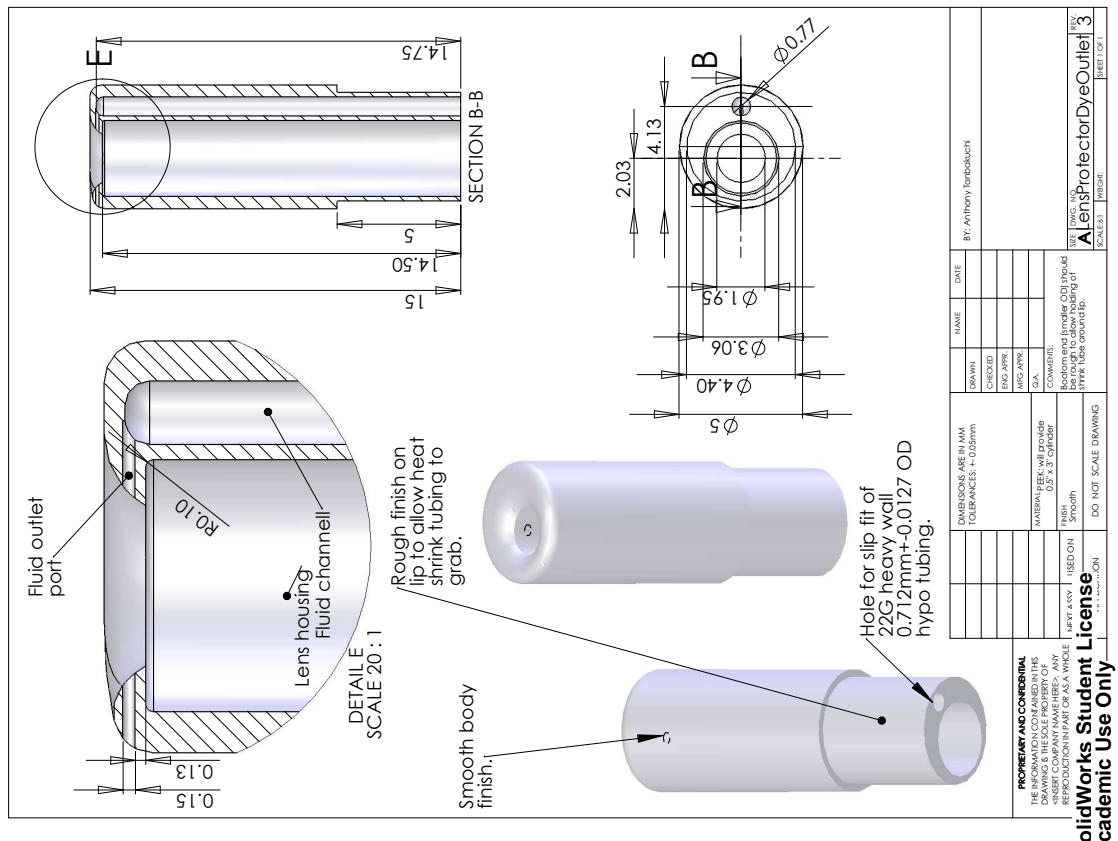


Figure A.18: Lens protector and dye outlet.

Laparoscope Handle Wiring Information

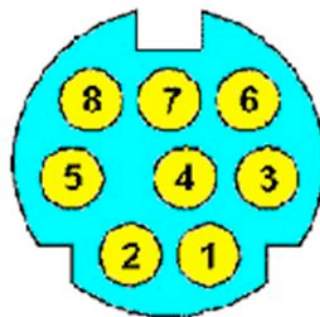
Cables Unlimited 25' Straight Thru RS232 DB25 M/F 2C, PCM-1600-25

Software Mapping	proximal cart connection	RS232 DB25 color	RS232 pin	distal handle connection	device connection	device
	black	blue-green		pink:white	pin 1	motor 1
	brown	blue-green:black		pink	pin 2	motor 1
	red	salmon		green	pin 3	motor 1
	orange	salmon:black			pin 4	motor 1
	yellow	white		green:white	pin 5	motor 1
	green	white:black		pink:light pink	pin 6	motor 1
	blue	green		yellow	pin 7	motor 1
	purple	green:black		black:white	pin 8	motor 1
	black	blue		pink:white	pin 1	motor 2
	brown	blue:black		pink	pin 2	motor 2
	red	light-blue		green	pin 3	motor 2
	orange	light-blue:black			pin 4	motor 2
	yellow	pink		green:white	pin 5	motor 2
	green	pink:black		pink:light pink	pin 6	motor 2
	blue	lavender		yellow	pin 7	motor 2
	purple	lavender:black		black:white	pin 8	motor 2
		grey				
		grey:black				
BID3	black	yellow			button 3	handle
	brown	yellow:black				
BID 4	red	red		black	button 4	handle
BAD!!!	orange	red:black		orange		
BID 5	yellow	orange		yellow	trigger 1	handle
BID 2	green	orange:black		brown	trigger 2	handle
GND	blue	black		red	common	handle
	purple	bare		green	ground	handle

Figure A.19: Wiring diagram. (Page 1)

Laparoscope Handle Wiring Information

Note that button ID 1 (BID 1) seems to be out of order on the controller board.
 Zaber T-CD Pin Diagram for motor connection

T-CDxxxx Minidin 8 Motor Connector Pin Diagram

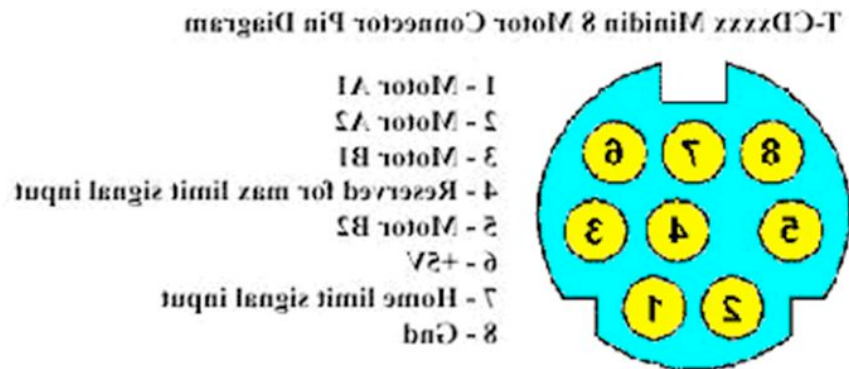
- 1 - Motor A1
- 2 - Motor A2
- 3 - Motor B1
- 4 - Reserved for max limit signal input
- 5 - Motor B2
- 6 - +5V
- 7 - Home limit signal input
- 8 - Gnd

T-CD Black motor extension cable pin wire colors

pin	wire color
1	black
2	brown
3	red
4	orange
5	yellow
6	green
7	blue
8	purple

Figure A.20: Wiring diagram. (Page 2)

Laparoscope Handle Wiring Information



NA08A16 Wire to Pin Colors

pin	wire color
1	pink:white
2	pink
3	green
4	
5	green:white
6	pink:light pink
7	yellow
8	black:white

Figure A.21: Wiring diagram. (Page 3)



University Research Instrumentation Center
 Prototype Machining & Design Facility
 Fabrication & Welding Facility
 1040 East 4th Street, West Annex 235
 Tucson, Arizona 85721-0077
 (520) 621-6758 / FAX (520) 621-6333

QUOTATION

Date: 05/28/08
 Quote Number: Q4101 1250
 Revision Number: 0

Customer: Radiology Research Lab
 Attention: Anthony Tanbakuchi
 Address: University of Arizona
 Tucson, AZ 85724
 Phone: 520-626-4500
 FAX/Email: kuchi@email.arizona.edu

Estimated Completion Date: 2-3 weeks ARO
 Quote Prepared By: Larry Acedo

Drawing # / Part Description	Item	Quantity	Unit Price	Extended Price
MOTOR HOUSING	M	2.00	347.00	694.00
MOTOR HOUSING COVER	M	2.00	166.00	332.00
SYRINGE PLUNGER	M	2.00	31.50	63.00
FOCUS ROD	M	2.00	36.00	72.00
FOCUS CONNECTOR	M	2.00	71.00	142.00
MATERIALS, BLACK ANODIZE, ALODINE		1.00	200.00	200.00

TOTAL: \$1,503.00

Modifications to submitted prints will only raise the cost if an increase in labor and/or materials is required.
 Material and shipping costs are estimates only and are based on current market value and availability.

Figure A.22: Microlaparoscope housing quotation. (Page 1)



University Research Instrumentation Center
Prototype Machining & Design Facility
Fabrication & Welding Facility
1040 East 4th Street, West Annex 235
Tucson, Arizona 85721-0077
(520) 621-6758 / FAX (520) 621-6333

QUOTATION

Date: 05/28/08
Quote Number: Q4101 1249
Revision Number: 0

Customer: Radiology Research Lab
Attention: Anthony Tanbakuchi
Address: University of Arizona
Tucson, AZ 85724
Phone: 626-6500
FAX/Email: kuchi@email.arizona.edu

Estimated Completion Date: 2-3 weeks ARO
Quote Prepared By: Larry Acedo

Drawing # / Part Description	Item	Quantity	Unit Price	Extended Price
MOTOR HOUSING	M	1.00	473.00	473.00
MOTOR HOUSING COVER	M	1.00	221.00	221.00
SYRINGE PLUNGER	M	1.00	63.00	63.00
FOCUS ROD	M	1.00	48.00	48.00
FOCUS CONNECTOR	M	1.00	95.00	95.00
MATERIALS, BLACK ANODIZE, ALODINE		1.00	200.00	200.00

TOTAL: **\$1,100.00**

Modifications to submitted prints will only raise the cost if an increase in labor and/or materials is required.
Material and shipping costs are estimates only and are based on current market value and availability.

Figure A.23: Microlaparoscope housing quotation. (Page 2)



University Research Instrumentation Center
 Prototype Machining & Design Facility
 Fabrication & Welding Facility
 1040 East 4th Street, West Annex 235
 Tucson, Arizona 85721-0077
 (520) 621-6758 / FAX (520) 621-6333

QUOTATION

Date: 07/24/08
 Quote Number: Q4101 1284
 Revision Number: 2

Customer: Radiology Research Lab
 Attention: Anthony Tanbakuchi
 Address: University of Arizona
 Tucson, AZ 85721
 Phone: 626-4500
 FAX/Email: kuchi@email.arizona.edu

Estimated Completion Date: 1-2 weeks ARO
 Quote Prepared By: Larry Acedo

Drawing # / Part Description	Item	Quantity	Unit Price	Extended Price
LENS PROTECTOR DYE OUTLET REV. 3	M	1.00	252.00	252.00
TOOLING		1.00	20.00	20.00

TOTAL: \$272.00

Modifications to submitted prints will only raise the cost if an increase in labor and/or materials is required.

Material and shipping costs are estimates only and are based on current market value and availability.

Thank you for the opportunity to provide you with this quote. All quotes are valid for 30 days. If changes are requested, a revision will be done and the original quote will be invalid. Please contact us if you have further questions.

Please sign and fill out the following information to accept this quote:

Signature: _____

Drwgs/Plans Submitted

Account #: _____

Obj. Code: _____

IDB: _____

Figure A.24: Lens protector and dye outlet quotation.

Tuesday, June 3, 2008

Larry,

Thanks for the quote, I would like to proceed with making the parts.

Please bill the work to **account #422-970. It is important that we are billed on or before June 30th for this account.**

Please manufacture 1 of each of the following parts to make a complete set:

- A: Motor Housing
- B: Motor Housing Cover
- C: Syringe Plunger
- D: Focus Rod
- E: Focus Connector

The electronic files (PDF and Solidworks) can be downloaded at this link:

<http://www.tanbakuchi.com/downloads/files/LaparoscopeDrawings.zip>

Username: letmein

Password: letmein

I am also submitting with the drawings the actual handle and the 2 motors that fit inside the motor housing for checking the fit.

An overall 3d drawing (Drawing Laparoscope.pdf) and cross-sectional drawing (Drawing Laparoscope Crossection.pdf) should provide an overview of the needed parts and how they assemble in the overall instrument (a surgical laparoscope prototype). Individual 2-d drawings for the parts are also included. Parts C-E are fairly straight forward. Part A is somewhat complex.

The overall pieces form a new version of a laparoscope we are using in clinical trials. The motor housing holds 2 linear motors in place (via 2 holes with set screws that clamp down on the motor shafts). Each motor has a rod that screws onto it (parts C and D). The Motor Housing Cover acts as a cover for the access hole in the motor housing where the Focus Connector (E) bridges the Focus Rod (D) to a fiber optic bundle, allowing the motor to push and pull the fiber that exits the front of the housing through a 3 mm diameter rod housing (held in place with a set screw). The second linear motor has the Syringe Plunger (C) connected and pushed against a syringe coupled to the end of the Motor Housing Cover (B).

The solid works files include the additional existing parts that complete the instrument. Note that the Motor Housing (A) mounts with 2 screws to the handle of the device (See

Figure A.25: Manufacturing details. (Page 1)

Motor Housing Section drawing upper left figure and Handle drawing). The mismatch of motor housing height and handle height is intentional so that the internal motors will actually fit in this tight space.

Finally, all the set screw holes in parts A, B, and E can be sized and threaded to your convenience using a standard size set screw. A set screw between 2-4 mm in diameter should be sufficient.

Please let me know if you have any questions or need any clarifications.

Note that all drawings are in millimeters (they are marked as such).

Thanks for your help,

-Anthony

Anthony Tanbakuchi
Research Associate

Radiology Research Lab
University of Arizona
Building 211 Office 166
1609 N. Warren Ave.
Tucson, Arizona 85724

Office: (520) 626-4500
Fax: (520) 626-3893
Cell: (520) 481-4005
kuchi@email.arizona.edu

Figure A.26: Manufacturing details. (Page 2)

George W. Speelman
UMC/Philips Clinical Engineering Dept.
University Medical Center
1501 North Campbell Avenue
Tucson, AZ 85724
P.O. Box 245180

Tel. No.: (520) 694-4950
FAX: (520) 694-4040
UMC BPR# 3224
gspelman@umcaz.edu

January 9, 2007

SUBJECT: Inspection of Experimental Imaging Device: "MCME" (Human Subjects number BIO #06-147)

To Whom It May Concern,

On January 8, 2007, I inspected an experimental imaging device (see "Device Description") to verify that it is safe for supervised use in a clinical setting as part of the development process. The inspection consisted of the following:

- Visual Inspection
 - Overall condition of the chassis, casters, etc.
 - Access panels (not secured during inspection)
 - LASER keyswitch, "panic" switch, and other controls
 - Condition of power cord and accessories
 - Condition and availability of appropriate Personal Protective Equipment, i.e. signage and eyewear
- Electrical Safety Testing
 - Ground path resistance
 - Chassis leakage current under normal and abnormal conditions (i.e. OFF/ON, ground/no ground, normal/reversed line polarity)
- LASER Power
 - LASER module maximum power (200 mW.)
 - LASER power delivered to tip of endoscope fiber (LT 1mW)

There are several items of concern that have been discussed with the researchers responsible for this device:

- The LASER power displayed represents the power available at the aperture of the LASER module; LASER power delivered to the fiber tip is not accurately displayed. I have been assured that this can be corrected.
- There were no labels identifying the device ("Make", Model, Serial No., and Electrical Specifications). Labels are being created to correct this deficiency.

Figure A.27: Safety approval. (Page 1)

I acknowledge that this device is experimental; in its present form I would call it a “working model”. Further development is anticipated; resultant changes may require that the device be inspected again.

However, it is my opinion that none of the minor deficiencies previously noted are serious enough to preclude properly supervised use in a clinical setting. I recommend that this device be approved for use in a clinical setting by the principal developers as part of their research and development process.

Please do not hesitate to contact me if you should require any further information or assistance in this matter.

Best regards,

George W. Speelman CET, CBET

DEVICE DESCRIPTION

Name: Mobile Confocal Microendoscope (MCME)

Description: The Mobile Confocal Microendoscope (MCME) system is currently being evaluated for its efficacy in In-Vivo optical biopsy. This system provides benefits unavailable to clinicians with current diagnosis techniques, primarily real-time imaging of cellular features of interest.

(Description provided by J. Udovich)

“Manufacturer”: University of Arizona Biomedical Imaging Lab

“Model”: MCME1

“Serial No.”: 1001

NOTE 1:

05/24/2007: At the request of the investigators, I performed a visual inspection of the MCME. Clinical experience with the MCME revealed that a flexible optical fiber was unsuitable as a delivery device; the investigators developed a rigid replacement ‘scope.

This design change does not significantly affect the energy delivered to the subject, and there are no changes affecting chassis leakage current. For these reasons my original recommendation stands: continued operation, under the conditions previously noted, should be approved.

Figure A.28: Safety approval. (Page 2)

NOTE 2:

11/28/2007: At the request of the investigators, I performed an inspection of the re-packaged MCME. The device had been “cleaned-up”, i.e. previously exposed components had been provided with covers, and the components/sub-assemblies had been transferred to a more mobile enclosure. None of the changes to the system resulted in significant changes to the operation or to the delivered energy. A visual inspection was performed: the only deficiency noted was the lack of a label indicating “Make”, “Model”, and “Serial No.”; this minor deficiency was discussed with Anthony Tanbakuchi. He has agreed to attach an appropriate label. Results of the Electrical safety test showed good electrical ground path integrity. Worst-case testing showed that the on-board isolation transformer is functioning properly, i.e. leakage current values were very low.

Since re-packaging has not significantly altered the energy delivered to the subject, and since there are no items of concern related to electrical safety, my original recommendation of 01/08/2007 stands. Continued operation in a clinical setting, under the conditions previously noted, should be approved.

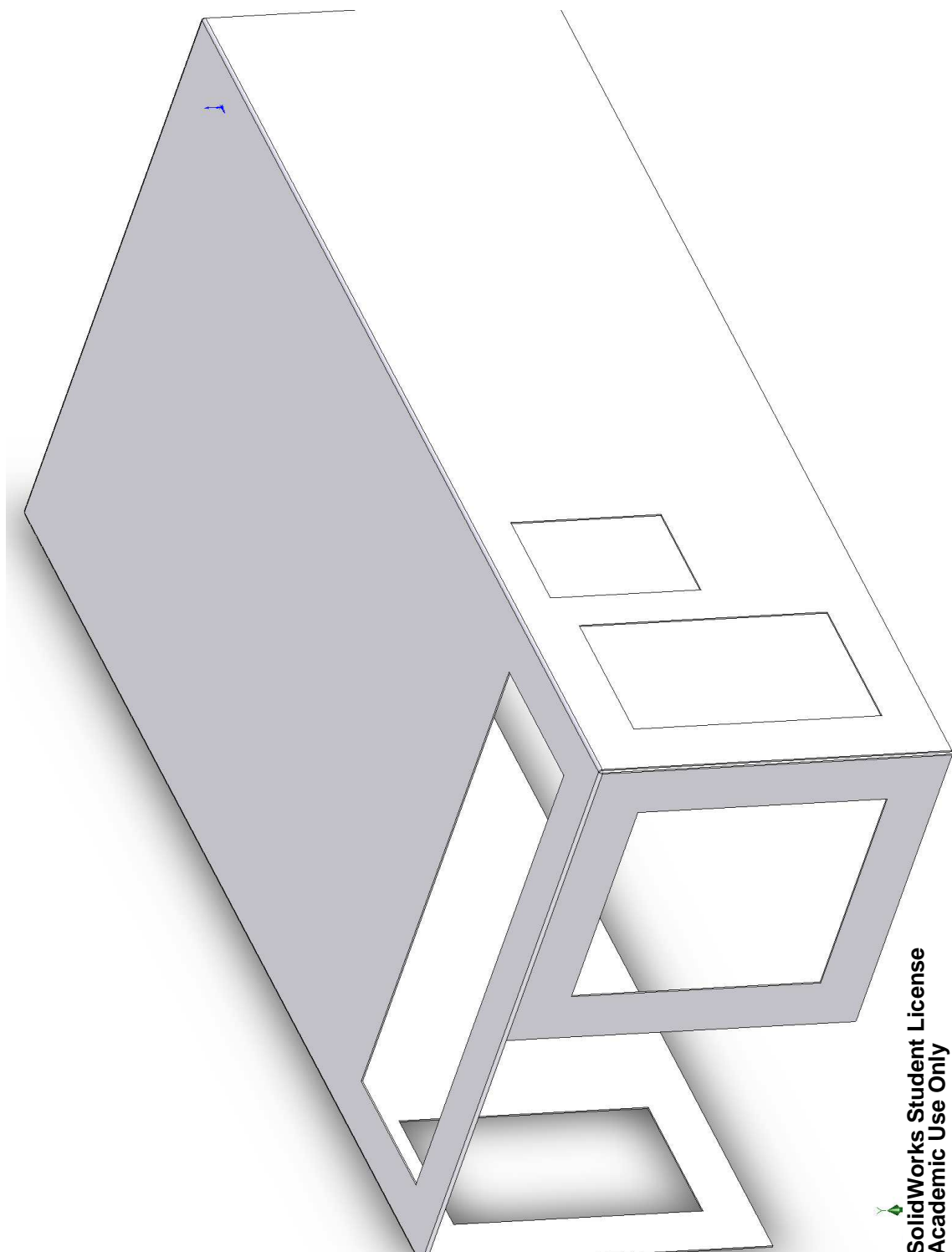
Best regards,

George W. Speelman CET, CBET

11/29/2007

Figure A.29: Safety approval. (Page 3)

Optical Scan Unit



SolidWorks Student License
Academic Use Only

Figure A.30: Optical scan unit housing (3D).

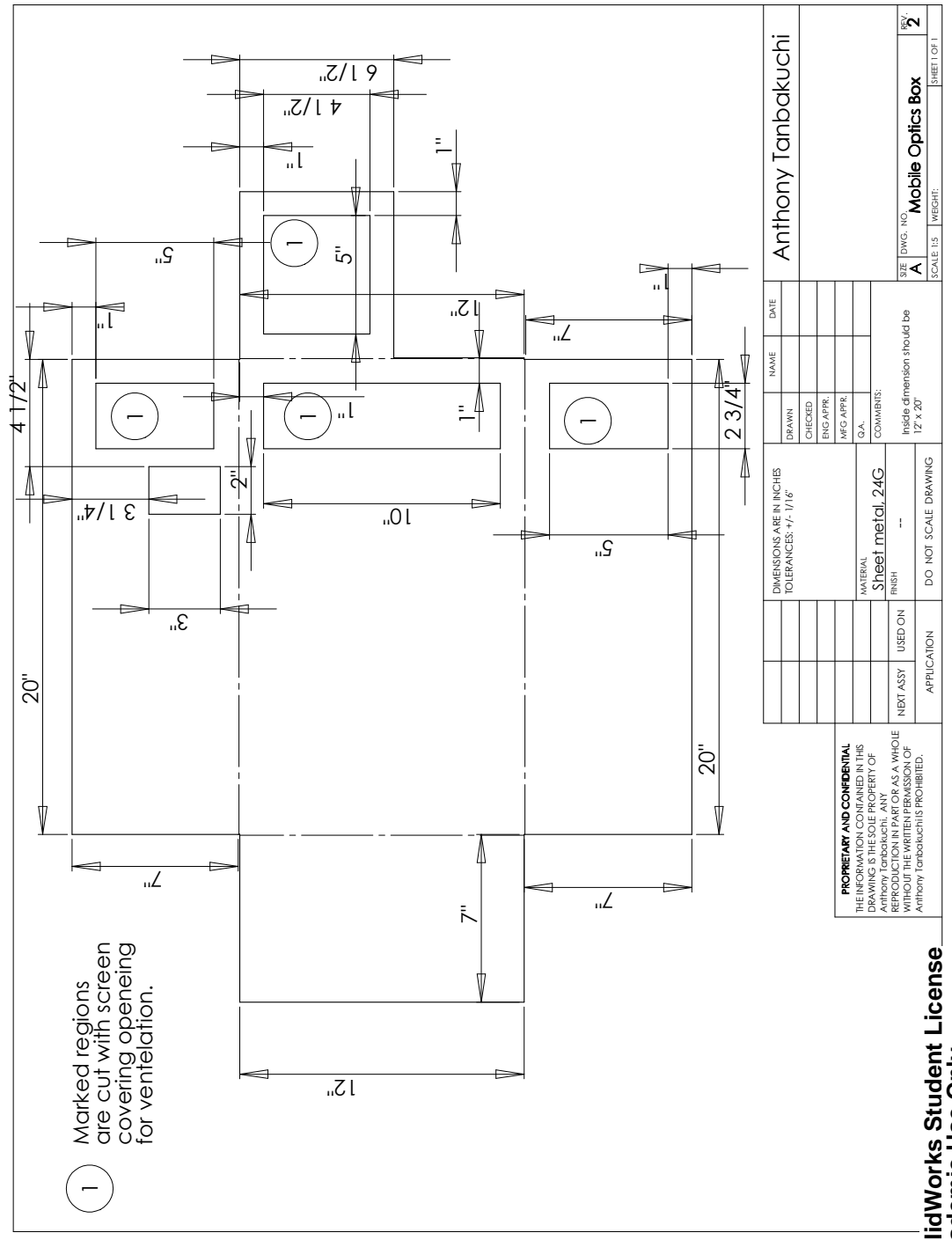


Figure A.31: Optical scan unit housing.

Real-time multi-spectral

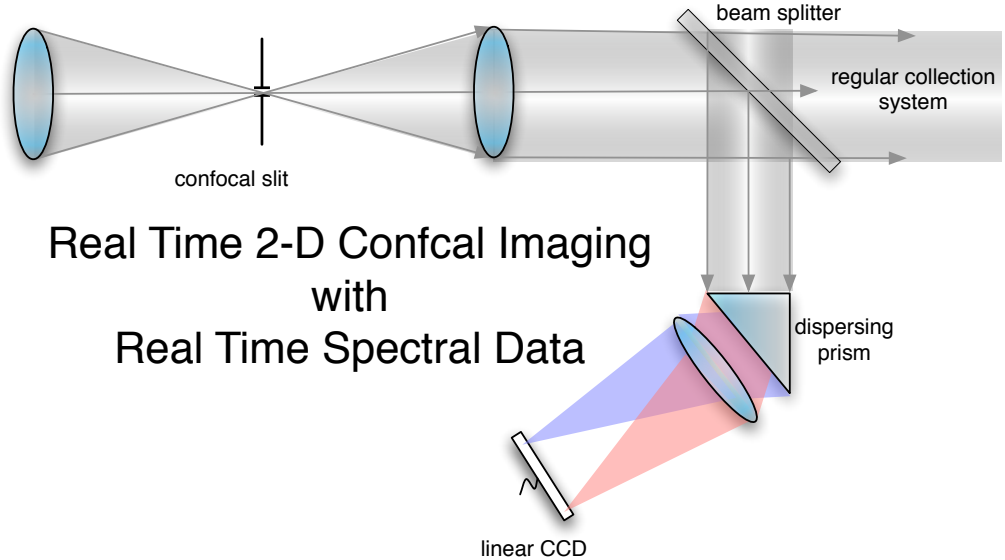


Figure A.32: Concept for real-time multi-spectral readout.

Appendix B

New miniature lens details

B.1 Lens data

10:26:11

DS303

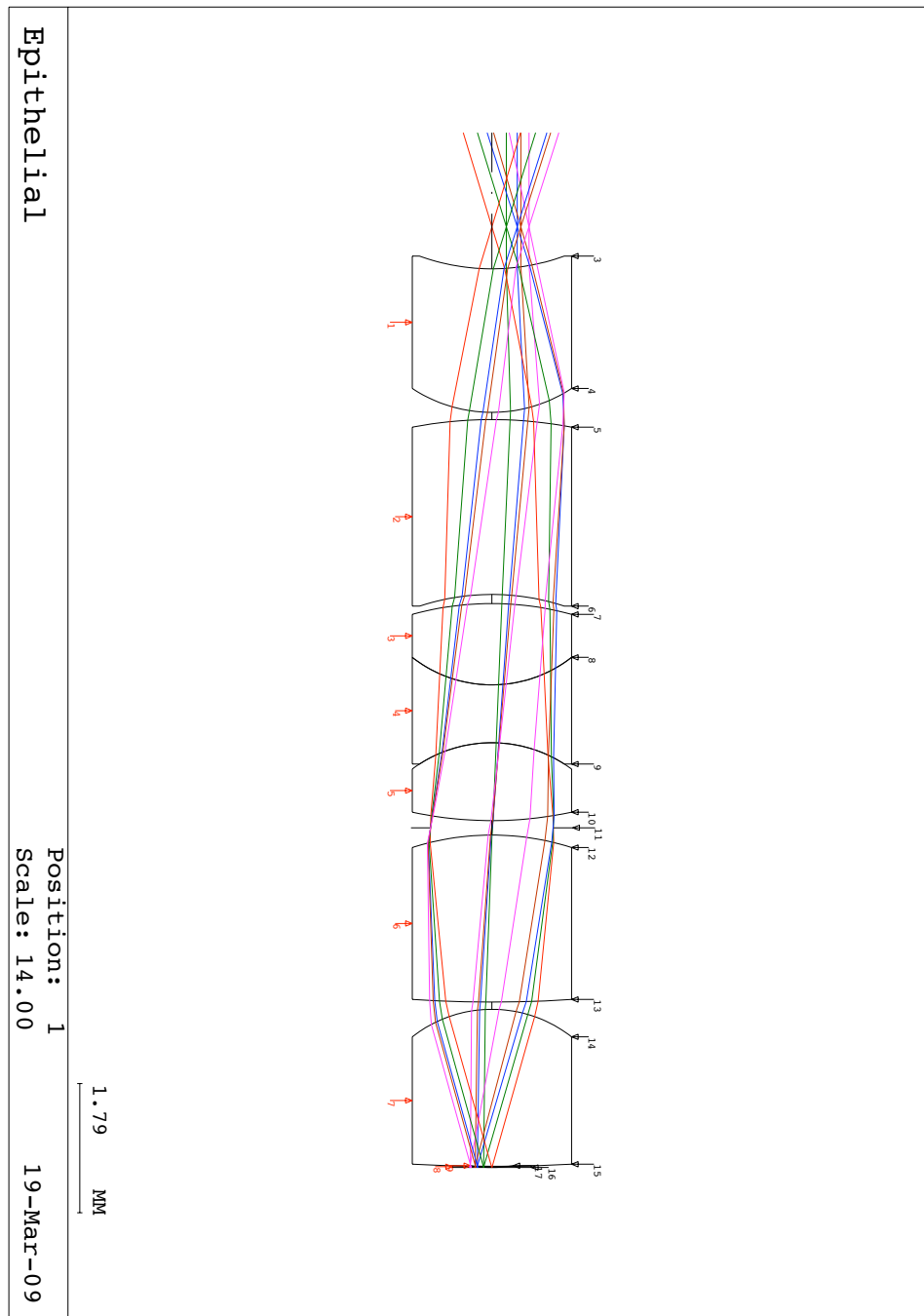


Figure B.1: Lens layout.

DS303

System data

		RDY	THI	RMD	GLA	CCY	THC	GLC
OBJ:	INFINITY	0.000000				100	100	
	SLB: "fiber"							
1:	INFINITY	0.414640				100	0	
	SLB: "focus space"							
2:	INFINITY	0.166050				100	100	
3:	-2.93000	1.983707		SF4_SCHOTT		100	100	
	SLB: "SF4-A"							
4:	-2.00000	0.100000				100	100	
5:	5.80000	2.416594		SF4_SCHOTT		100	100	
	SLB: "SF4-B"							
6:	3.17500	0.125830				100	100	
7:	4.11500	1.123592		NBF2_HOYA		100	100	
	SLB: "triplet-A"							
8:	-1.78200	0.800000		SF4_SCHOTT		100	100	
	SLB: "triplet-B"							
9:	1.84700	1.076034		NLAK22_SCHOTT		100	100	
	SLB: "triplet-C"							
10:	-5.25900	0.100000				100	100	
> STO:	INFINITY	0.100000				100	100	
12:	3.60100	2.308204		NLASF31A_SCHOTT		100	100	
	SLB: "SF31A-A"							
13:	-16.63100	0.100000				100	100	
14:	1.78200	2.170348		NLASF31A_SCHOTT		100	100	
	SLB: "SF31A-B"							
15:	-20.08800	0.015000		WATER_SPECIAL		100	100	
	SLB: "front face"							
16:	INFINITY	0.000000				100	100	
IMG:	-1.76016	0.000000				0	100	
SPECIFICATION DATA								
NAO	0.29000							
TEL								
DIM	MM							
WL	830.00	750.00	613.50	550.00	486.00			
REF	3							
WTW	1	1	1	1	1			
XOB	0.000000	0.000000	0.000000	0.000000	0.000000			
YOB	0.000000	0.200000	0.350000	0.400000	0.51250			
WTF	1.000000	1.000000	1.000000	1.000000	1.000000			
VUX	-0.00263	-0.00742	-0.01805	-0.02312	-0.03718			
VLX	-0.00263	-0.00742	-0.01805	-0.02312	-0.03718			
VUY	-0.00263	-0.00912	-0.03973	0.05799	0.31952			
VLY	-0.00263	-0.02450	-0.04512	-0.05076	-0.05726			
POL	N							
APERTURE DATA/EDGE DEFINITIONS								
CA APE								
CIR S1		0.512500						
CIR S2		0.660071						
CIR S3		1.000000						
CIR S4		1.000000						
CIR S5		1.000000						
CIR S6		1.000000						
CIR S7		1.000000						
CIR S8		1.000000						
CIR S9		1.000000						
CIR S10		1.000000						
CIR S11		0.847952						
CIR S12		1.000000						
CIR S13		1.000000						
CIR S14		1.000000						
CIR S15		0.345676						
CIR S16		0.314195						
CIR S1 EDG		0.612500						
CIR S2 EDG		0.760071						
CIR S3 EDG		1.100000						
CIR S4 EDG		1.100000						
CIR S5 EDG		1.100000						
CIR S6 EDG		1.100000						
CIR S7 EDG		1.100000						
CIR S8 EDG		1.100000						
CIR S9 EDG		1.100000						
CIR S10 EDG		1.100000						
CIR S11 EDG		1.117542						
CIR S12 EDG		1.100000						

Figure B.2: System data. (Page 1)

DS303

CIR S13	EDG	1.100000
CIR S14	EDG	1.100000
CIR S15	EDG	0.445676
CIR S16	EDG	0.545676

REFRACTIVE INDICES

GLASS CODE	830.00	750.00	613.50	550.00	486.00
WATER_SPECIAL	1.327712	1.329149	1.332270	1.334321	1.337136
NLASF31A_SCHOTT	1.866612	1.870413	1.880313	1.887609	1.898252
SF4_SCHOTT	1.735576	1.739969	1.751877	1.760983	1.774716
NBF2_HOYA	1.744678	1.747599	1.755015	1.760382	1.768113
NLAK22_SCHOTT	1.641936	1.644140	1.649666	1.653618	1.659263

No solves defined in system

No pickups defined in system

ZOOM DATA**ZOOM TITLE**

POS 1	"Epithelial"
POS 2	"50um"
POS 3	"150um"

	POS 1	POS 2	POS 3
VUY F1	-0.00263	-0.00435	-0.01116
VLY F1	-0.00263	-0.00435	-0.01116
VUY F2	-0.00912	-0.00575	-0.00072
VLY F2	-0.02450	-0.02810	-0.03840
VUY F3	-0.03973	-0.04238	-0.01962
VLY F3	-0.04512	-0.04821	-0.05500
VUY F4	0.05799	0.01010	-0.03397
VLY F4	-0.05076	-0.05319	-0.05714
VUY F5	0.31952	0.27508	0.11224
VLY F5	-0.05726	-0.05688	-0.03586
VUX F1	-0.00263	-0.00435	-0.01116
VLX F1	-0.00263	-0.00435	-0.01116
VUX F2	-0.00742	-0.00858	-0.01386
VLX F2	-0.00742	-0.00858	-0.01386
VUX F3	-0.01805	-0.01798	-0.01992
VLX F3	-0.01805	-0.01798	-0.01992
VUX F4	-0.02312	-0.02246	-0.02277
VLX F4	-0.02312	-0.02246	-0.02277
VUX F5	-0.03718	-0.03477	-0.03030
VLX F5	-0.03718	-0.03477	-0.03030
THI S1	0.41464	0.33264	0.10000
THC S1	0	0	0
THI S15	0.01500	0.05000	0.15000
THC S15	100	100	100
RDY S17	-1.76016	-1.85003	-2.04360
CCY S17	0	0	0

POS 1 POS 2 POS 3**INFINITE CONJUGATES**

EFL	10.0521	10.0521	10.0521
BFL	-5.7269	-5.7532	-5.8282
FFL	17.6431	17.5611	17.3284
FNO	0.0000	0.0000	0.0000

AT USED CONJUGATES

RED	0.5697	0.5724	0.5801
FNO	0.9823	0.9869	1.0002
OBJ DIS	0.0000	0.0000	0.0000
TT	13.0000	12.9530	12.8204
IMG DIS	0.0000	0.0000	0.0000
OAL	13.0000	12.9530	12.8204

PARAXIAL IMAGE

HT	0.2920	0.2934	0.2973
THI	0.0003	0.0008	0.0030
ANG	0.0000	0.0000	0.0000

ENTRANCE PUPIL

DIA	0.6060E+10	0.6060E+10	0.6060E+10
THI	0.1000E+11	0.1000E+11	0.1000E+11

EXIT PUPIL

DIA	6.0920	6.0920	6.0920
THI	-5.7269	-5.7532	-5.8282
STO DIA	1.6928	1.6934	1.6951

Figure B.3: System data. (Page 2)

DS303

Tolerance data

C E N T E R E D T O L E R A N C E S							POSITION 1		
Epithelial									
SUR	RADIUS	TOL	FRINGES	THICKNESS	TOL	GLASS	INDEX	V-NO	INHOMO-GENEITY
General: Loose			10.0		0.25			0.003	
General: Tight			3.0		0.025			0.0003	
Liebmann: Gen	0.005		4.0/ 0.25 wave		0.050				
whichever greater rad/fringes Liebmann									
0				0.00000					
1				0.41464					
2				0.16605					
3	-2.93000	0.0600	12.0/ 3.00	1.98371	0.04000	SF4	0.00200	0.80	
4	-2.00000	0.0200	4.0/ 1.00	0.10000	0.04000				
5	5.80000	0.0600	2.0/ 0.50	2.41659	0.06000	SF4	0.00200	0.80	
6	3.17500	0.0200	2.0/ 0.50	0.12583	0.02000				
7	4.11500	0.0400	2.0/ 0.50	1.12359	0.06000	NBF2	0.00200	0.80	
8	-1.78200	0.0600	12.0/ 3.00	0.80000	0.08000	SF4	0.00150	0.80	
9	1.84700	0.0200	12.0/ 3.00	1.07603	0.08000	NLAK22	0.00200	0.80	
10	-5.25900	0.0600	2.0/ 0.50	0.10000	0.10000				
11				0.10000	0.10000				
12	3.60100	0.0200	2.0/ 0.50	2.30820	0.04000	NLASF31A	0.00200	0.80	
13	-16.63100	0.7000	2.0/ 0.50	0.10000	0.02000				
14	1.78200	0.0200	2.0/ 0.50	2.17035	0.02000	NLASF31A	0.00200	0.80	
15	-20.08800	4.0000	12.0/ 3.00	0.01500	0.02000	WATER	0.00200	0.80	
16	INF		12.0/ 3.00	0.00000					
17	-1.76016			0.00000					

Radius, radius tolerance, thickness and thickness tolerance are given in mm.

Fringes of power and irregularity are at 546.1 nm. over the clear aperture

Irregularity is defined as fringes of cylinder power in test plate fit

T O L E R A N C E L I M I T S

	MINIMUM	MAXIMUM
* RADIUS	0.0200	
* SAG	0.0020	0.0500
** POWER	2.0	12.0
IRREGULARITY	0.50	3.00
THICKNESS	0.02000	0.50000
INDEX	0.00010	0.00200
V-NUMBER(%)	0.20	0.80

* Radius tolerance is determined by both radius and sag limits

** Power tolerance is between 2 and 4 times the irregularity tolerance

Figure B.4: Tolerance data. (Page 1)

DS303

13-Nov-08

POSITION 1

DECENTERED
TOLERANCES

Epithelial

ELEMENT NO.	FRONT RADIUS	BACK RADIUS	ELEMENT WEDGE		ELEMENT TILT		EL. DEC/ROLL(R)	
			TIR	ARC MIN	TIR	ARC MIN	TIR	mm.
General: Loose				3.0		3.0		0.1
General: Tight				0.5		0.3		0.01
Liebmman: Gen								
1	-2.93000	-2.00000	0.0040	6.9	0.0040	6.9	0.0063	0.0200
2	5.80000	3.17500	0.0020	3.4	0.0010	1.7	0.0057	0.0200
3	4.11500	-1.78200	0.0020	3.4			0.0260	0.0200 (R)
3- 4	4.11500	1.84700					0.0018	0.0200 (R)
3- 5	4.11500	-5.25900			0.0040	6.9	0.0173	0.0200
4	-1.78200	1.84700	0.0040	6.9				
5	1.84700	-5.25900	0.0040	6.9				
6	3.60100	-16.63100	0.0020	3.4	0.0010	1.7	0.0135	0.0200
7	1.78200	-20.08800	0.0020	9.9			0.0220	0.0200 (R)
7- 8	1.78200	INF			0.0016	8.6	0.0224	0.0200
8	-20.08800	INF	0.0020	10.9				

Radii are given in units of mm.

For wedge and tilt, TIR is a single indicator measurement taken at the smaller of the two clear apertures. For decenter and roll, TIR is a measurement of the induced wedge and is the maximum difference in readings between two indicators, one for each surface, with both surfaces measured at their respective clear apertures. The direction of measurement is parallel to the original optical axis of the element before the perturbation is applied. TIR is measured in mm.

Decenter or roll is measured perpendicular to the optical axis in mm.

TOLERANCE LIMITS

	MINIMUM	MAXIMUM
TIR	0.0020	0.1000
TILT	0.0003	0.0050
DECENTER	0.0200	0.5000
ROLL	0.0200	0.5000

X: 0.00000E+00 Y: 0.17603E-02

Figure B.5: Tolerance data. (Page 2)

DS303

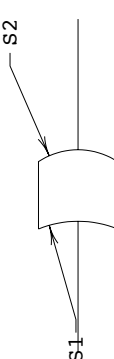
	RADIUS	RAD TOL	POW/IRR	C.A.	DIA	EDGE DIA	DIA TOL	CENTRAL THICKNESS	THI TOL	WEDGE	-
S1	2.930 CC	+0.0600	12 / 3.0		2.000						
S2	2.000 CX	+0.0200	4.0 / 1.0		2.000	2.200		1.984	+0.0400	0.0040	T.I.R.
NOTES :											
1. ALL DIMENSIONS ARE IN MILLIMETERS. 2. MATERIAL: OPTICAL GLASS PER MIL-G-174 TYPE: SF4 SCHOTT NO. 755276 NH 1.7552 ± 0.0020 V 27.6 ± 0.8% STRIAE GRADE , ANNEAL MELT NO. 3. 'P' FITCH POLISH TO TEST PLATE WITHIN POWER AND IREGULARITY INDICATED. 4. MANUFACTURE PER MIL-O-13830 5. SURFACE QUALITY 6. 'C' MAGNESIUM FLUORIDE COATING PER MIL-C-675 FOR MAX TRANSMISSION AT MILLIMICRONS. 7. 'G' FINE GROUND & BLACKENED PER 8. BEVEL EDGES AT 45 DEG TO MAX FACE WIDTH 9. DIAMETER TO FLAT IS (REF) WITH SURFACE SAG OF ON SURFACE S1											
											
Miniatue Objective ELEMENT 1						DR CHK APPD SCALE 7.01:1 REL BY REL DATE					

Figure B.6: Element 1 drawing.

10:40:05

DS303

184

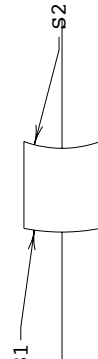
	RADIUS	RAD TOL	POW/IRR	C.A.	DIA	EDGE DIA	DIA TOL	CENTRAL THICKNESS	THI TOL	WEDGE	-
S1	5.800 CX	+0.0600	2.0 / .50		2.000						
S2	3.175 CC	+0.0200	2.0 / .50		2.000	2.200		2.417	+0.0600	0.0020	T.I.R.
NOTES :											
1. ALL DIMENSIONS ARE IN MILLIMETERS. 2. MATERIAL: OPTICAL GLASS PER MIL-G-174 TYPE: SF4 SCHOTT NO. 755276 NH 1.7552 ± 0.0020 V 27.6 ± 0.8% STRIAE GRADE , ANNEAL MELT NO. 3. 'P' FITCH POLISH TO TEST PLATE WITHIN POWER AND IREGULARITY INDICATED. 4. MANUFACTURE PER MIL-O-13830 5. SURFACE QUALITY 6. 'C' MAGNESIUM FLUORIDE COATING PER MIL-C-675 FOR MAX TRANSMISSION AT MILLIMICRONS. 7. 'G' FINE GROUND & BLACKENED PER 8. BEVEL EDGES AT 45 DEG TO MAX FACE WIDTH 9. DIAMETER TO FLAT IS (REF) WITH SURFACE SAG OF ON SURFACE S2											
											
Miniature Objective ELEMENT 2						DR CHK APPD SCALE 6.74 : 1 REL BY REL DATE - -					

Figure B.7: Element 2 drawing.

DS303

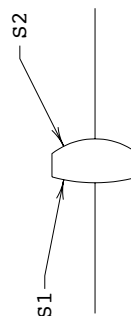
	RADIUS	RAD TOL	POW/IRR	C.A.	DIA	EDGE DIA	DIA TOL	CENTRAL THICKNESS	THI TOL	WEDGE	-
S1	4 .115 CX	+0 .0400	2 .0 / .50		2 .000						
S2	1 .782 CX	+0 .0600	12 / 3 .0		2 .000	2 .200		1 .124	+0 .0600	0 .0020	T.I.R.
NOTES :											
1. ALL DIMENSIONS ARE IN MILLIMETERS. 2. MATERIAL: OPTICAL GLASS PER MIL-G-174 TYPE: NBF2 HOYA NO. 757477 NH 1.7570 ± 0.0020 V 47.7 ± 0.8% STRIAE GRADE , ANNEAL MELT NO. 3. 'P' FITCH POLISH TO TEST PLATE WITHIN POWER AND IREGULARITY INDICATED. 4. MANUFACTURE PER MIL-O-13830 5. SURFACE QUALITY 6. 'C' MAGNESIUM FLUORIDE COATING PER MIL-C-675 FOR MAX TRANSMISSION AT MILLIMICRONS. 7. 'G' FINE GROUND & BLACKENED PER 8. BEVEL EDGES AT 45 DEG TO MAX FACE WIDTH											
											
Miniatue Objective ELEMENT 3						DR					
						CHK					
						APPD					
						SCALE 7.61:1	REL BY REL DATE				

Figure B.8: Element 3 drawing.

DS303

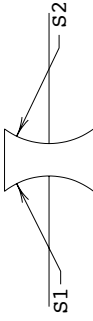
	RADIUS	RAD TOL	POW/IRR	C.A.	DIA	EDGE DIA	DIA TOL	CENTRAL THICKNESS	THI TOL	WEDGE	-
S1	1.782 CC	+0.0600	12 / 3.0		2.000						
S2	1.847 CC	+0.0200	12 / 3.0		2.000	2.200		0.800	+0.0800	0.0040	T.I.R.
NOTES :											
1. ALL DIMENSIONS ARE IN MILLIMETERS. 2. MATERIAL: OPTICAL GLASS PER MIL-G-174 TYPE: SF4 SCHOTT NO. 755276 NH 1.7552 ± 0.0015 V 27.6 ± 0.8% STRIAE GRADE , ANNEAL MELT NO. 3. 'P' FITCH POLISH TO TEST PLATE WITHIN POWER AND IREGULARITY INDICATED. 4. MANUFACTURE PER MIL-O-13830 5. SURFACE QUALITY 6. 'C' MAGNESIUM FLUORIDE COATING PER MIL-C-675 FOR MAX TRANSMISSION AT MILLIMICRONS. 7. 'G' FINE GROUND & BLACKENED PER 8. BEVEL EDGES AT 45 DEG TO MAX FACE WIDTH 9. DIAMETER TO FLAT IS (REF) WITH SURFACE SAG OF ON SURFACE S1 DIAMETER TO FLAT IS (REF) WITH SURFACE SAG OF ON SURFACE S2											
											
Miniature Objective ELEMENT 4						SCALE 7.86:1	REL BY REL DATE	-			
						DR					
						CHK					
						APPD					

Figure B.9: Element 4 drawing.

10:40:05

DS303

187

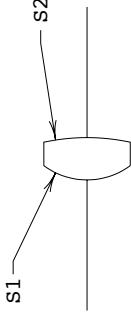
	RADIUS	RAD TOL	POW/IRR	C.A.	DIA	EDGE DIA	DIA TOL	CENTRAL THICKNESS	THI TOL	WEDGE	-
S1	1.847 CX	+0.0200	12 / 3.0		2.000						
S2	5.259 CX	+0.0600	2.0 / .50		2.000	2.200		1.076	+0.0800	0.0040	T.I.R.
NOTES :											
1. ALL DIMENSIONS ARE IN MILLIMETERS. 2. MATERIAL: OPTICAL GLASS PER MIL-G-174 TYPE: NLAK22 SCHOTT NO. 651559 NH 1.6511 ± 0.0020 V 55.9 ± 0.8% STRIAE GRADE , ANNEAL MELT NO. 3. 'P' FITCH POLISH TO TEST PLATE WITHIN POWER AND IREGULARITY INDICATED. 4. MANUFACTURE PER MIL-O-13830 5. SURFACE QUALITY 6. 'C' MAGNESIUM FLUORIDE COATING PER MIL-C-675 FOR MAX TRANSMISSION AT MILLIMICRONS. 7. 'G' FINE GROUND & BLACKENED PER 8. BEVEL EDGES AT 45 DEG TO MAX FACE WIDTH											
											
Miniatue Objective ELEMENT 5						DR					
						CHK					
						APPD					
						SCALE 7.65:1	REL BY REL DATE				

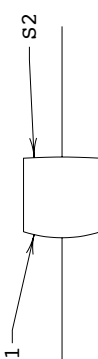
Figure B.10: Element 5 drawing.

DS303

	RADIUS	RAD TOL	POW/IRR	C.A.	DIA	EDGE DIA	DIA TOL	CENTRAL THICKNESS	THI TOL	WEDGE	
S1	3.601 CX	± 0.0200	2.0 / .50		2.000						-
S2	16.631 CX	± 0.7000	2.0 / .50		2.000	2.200		2.308	± 0.0400	0.0020	T.I.R.

NOTES :

1. ALL DIMENSIONS ARE IN MILLIMETERS.
2. MATERIAL: OPTICAL GLASS PER MIL-G-174
TYPE: NLASF31A SCHOTT NO. 883408
 N_h 1.8830 \pm 0.0020 V 40.8 \pm 0.8%
STRIKE GRADE ,
ANNEAL
MELT NO.
3. 'P' FITCH POLISH TO TEST PLATE WITHIN
POWER AND IREGULARITY INDICATED.
4. MANUFACTURE PER MIL-O-13830
5. SURFACE QUALITY
6. 'C' MAGNESIUM FLUORIDE COATING PER MIL-C-675
FOR MAX TRANSMISSION AT MILLIMICRONS.
7. 'G' FINE GROUND & BLACKENED PER
8. BEVEL EDGES AT 45 DEG TO MAX FACE WIDTH



	DR
	CHK
	APPD
Minature Objective	SCALE 6.80:1 REL BY REL DATE
ELEMENT 6	-

Figure B.11: Element 6 drawing.

DS303

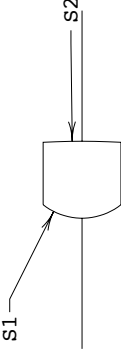
	RADIUS	RAD TOL	POW/IRR	C.A.	DIA	EDGE DIA	DIA TOL	CENTRAL THICKNESS	THI TOL	WEDGE	-										
S1	1.782 CX	+0.0200	2.0 / .50		2.000																
S2	20.088 CX	+4.0000	12 / 3.0		0.691	2.200		2.170	+0.0200	0.0020	T.I.R.										
NOTES :																					
1. ALL DIMENSIONS ARE IN MILLIMETERS. 2. MATERIAL: OPTICAL GLASS PER MIL-G-174 TYPE: NLASF31A SCHOTT NO. 883408 NH 1.8830 ± 0.0020 V 40.8 ± 0.8% STRIAE GRADE , ANNEAL MELT NO. 3. 'P' FITCH POLISH TO TEST PLATE WITHIN POWER AND IREGULARITY INDICATED. 4. MANUFACTURE PER MIL-O-13830 5. SURFACE QUALITY 6. 'C' MAGNESIUM FLUORIDE COATING PER MIL-C-675 FOR MAX TRANSMISSION AT MILLIMICRONS. 7. 'G' FINE GROUND & BLACKENED PER 8. BEVEL EDGES AT 45 DEG TO MAX FACE WIDTH																					
																					
<table border="1"> <tr> <td></td> <td>DR</td> </tr> <tr> <td></td> <td>CHK</td> </tr> <tr> <td></td> <td>APPD</td> </tr> <tr> <td>Scale</td> <td>REL BY REL DATE</td> </tr> <tr> <td>6.89:1</td> <td></td> </tr> </table>													DR		CHK		APPD	Scale	REL BY REL DATE	6.89:1	
	DR																				
	CHK																				
	APPD																				
Scale	REL BY REL DATE																				
6.89:1																					
<table border="1"> <tr> <td>Miniature Objective</td> <td></td> </tr> <tr> <td>ELEMENT 7</td> <td></td> </tr> <tr> <td></td> <td>-</td> </tr> </table>												Miniature Objective		ELEMENT 7			-				
Miniature Objective																					
ELEMENT 7																					
	-																				

Figure B.12: Element 7 drawing.

B.2 Lens quotation

The following is a quotation for a preliminary version of the final design.

From: "Robert Bush" <Robert.Bush@Liebmann.com>
To: "Anthony Tanbakuchi" <anthony.tanbakuchi@gmail.com>
Cc: "Beth Saunders" <BSaunders@Liebmann.com>, "Glenn Gilbert"
<GGilbert@Liebmann.com>, "Jay Kumler \Coastal Optical Systems'"
<Jay.Kumler@coastalopt.com>

Quote Number 1724-RRL (estimate)

June 22, 2007

Hi Anthony,

I sent the Zemax file (I do not have Zemax here) down to our sister company - Coastal Optical Systems Inc in West Palm Beach FL. They were exhibiting right beside us at the trade show in Rochester. Jay Kumler has reviewed the design and sent me back the pages in word that I typically need to quote - Radii, CT's, tolerances. Coastal and Liebmann work nearly seamlessly together on many projects.

From the design side: Coastal reviewed the design and had the following observation.

The design is well corrected.

From the manufacturing side: I have reviewed the layout and have the following observations.

1. The lens size is not a problem for us. We make hundreds of lenses these sizes or smaller every month for use in endoscopes.
2. You are correct that the little meniscus lens will be the toughest, but this is what we do. We are confident we can manufacture these lenses.
3. We are making some assumptions:

- a. CT tolerances of .050 or larger;
- b. Radius tolerances of 4 fringes or .005mm, whichever is larger;
- c. Irregularity of BC wave or looser;
- d. Diameter tolerances of +0.000, -0.025;
- e. Sag tolerances (if needed) of +/- .025mm.

4. Please be careful when reviewing the centering specs. These are

Figure B.13: Lens quotation. (Page 1)

small lenses and even small TIR measurements can be quite large angular measurements. Try to keep the TIR of the lenses at .005mm or larger.
5. For good manufacturing practice, lenses should have chamfers when possible. It may not be possible here due to your size constraints, but try to allow room for a .050mm bevel at 45 degrees.

I am checking on the metal housing availability. There are companies out there that specialize in these small diameters.

From a budget point of view, Jay has given me some estimates if you would like Coastal to review the design.

From the manufacturing side. For Liebmann to produce 6 sets of lenses, the cost would be ~\$23K - \$27K.

You still need to add the cost of the housing and any other metal parts (spacers, retainers). Do you need us to quote the optical assembly or testing of the assembly? Hopefully this gets you the information you need for budgeting.

Please let me know if you have any questions. I would suggest you take a look at the Coastal Website. This type of work (lens design, manufacture and test) is right up their alley. The size of the components fits Liebmann very well. Together, I think we can offer a way to a good solution for your application.

Best regards,

Bob Bush

Liebmann Optical Company

413-527-0079, ext 150

Robert.Bush@Liebmann.com

Figure B.14: Lens quotation. (Page 2)

B.3 Additional Designs

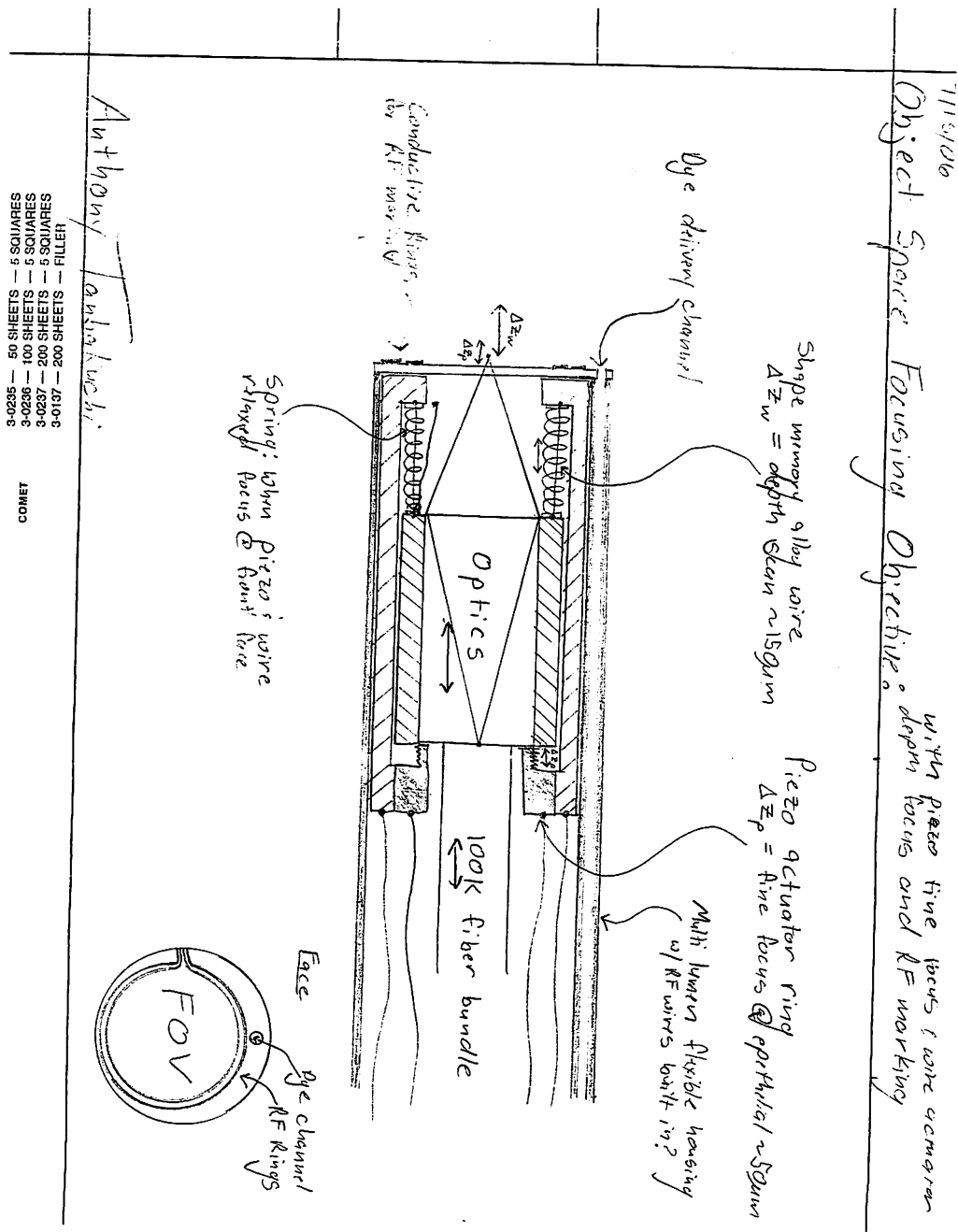


Figure B.15: Alternative objective space focus. Front element contains conductive rings to mark tissue site using RF ablation.

Appendix C

Clinical software

The confocal microlaparoscope clinical software called LiveHistology was written in Objective-C using Cocoa for the user interface on Mac OS X Leopard (10.5). The software was developed using Xcode and Interface Builder, both provided with OS X.

Since the program is multi-threaded and I encountered problems using the QuickTime libraries to encoding the live videos in a multi-threaded environment, a small helper application called ImageMovie was also created. The clinical software writes a movie file (just a package with the individual movie frames). Once you click on the movie file, the ImageMovie program automatically re-encodes the movie to a quicktime movie and deletes the original movie package. Originally the program was not multi-threaded and the videos could be directly encoded. Ultimately the QuickTime bug should be fixed (probably in OS X 10.6 since the QT library will likely be dramatically overhauled) and then the program can go back to using to directly encode the videos using the QuickTime library.

C.1 Dependencies

The following is a list of dependencies the program has outside of the standard OS X libraries.

PVCAM Library Interfaces with our CCD cameras. [PVCAM Website](#)

Note: you can't always get the newest Mac version from their website.

NI VISA Library Interfaces with our function generator. The Virtual Instrument Software Architecture (VISA) is a standard for configuring, programming, and troubleshooting instrumentation systems comprising GPIB, VXI, PXI, Serial, Ethernet, and/or USB interfaces. [NI VISA Website](#)

BGHUDAppKit Additional user interface elements used in the software (primarily the image processing and log windows.) You must compile the XCode project then double click on the *BGHUDAppKitPlugin.ibplugin* in the build directory to add the new elements to Interface Builder. [BGHUD Info](#) and [BGHUD Google Code Site](#)

C.2 Classes

The following is a list of the classes inside the program.

Main program

SciCamController This is the main program class. Once the user interface is loaded the entrance into the program is the *awakeFromNib* method. All of the main program functions and objects are inside this class.

Image processing, encoding, and display

AATvImagePool This class efficiently manages the memory for the *AATvImage* object. The *AATvImage* objects store the image data and can perform efficient image processing operations in real-time. Only one instance of this class is ever created and it's method *getvImageWithWidth...* returns a new *AATvImage*. This class has been designed to allow use of Objective-C Garbage collection while efficiently managing memory for images. Use this for all image data.

AATvImage A class representing an image. It has a pointer to the raw data (*(void) dataBuffer*) as well as additional typed pointers pointing to the raw data for 8-bit (*UInt8DataBuffer*), 16-bit (*unsignedShortDataBuffer*), and floating point (*floatDataBuffer*) formats. It stores the properties basic properties and contains many optimized methods for finding image statistis and performing image processing operations. Add new image processing methods to this class. Don't directly create a *AATvImage*, get a new image using *AATvImagePool*'s *getvImageWithWidth...* method.

AATMovieWriter Used to encode the live videos.

AATAutoFocusAnalysis Analyzes a sequence of images to find the best focus.

MyOpenGLImageView Used to display the live images in the *high quality* mode. The software also can display the images directly using *NSImageView*.

AATZScanSlice Just a set of *AATVimages* collected during an axial z-scan.

Hardware interface

AATCameraProtocol Defines the basic functions a camera class must implement. This generalizes the cameras so we can later use other types of cameras. It also allows the ability to easily use a simulated camera to test the program when no physical camera is available.

PVCamController Conforms to the *AATCameraProtocol* and allows the use of PVCAM based cameras (from Photometrics, Roper Scientific and Princeton Instruments). Our two CCD cameras are controlled with this class. Requires the PVCAM library to be installed.

AATSimulatedCamera Conforms to the *AATCameraProtocol* and implements a simulated camera that generates data for the program when no real camera is available.

FunctionGenerator Controls the function generator using the National Instruments NI VISA library. Requires the NI VISA library to be installed. Houssine helped develop this class.

hidjoystick Used to interface with the buttons on the microlaparoscope handle. The buttons are wired to a USB HID joystick chip. The HID (Human Interface Device) library is used to interact with the chip.

joystickEvent For individual events from a joystick chip. Used by *hidjoy-stick*, don't use this directly.

proXRcontroller Not used anymore. Old system used a Pro-XR controller to control the piezo valve in the second generation microlaparoscope. The Pro-XR device contains relay switches that are controlled via a serial interface.

AATSerialPort Connects to serial ports and performs low level communication.

AATZaberController Connects to and controls the motors inside the microlaparoscope. The motors control focus and dye delivery. Utilizes *AATSerialPort* for low level serial communication to the motors. The motors are connected to the system using a serial to USB connector.

AATZaberMotor Defines all the functions and properties for the motors. Don't directly use this, get a motor from the *AATZaberController*.

Appendix D

Bare fibers

The bare fibers with contoured tips discussed in Chapter 6 were developed using the polishing configuration shown in figure D.1. A flat tipped bare fiber was placed into contact with fiber polishing paper. The polishing paper spins along the z axis. Concurrently, the fiber is pivoted in the y - z plane and rotated along its optical axis (z'). The combined motion of the fiber and the polishing paper shapes the flat tipped fiber into a hemisphere tip. A cone tipped fiber can be generated by omitting the pivoting movement of the fiber.

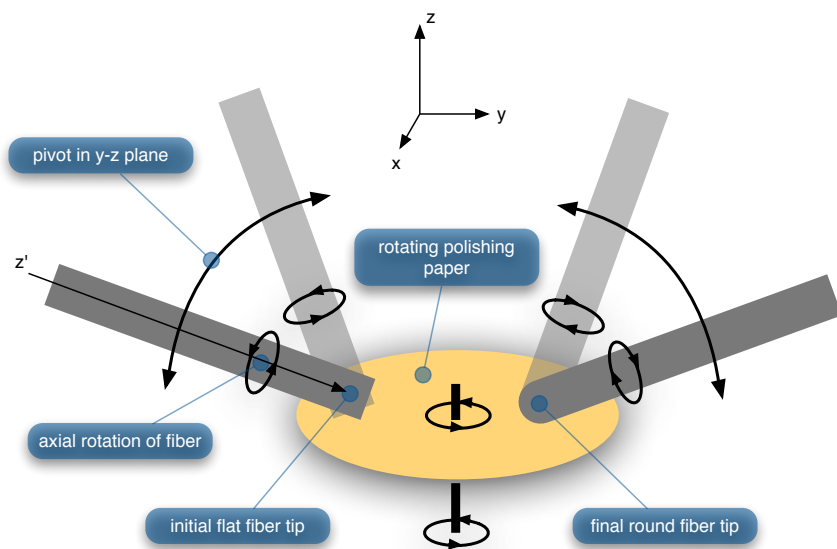


Figure D.1: Method for manufacturing contoured fiber tips.

Appendix E

Citation Index

CITATION INDEX

- Adler and Murdoch [85], 94
- Blanca and Saloma [63], 74, 79, 91
- Boudoux et al. [22], 23
- Bowrey and Peters [52], 51
- Calle et al. [13], 22
- Carr et al. [86], 94
- Chen et al. [41], 23
- Cheong et al. [83], 93
- Claus et al. [12], 22
- Corle and Kino [60], 74, 77, 93, 104
- Crilly et al. [70], 78
- Freeberg et al. [35], 23
- Frieden [76], 83
- Galassi et al. [74], 82
- Garcia et al. [8], 21
- Giovanelli [81], 91
- Gmitro and Aziz [2], 19, 23, 24, 32, 58
- Haka et al. [33], 23
- Hallowell [19], 23
- Heney and Greenstein [77], 87
- Jacques et al. [78], 87
- Jean et al. [27], 23
- Kerlikowske et al. [15], 22
- Kiesslich et al. [57], 64
- Kleinsmith [1], 18
- Knittel et al. [28], 23
- Konig et al. [29], 23
- Kramer et al. [17], 22, 50
- Kusuzaki et al. [56], 63
- L'Ecuyer [75], 83
- Lam et al. [42], 23
- Lange and Boyd [53], 52
- Liebert et al. [68], 78
- Lin and Webb [26], 23
- Magnor et al. [62], 74
- Makhlof et al. [3], 19, 37
- Makhlof et al. [51], 34, 37, 58
- Mayes et al. [36], 23

- Metropolis and Ulam [64], 78
 Modan et al. [14], 22
 Mori et al. [11], 22
 Morykwas et al. [54], 52
 Motz et al. [34], 23
 Mustonen et al. [59], 73
 Nakao et al. [23], 23
 National Cancer Institute [9], 21
 Polglase et al. [21], 23
 Prahл et al. [67], 78
 R Development Core Team [82], 92
 Richards-Kortum et al. [31], 23
 Risch et al. [10], 22
 Rocca et al. [18], 22
 Rouse and Gmitro [5], 19, 24, 32, 37,
 43, 58
 Rouse et al. [50], 32, 58
 Rouse et al. [6], 19, 24, 32, 40, 43, 58,
 112
 Sabharwal et al. [4], 19, 24, 32, 58
 Schmitt and Ben-Letaiet [69], 78
 Schmitt et al. [73], 79
 Schwarz et al. [88], 125
 Shin et al. [25], 23
 Srivastava et al. [55], 54, 63
 Stratton et al. [16], 22
 Swartling et al. [71], 78
 Tanbakuchi et al. [44], 24, 58, 62, 73,
 92
 Tanbakuchi et al. [45], 28
 Tanbakuchi et al. [46], 29
 Tanbakuchi et al. [47], 32, 58
 Tanbakuchi et al. [49], 32, 43, 58
 Tearney et al. [38], 23
 Testoni and Mangiavillano [43], 23
 Tumlinson et al. [37], 23
 Udovich et al. [48], 32, 51, 58
 Udovich et al. [58], 64
 Utzinger and Richards-Kortum [32], 23
 Vo-Dinh et al. [84], 93
 Wang et al. [20], 23
 Wang et al. [40], 23
 Wang et al. [65], 78
 Welch and van Gemert [79], 91
 Welch et al. [72], 79
 Wilder-Smith et al. [39], 23
 Wilson and Adam [66], 78
 Wilson and Jacques [87], 108, 109
 Wilson [61], 74, 79
 Yang et al. [24], 23
 Zhuo et al. [30], 23
 Zucker [7], 19

van de Hulst [80], 91

Appendix F

Colophon

This dissertation was typeset using the L^AT_EX typesetting system created by Leslie Lamport and the Memoir class written by Peter Wilson. The body text is Computer Modern Roman designed by Donald Knuth. Other fonts include Sans, Smallcaps, Italic, and Slanted, all from Knuth's Computer Modern family. The optical design was carried out in Code V, data analysis was done using R, mechanical design was accomplished with SolidWorks, and most of the figures were created with OmniGraffle.

REFERENCES

REFERENCES

- [1] Lewis J Kleinsmith. *Principles of cancer biology*. Pearson Benjamin Cummings, San Francisco, 2006. ISBN 0805340033. URL <http://www.loc.gov/catdir/toc/ecip0511/2005010378.html>.
- [2] Arthur F. Gmitro and David Aziz. Confocal microscopy through a fiber-optic imaging bundle. *Optics Letters*, 18(1), November 1993.
- [3] Houssine Makhlof, Arthur F Gmitro, Anthony A Tanbakuchi, Josh A Udovich, and Andrew R Rouse. Multispectral confocal microendoscope for in vivo and in situ imaging. *J Biomed Opt*, 13(4):044016, 2008 Jul-Aug. ISSN 1083-3668 (Print). doi: 10.1117/1.2950313.
- [4] Yashvinder S. Sabharwal, Andrew R. Rouse, LaTanya Donaldson, Mark F. Hopkins, and Arthur F. Gmitro. Slit-scanning confocal microendoscope for high-resolution in vivo imaging. *Applied Optics*, 38(34):7133–7144, December 1999.
- [5] Andrew R. Rouse and Arthur F. Gmitro. Multispectral imaging with a confocal microendoscope. *Optics Letters*, 25(23), 2000.
- [6] Andrew R. Rouse, Angelique Kano, Joshua A. Udovich, Shona M. Kroto, and Arthur F. Gmitro. Design and demonstration of a miniature catheter for a confocal microendoscope. *Applied Optics*, 43(31):5763–5771, November 2004.

- [7] Karl A. Zucker, editor. *Surgical Laparoscopy*. Quality medical publishing, 1991.
- [8] M. Garcia, A. Jemal, E. M. Ward, M. M. Center, Y Hao, R. L. Siegel, and M. J. Thun. *Global Cancer Facts & Figures*. American Cancer Society, Atlanta, GA, 2007. URL http://www.cancer.org/downloads/STT/Global_Cancer_Facts_and_Figures_2007_rev.pdf.
- [9] National Cancer Institute. NCI issues clinical announcement for preferred method of treatment for advanced ovarian cancer. <http://www.cancer.gov/newscenter/pressreleases/IPchemotherapyrelease>, January 2006.
- [10] H.A. Risch, L.D. Marrett, M. Jain, and G.R. Howe. Differences in Risk Factors for Epithelial Ovarian Cancer by Histologic Type Results of a Case-Control Study, 1996.
- [11] M. Mori, I. Harabuchi, H. Miyake, J.T. Casagrande, B.E. Henderson, and R.K. Ross. Reproductive, genetic, and dietary risk factors for ovarian cancer. *American Journal of Epidemiology*, 128(4):771–777, 1988.
- [12] EB Claus, JM Schildkraut, WD Thompson, and NJ Risch. The genetic attributable risk of breast and ovarian cancer. *Cancer*, 77(11):2318–24, 1996.
- [13] E.E. Calle, C. Rodriguez, K. Walker-Thurmond, and M.J. Thun. Overweight, Obesity, and Mortality from Cancer in a Prospectively Studied Cohort of US Adults, 2003.
- [14] B. Modan, E. Ron, L. Lerner-Geva, T. Blumstein, J. Menczer, J. Rabinovici, G. Oelsner, L. Freedman, S. Mashiach, and B. Lunenfeld. Cancer Incidence in a Cohort of Infertile Woman. *American Journal of Epidemiology*, 147(11):1038–1042, 1998.

- [15] K. Kerlikowske, J. S. Brown, and D. G. Grady. Should women with familial ovarian cancer undergo prophylactic oophorectomy. *Obstetrics and Gynecology*, 80(4):700–707, 1992.
- [16] J. F. Stratton, P. Pharoah, S. K. Smith, D. Easton, and B.A. Ponder. A systematic review and meta-analysis of family history and risk of ovarian cancer. *British Journal of Obstetrics and Gynecology*, 105(5):493–499, 1998.
- [17] B. S. Kramer, J. Gohagan, and P. C. Prorok. NIH consensus 1994: screening. *Gynecologic Oncology*, 55(3):20–21, 1994.
- [18] W.A. Rocca, B.R. Grossardt, M. de Andrade, G.D. Malkasian, and L.J. Melton. Survival patterns after oophorectomy in premenopausal women: a population-based cohort study. *Lancet Oncology*, 7(10):821–828, 2006.
- [19] N. Hallowell. A qualitative study of the information needs of high-risk women undergoing prophylactic oophorectomy. *Psycho-Oncology*, 9(6):486–495, 2000.
- [20] T.D. Wang, M.J. Mandella, C.H. Contag, G.S. Kino, et al. Dual-axis confocal microscope for high-resolution *in vivo* imaging. *Optics Letters*, 28(6):414–416, 2003.
- [21] A.L. Polglase, W.J. McLaren, S.A. Skinner, R. Kiesslich, M.F. Neurath, and P.M. Delaney. A fluorescence confocal endomicroscope for *in vivo* microscopy of the upper-and the lower-GI tract. *Gastrointestinal Endoscopy*, 62(5):686–695, 2005.
- [22] C. Boudoux, S. Yun, W. Oh, W. White, N. Iftimia, M. Shishkov, B. Bouma, and G. Tearney. Rapid wavelength-swept spectrally encoded confocal microscopy. *Optics Express*, 13(20):8214–8221, 2005.

- [23] Madoka Nakao, Shigeto Yoshida, Shinji Tanaka, Yoshito Takemura, Shiro Oka, Masaharu Yoshihara, and Kazuaki Chayama. Optical biopsy of early gastroesophageal cancer by catheter-based reflectance-type laser-scanning confocal microscopy. *J Biomed Opt*, 13(5):054043, 2008 Sep-Oct. ISSN 1083-3668 (Print). doi: 10.1117/1.2983674.
- [24] L. Yang, A.M. Raighne, E.M. McCabe, L.A. Dunbar, and T. Scharf. Confocal microscopy using variable-focal-length microlenses and an optical fiber bundle. *Applied Optics*, 44(28):5928–5936, 2005.
- [25] H.J. Shin, M.C. Pierce, D. Lee, H. Ra, O. Solgaard, and R. Richards-Kortum. Fiber-optic confocal microscope using a MEMS scanner and miniature objective lens. *Optics Express*, 15(15):9113–9122, 2007.
- [26] C.P. Lin and R.H. Webb. Fiber-coupled multiplexed confocal microscope, April 22 2004. US Patent App. 10/830,905.
- [27] F. Jean, G. Bourg-Heckly, and B. Viellerobe. Fibered confocal spectroscopy and multicolor imaging system for in vivo fluorescence analysis. *Optics Express*, 15 (7):4008–4017, 2007.
- [28] J. Knittel, L. Schnieder, G. Buess, B. Messerschmidt, and T. Possner. Endoscope-compatible confocal microscope using a gradient index-lens system. *Optics Communications*, 188(5-6):267–273, 2001.
- [29] K. Konig, A. Ehlers, I. Riemann, S. Schenkl, R. Buckle, and M. Kaatz. Clinical two-photon microendoscopy. *Microsc Res Tech*, 70(5):398–402, 2007 May. ISSN 1059-910X (Print). doi: 10.1002/jemt.20445.
- [30] S Zhuo, J Chen, T Luo, X Jiang, S Xie, and R Chen. Two-layered multiphoton microscopic imaging of cervical tissue. *Lasers Med Sci*, (2008), 2008.

- [31] R. Richards-Kortum, N. Ramanujam, A. Mahadevan-Jansen, M. Follen, and U. Utzinger. Method for probabilistically classifying tissue in vitro and in vivo using fluorescence spectroscopy, June 26 2007. US Patent 7,236,815.
- [32] U. Utzinger and R.R. Richards-Kortum. Fiber optic probes for biomedical optical spectroscopy. *Journal of Biomedical Optics*, 8:121, 2003.
- [33] Abigail S. Haka, Karen E. Shafer-Peltier, Maryann Fitzmaurice, Joseph Crowe, Ramachandra R. Dasari, and Michael S. Feld. Diagnosing breast cancer by using raman spectroscopy. *Proc Natl Acad Sci USA*, 102(35):12371–12376, 2005 Aug 30. ISSN 0027-8424 (Print). doi: 10.1073/pnas.0501390102.
- [34] Jason T. Motz, Saumil J. Gandhi, Obrad R. Scepanovic, Abigail S. Haka, John R. Kramer, Ramachandra R. Dasari, and Michael S. Feld. Real-time raman system for in vivo disease diagnosis. *J Biomed Opt*, 10(3):031113, 2005 May-Jun. ISSN 1083-3668 (Print). doi: 10.1117/1.1920247.
- [35] J Adrian Freeberg, J L Benedet, Calum MacAulay, Loyd A West, and Michele Follen. The performance of fluorescence and reflectance spectroscopy for the in vivo diagnosis of cervical neoplasia; point probe versus multispectral approaches. *Gynecol Oncol*, 107(1 Suppl 1):S248–55, 2007 Oct. ISSN 0090-8258 (Print). doi: 10.1016/j.ygyno.2007.07.008.
- [36] Patrick Mayes, David Dicker, Yingqiu Liu, and Wafik El-Deiry. Noninvasive vascular imaging in fluorescent tumors using multispectral unmixing. *Biotechniques*, 45(4):459–460, 2008 Oct. ISSN 0736-6205 (Print). doi: 10.2144/000112946.
- [37] A.R. Tumlinson, J.K. Barton, B. Považay, H. Sattman, A. Unterhuber, R.A. Leitgeb, and W. Drexler. Endoscope-tip interferometer for ultrahigh resolution

- frequency domain optical coherence tomography in mouse colon. *Optics Express*, 14(5):1878–1887, 2006.
- [38] G.J. Tearney, S.A. Boppart, B.E. Bouma, M.E. Brezinski, N.J. Weissman, J.F. Southern, and J.G. Fujimoto. Scanning single-mode fiber optic catheter-endoscope for optical coherence tomography. *SPIE MILESTONE SERIES MS*, 147:656–658, 1998.
- [39] Petra Wilder-Smith, Woong-Gyu Jung, Matthew Brenner, Kathryn Osann, Hamza Beydoun, Diana Messadi, and Zhongping Chen. In vivo optical coherence tomography for the diagnosis of oral malignancy. *Lasers Surg Med*, 35(4): 269–275, 2004. ISSN 0196-8092 (Print). doi: 10.1002/lsm.20098.
- [40] Z.G. Wang, C. Lee, W. Waltzer, Z.J. Yuan, Z.L. Wu, H.K. Xie, and Y.T. Pan. Optical coherence tomography for noninvasive diagnosis of epithelial cancers. *Conf Proc IEEE Eng Med Biol Soc*, 1:129–132, 2006. ISSN 1557-170X (Print). doi: 10.1109/IEMBS.2006.259452.
- [41] Y. Chen, A.D. Aguirre, P.L. Hsiung, S. Desai, P.R. Herz, M. Pedrosa, Q. Huang, M. Figueiredo, S.W. Huang, A. Koski, J.M. Schmitt, J.G. Fujimoto, and H. Mashimo. Ultrahigh resolution optical coherence tomography of barrett's esophagus: preliminary descriptive clinical study correlating images with histology. *Endoscopy*, 39(7):599–605, 2007 Jul. ISSN 1438-8812 (Electronic). doi: 10.1055/s-2007-966648.
- [42] Stephen Lam, Beau Standish, Corisande Baldwin, Annette McWilliams, Jean leRiche, Adi Gazdar, Alex I. Vitkin, Victor Yang, Norihiko Ikeda, and Calum MacAulay. In vivo optical coherence tomography imaging of preinvasive

- bronchial lesions. *Clin Cancer Res*, 14(7):2006–2011, 2008 Apr 1. ISSN 1078-0432 (Print). doi: 10.1158/1078-0432.CCR-07-4418.
- [43] Pier-Alberto Testoni and Benedetto Mangiavillano. Optical coherence tomography in detection of dysplasia and cancer of the gastrointestinal tract and biliary-pancreatic ductal system. *World J Gastroenterol*, 14(42):6444–6452, 2008 Nov 14. ISSN 1007-9327 (Print).
- [44] Anthony A. Tanbakuchi, Andrew R. Rouse, Josh A. Udovich, Kenneth D. Hatch, and Arthur F. Gmitro. A clinical confocal microlaparoscope for real-time in vivo optical biopsies. Submitted to the Journal of Biomedical Optics, February 2009.
- [45] Anthony A. Tanbakuchi, Andrew R. Rouse, Josh A. Udovich, Kenneth D. Hatch, and Arthur F. Gmitro. *In vivo* imaging of ovarian tissue using a novel confocal microlaparoscope. Submitted to the American Journal of Obstetrics and Gynecology, March 2009.
- [46] Anthony A. Tanbakuchi, Andrew R. Rouse, and Arthur F. Gmitro. Monte carlo characterization of parallelized fluorescence confocal systems imaging in turbid media. Submitted to the Journal of Biomedical Optics, April 2009.
- [47] A.A. Tanbakuchi, A.R. Rouse, K.D. Hatch, R.E. Sampliner, J.A. Udovich, and A.F. Gmitro. Clinical evaluation of a confocal microendoscope system for imaging the ovary. In *Endoscopic Microscopy III*. Edited by Tearney, Guillermo J.; Wang, Thomas D. *Proceedings of the SPIE*, volume 6851, pages 685103–685103, 2008.
- [48] Joshua A. Udovich, Andrew R. Rouse, Anthony Tanbakuchi, Molly A. Brewer, Richard Sampliner, and Arthur F. Gmitro. Confocal micro-endoscope for use in a

- clinical setting. volume 6432, page 64320H. SPIE, 2007. doi: 10.1117/12.701798.
URL <http://link.aip.org/link/?PSI/6432/64320H/1>.
- [49] Anthony A. Tanbakuchi, Andrew R. Rouse, Josh A. Udovich, and Arthur F. Gmitro. Surgical imaging catheter for confocal microendoscopy with advanced contrast delivery and focus systems. volume 6082, page 608202. SPIE, 2006. doi: 10.1117/12.644812. URL <http://link.aip.org/link/?PSI/6082/608202/1>.
- [50] Andrew R. Rouse, Anthony A. Tanbakuchi, Joshua A. Udovich, and Arthur F. Gmitro. Design of an in vivo multi-spectral confocal microendoscope for clinical trials. volume 6082, page 608205. SPIE, 2006. doi: 10.1117/12.646913. URL <http://link.aip.org/link/?PSI/6082/608205/1>.
- [51] Houssine Makhlouf, Anthony A. Tanbakuchi, Andrew R. Rouse, and Arthur F. Gmitro. Design of a multi-spectral channel for in-vivo confocal microscopy. volume 6432, page 643206. SPIE, 2007. doi: 10.1117/12.698697. URL <http://link.aip.org/link/?PSI/6432/643206/1>.
- [52] D.J. Bowrey and J.H. Peters. LAPAROSCOPIC ESOPHAGEAL SURGERY. *Surgical Clinics of North America*, 80(4):1213–1242, 2000.
- [53] K. Lange and L.J. Boyd. The use of fluorescein to determine the adequacy of the circulation. *Med Clin North Am*, 26:943–952, 1942.
- [54] M. Morykwas, H. Hills, and L. Argenta. The safety of intravenous fluorescein administration. *Ann. Plas. Surg.*, 26:551–553, 1991.
- [55] S. Srivastava, J.J. Rodríguez, A.R. Rouse, M.A. Brewer, and A.F. Gmitro. Computer-aided identification of ovarian cancer in confocal microendoscope images. *Journal of Biomedical Optics*, 13:024021, 2008.

- [56] K. Kusuzaki, H. Murata, T. Matsubara, S. Miyazaki, K. Shintani, M. Seto, A. Matsumine, H. Hosoi, T. Sugimoto, and A. Uchida. Clinical outcome of a novel photodynamic therapy technique using acridine orange for synovial sarcomas. *Photochem Photobiol*, 81(3):705–9, 2005.
- [57] R. Kiesslich, J. Burg, M. Vieth, J. Gnaediger, M. Enders, P. Delaney, A. Polglase, W. McLaren, D. Janell, S. Thomas, et al. Confocal laser endoscopy for diagnosing intraepithelial neoplasias and colorectal cancer in vivo. *Gastroenterology*, 127(3):706–713, 2004.
- [58] Josh A. Udovich, D. G. Besselsen, and Arthur F. Gmitro. Assessment of acridine orange and SYTO 16 for in vivo imaging of the peritoneal tissues in mice. *Journal of Microscopy*, In press, 2008.
- [59] R.K. Mustonen, M.B. McDonald, S. Srivannaboon, A.L. Tan, M.W. Doubrava, and C.K. Kim. Normal Human Corneal Cell Populations Evaluated by In Vivo Scanning Slit Confocal Microscopy. *Cornea*, 17(5):485, 1998.
- [60] Timothy R Corle and Gordon S Kino. *Confocal scanning optical microscopy and related imaging systems*. Academic Press, San Diego, 1996. ISBN 0124087507 (alk. paper). URL <http://www.loc.gov/catdir/description/els032/96001999.html>.
- [61] T Wilson, editor. *Confocal Microscopy*. Academic Press, 1990.
- [62] M. Magnor, P. Dorn, and W. Rudolph. Simulation of confocal microscopy through scattering media with and without time gating. *Journal of the Optical Society of America B*, 18(11):1695–1700, 2001.
- [63] C.M. Blanca and C. Saloma. Monte Carlo analysis of two-photon fluorescence imaging through a scattering medium. *Applied Optics*, 37(34), 1998.

- [64] N. Metropolis and S. Ulam. The monte carlo method. *Journal of the American Statistical Association*, pages 335–341, 1949.
- [65] L. Wang, S.L. Jacques, and L. Zheng. MCML—Monte Carlo modeling of light transport in multi-layered tissues. *Computer Methods and Programs in Biomedicine*, 47(2):131–146, 1995.
- [66] BC Wilson and G. Adam. A Monte Carlo model for the absorption and flux distributions of light in tissue. *Medical Physics*, 10:824, 1983.
- [67] SA Prahl, M. Keijzer, SL Jacques, and AJ Welch. A Monte Carlo model of light propagation in tissue. *Dosimetry of Laser Radiation in Medicine and Biology*, 155:102–111, 1989.
- [68] A. Liebert, H. Wabnitz, N. Zolek, and R. Macdonald. Monte Carlo algorithm for efficient simulation of time-resolved fluorescence in layered turbid media. *Optics Express*, 16(17):13188–13202, 2008.
- [69] JM Schmitt and K. Ben-Letait. Efficient Monte Carlo simulation of confocal microscopy in biological tissue. *Journal of the Optical Society of America A*, 13: 952–961, 1996.
- [70] R.J. Crilly, W.F. Cheong, B. Wilson, and J.R. Spears. Forward-adjoint fluorescence model: Monte Carlo integration and experimental validation. *Applied Optics*, 36(25), 1997.
- [71] J. Swartling, A. Pifferi, A.M.K. Enejder, and S. Andersson-Engels. Accelerated Monte Carlo models to simulate fluorescence spectra from layered tissues. *Journal of the Optical Society of America A*, 20(4):714–727, 2003.

- [72] AJ Welch, C. Gardner, R. Richards-Kortum, E. Chan, G. Criswell, J. Pfefer, and S. Warren. Propagation of Fluorescent Light. *Lasers in Surgery and Medicine*, 21:166–178, 1997.
- [73] JM Schmitt, A. Knuettel, and M. Yadlowsky. Confocal microscopy in turbid media. *Journal of the Optical Society of America A*, 11:2226–2226, 1994.
- [74] M. Galassi, J. Davies, J. Theiler, B. Gough, G. Jungman, M. Booth, and F. Rossi. GNU Scientific Library Reference Manual-Revised Second Edition (v1. 8). *Bristol, United Kingdom: Network Theory Ltd*, 2006.
- [75] P. L'Ecuyer. Combined multiple recursive random number generators. *Operations Research*, pages 816–822, 1996.
- [76] B. Roy Frieden. *Probability, statistical optics, and data testing: a problem solving approach*, volume 10. Springer, Berlin, 3rd ed edition, 2001. ISBN 3540417087 (alk. paper). URL <http://www.loc.gov/catdir/enhancements/fy0815/2001020879-d.html>.
- [77] LG Henyey and JL Greenstein. Diffuse radiation in the galaxy *Astrophys. J*, 93: 70–83, 1941.
- [78] SL Jacques, CA Alter, and SA Prahl. Angular dependence of HeNe laser light scattering by human dermis. *Lasers Life Sci*, 1(4):309–333, 1987.
- [79] A.J. Welch and M.J.C. van Gemert. *Optical-thermal Response of Laser-irradiated Tissue*. Plenum Pub Corp, 1995.
- [80] HC van de Hulst. Multiple light scattering. Tables, formulas and applications. *New York: Academic Press*, 1980.

- [81] RG Giovanelli. Reflection by Semi-infinite Diffusers. *Journal of Modern Optics*, 2(4):153–162, 1955.
- [82] R Development Core Team. *R: A Language and Environment for Statistical Computing*. R Foundation for Statistical Computing, Vienna, Austria, 2008.
URL <http://www.R-project.org>. ISBN 3-900051-07-0.
- [83] WF Cheong, SA Prahl, and AJ Welch. A review of the optical properties of biological tissues. *Quantum Electronics, IEEE Journal of*, 26(12):2166–2185, 1990.
- [84] T. Vo-Dinh et al. Biomedical Photonics Handbook. *Journal of Biomedical Optics*, 9:1110, 2004.
- [85] Daniel Adler and Duncan Murdoch. *rgl: 3D visualization device system (OpenGL)*, 2008. URL <http://rgl.neoscientists.org>. R package version 0.81.
- [86] Dan Carr, ported by Nicholas Lewin-Koh, and Martin Maechler. *hexbin: Hexagonal Binning Routines*, 2008. R package version 1.17.0.
- [87] BC Wilson and SL Jacques. Optical reflectance and transmittance of tissues: principles and applications. *Quantum Electronics, IEEE Journal of*, 26(12):2186–2199, 1990.
- [88] France Schwarz, Arnaud Le Nevez, Magalie Genet, Anne Osdoit, and François Lacombe. Deep high-resolution fluorescence microscopy of full organs: the benefit of ultraminiature confocal miniprobes. volume 7172, page 71720G. SPIE, 2009. doi: 10.1117/12.808108. URL <http://link.aip.org/link/?PSI/7172/71720G/1>.